Dynamics of structures in active suspensions of paramagnetic particles and applications to artificial micro-swimmers

by

Eric Edward Keaveny

Sc.M., Applied Mathematics, Brown University, 2006
B.S., Applied Physics, Columbia University, 2001

Thesis

Submitted in partial fulfillment of the requirements for
the Degree of Doctor of Philosophy
in the Division of Applied Mathematics at Brown University

May 2008

This dissertation by Eric Edward Keaveny is accepted in its present form by
the Division of Applied Mathematics as satisfying the
dissertation requirement for the degree of
Doctor of Philosophy

Date........................ ....
Martin R. Maxey, Director

Recommended to the Graduate Council

Date........................ ....
George Em Karniadakis, Reader

Date........................ ....
Thomas R. Powers, Reader

Approved by the Graduate Council

Date........................ ....
Sheila Bonde
Dean of the Graduate School

The Vita of Eric Edward Keaveny

Eric Edward Keaveny was born on November 8, 1979 in the village of Port Chester in Westchester County, New York. After growing up in the nearby town of Harrison and attending Harrison High School from 1993–1997, he continued his studies at Columbia University's Fu Foundation School of Engineering and Applied Science in New York, NY. During this time he was selected to participate in the Department of Energy's National Undergraduate Fellowship Program in Plasma Physics and Fusion Energy Sciences for the summer of 2000. In 2001, he graduated *cum laude* from Columbia attaining a B.S. in Applied Physics. He then took a job as a carpenter working at spots along the Hudson River, from Manhattan to Greene County. After doing this for one year, he began his graduate studies in the Division of Applied Mathematics at Brown University in Providence, RI in September 2002 eventually earning an Sc.M. in Applied Mathematics in 2006. While at Brown, he was awarded a VIGRE Fellowship (2002-2004) and a Simon Ostrach Graduate Fellowship (2007).

Publications:

1. E.E. Keaveny and M.R. Maxey. Modeling the magnetic interactions between paramagnetic beads in magnetorheological fluids. *submitted to J. Comp. Phys.*

2. E.E. Keaveny and M.R. Maxey. Interactions between co-moving magnetic microswimmers. *Phys. Rev. E*, 77:041910, 2008.

3. E.E. Keaveny and M.R. Maxey. Spiral swimming of an artificial micro-swimmer. *J. Fluid Mech.*, 598:293-319, 2008.

4. E.E. Keaveny, I.V. Pivkin, M. Maxey and G.E. Karniadakis. A comparative study between dissipative particle dynamics and molecular dynamics for simple- and complex-geometry flows. *J. Chem. Phys.*, 123:104107, 2005.

Acknowledgments

This thesis is dedicated to the memories of Edward Saviano and Mario Santangelo.

I would first like to thank my thesis advisor Professor Martin Maxey. From the onset of my graduate career to the completion of this thesis, his dedication, guidance, and encouragement have been invaluable. I also express gratitude to Professor George Karniadakis for serving as a reader of this thesis and his active participation in my research. I also wish to thank Professor Thomas Powers for his service as a reader and for his many questions and comments over the course of this work.

I would like to thank Professor David Gottlieb for providing me with the opportunity to visit Paris and the laboratory where the micro-swimmer experiments were performed. I also thank Professor Eric Climent and Micheline Abbas for their many discussions and hosting me during my visit to Toulouse.

I would like to thank the staff of the Division of Applied Mathematics. I would especially like to thank Madeline Brewster for all of her help with recommendation letters during my job search and for making the "Brewster brew" that has fueled many morning thoughts. I would also like to extend thanks to Jean Radican for all of her help, but more importantly for bringing me food and medicine when I was a sick prospective student bed ridden at the Arlington house.

I would like to thank the graduate students of the greater fluid mechanics group in the Division. I offer specific thanks to Igor Pivkin and Jasmine Foo for their many conversations and friendship. I also would like to thank friends from my entering class: Kevin Leder, Thomas Dean and Peter Oman and wish them the best on their future endeavors.

I would like to thank the many friends that I have met over the years before beginning graduate school especially Christopher Borgia, Benjamin Fiering, Michael Burbank, Jeremy Milgrim, and Eve Klein. I appreciate all of their efforts to keep in touch. I am also indebted to the friends that I have made here in Providence, especially Barbara Giovannone, Olga Yoshizumi, Mary Farnsworth and Benjamin Davies along with my roommates Stephen Miller and Thomas Pollard. I thank you all for great memories and I hope these friendships continue over years to come. I give special thanks to Lisa Longato. Without her, the experience of looking for employment and writing this thesis would not have been nearly as enjoyable. I wish her the best and offer my support and love as she continues her graduate work.

Finally, none of this would be possible without the continued support and love of my family. Mom, Dad and Keith – I love each of you and appreciate everything that you have done for me.

This work was supported financially by an NSF VIGRE Fellowship, a Simon Ostrach Graduate Fellowship and by the NSF under grant number CTS-0326702.

Contents

List of Tables

List of Figures

Chapter 1

Introduction

Superparamagnetic particles, ranging from $0.3 - 10\mu m$ in diameter, suspended in a liquid will aggregate to form chains when an initially random dispersion is placed in a uniform, static magnetic field. The formation of these fibrous structures changes the bulk rheological properties of the medium and as such these suspensions are typically referred to as magnetorheological fluids (MR) [67]. Traditionally, MR fluids have been employed in a variety of damping and shock absorbing devices where the particle volume fractions for the suspensions range from 20-40%. In this context, the particles are usually carbonyl iron powders suspended in oil and are subject to strong magnetic fields, in excess of $10^5 A/m$. Such MR fluids differ from ferrofluids [108] that consist of colloidal suspensions of nanoscale ferromagnetic particles, typically single domain magnetite crystals $10nm$ in diameter. In ferrofluids, the particles have a surfactant coating that prevents permanent aggregation and Brownian motion is very significant, inhibiting the formation of particle structures.

More recently, superparamagnetic particles and the structures that they form have been employed in a variety of microfluidic devices. These monodisperse polymeric spherical particles containing randomly oriented magnetite crystals are key components in recently developed DNA separation chips [32] and micro-mixers [105]. Small groups of particles can be manipulated to form micro-pumps in a channel [13], or joined together to a produce magnetic filament [48, 11] that provides the propulsive mechanism for an artificial micro-swimmer [33].

Additional experimental studies have focused on the basic physics of these suspensions and the self-assembled structures. There have been numerous studies regarding the aggregation processes and the growth rates of the chain structures in suspensions subject to a uniform field [102, 31, 90, 95]. The strength and interactions between the individual linear structures has also been investigated [41, 43, 42]. Aggregation under rotating fields has also been considered [93, 115] and illustrated how the introduction of viscous stresses can dramatically change the shape of the resulting structures.

While there has been an extensive experimental effort to quantify suspension properties and structural dynamics, the number of theoretical or numerical studies in this area has been limited. Additionally, the analyses that has been performed employ simple drag models to provide the hydrodynamic forces and fixed point dipole models to give the magnetic interactions [94, 93, 69]. These models are valid only in the limit of very dilute, uniform suspensions and will fail to provide a correct description of the interactions when the particles begin to aggregate under the influence of the applied field. One of the primary goals of this thesis is to establish a simulation technique able to efficiently and accurately handle of ensembles of tens to thousands of particles. In these simulations, the hydrodynamic interactions are provided by the force-coupling method (FCM). FCM has been used previously to study aggregation in a uniform applied field [25]. The magnetic interactions are determined using a method developed here that combines a finite-dipole model and the resulting multipoles from the exact two body calculation. This method is described and verified in Chapter 3. In Chapter 4, we validate the complete simulation and explore the effects of short-range solid contact barriers by considering the dynamics of a pair of particles subject to a rapidly rotating field. We also consider more generally the dynamics of suspensions of paramagnetic beads subject to shear flows and rotating fields where the hydrodynamic forces can deform and rupture the chains.

One of the devices constructed from superparamagnetic beads is the artificial micro-swimmer that consists of a chain of beads linked together to from an artificial flagellum and attached to a human red blood cell [33]. In addition to providing a physical model with which to study the fundamental aspects of low Reynolds number propulsion and the swimming of microorganisms, this biomimetic device is the first step toward engineering controllable micro-swimmers. We are able to provide a simulation of this device using the methods introduced to describe the interactions between paramagnetic particles in conjunction with an additional model developed here to capture the elastic coupling afforded by the flexible chemical links between the beads. This method is described in Chapter 5 as are the resulting swimming speeds of the device determined by the simulations. The originally proposed swimming strategy employed oscillating magnetic fields to generate a transverse beating motion of the flagellum, similar to the motion of a spermatozoa. In Chapter 6, we propose and demonstrate the effectiveness of an alternative strategy that uses rotating fields to facilitate a swimming analogous to the helical flagellum motion exhibited by certain bacteria. In addition to providing simulations of this behavior, we perform analysis based on a resistive force/continuous elastica model to explore the dependence of the swimming speed on the swimmer geometry and magnetic field in the low frequency limit.

As the magnetic micro-swimmer may serve as a physical model for a swimming microorganism, we perform a variety of simulations to understand how two artificial micro-swimmers will interact with each other. These results are presented in Chapter 7 and the nature of the hydrodynamic and magnetic interactions between the swimmers are determined. Additionally we indicate at what range of separation distances a point representation of the swimmers may be appropriate. We also quantify the interactions between a single swimmer and a rigid surface. The far-field effects of the surface are obtained using the image systems for various fundamental singularities for the Stokes equations and lubrication forces are added to resolve the particle mobility near contact. With this representation, we examine the changes in swimming speed and motions away from the surface for a planar-type swimmer and the rolling motion of a spiral swimmer. The hydrodynamic wall model and the simulation results are presented in Chapter 8.

Although the methods developed and employed in this thesis are intended to describe the dynamics of paramagnetic beads and filaments, in Chapter 9 of this thesis we demonstrate these methods can be extended to address an additional class of problems. Specifically, we adapt to FCM the 'squirmer' model for a swimming microorganism developed by Ishikawa *et al.* [57]. The squimer model is appropriate for ciliated microorganisms or as an initial model for flagellum-propelled swimmers over times scales long compared to the rapid flagellum oscillations ($\approx 100Hz$ or more). We demonstrate that the FCM-squimer formulation reproduces both the squirmer trajectories [57] and suspension self-diffusion coefficients [55] and allows for at least an order-of-magnitude increase in the number of squirmers that can be considered in a simulation.

Chapter 2

The motion of paramagnetic beads in viscous fluid

2.1 Introduction

Paramagnetic beads suspended in a viscous fluid experience hydrodynamic forces, $\mathbf{F}_{hydro}$, interparticle magnetic force, $\mathbf{F}_{mag}$, short-ranged interparticle surface forces $\mathbf{F}_{surf}$ and random Brownian forces $\mathbf{F}_{rand}$. The dynamics of these rigid spherical particles of mass m and radius a are given by Newton's equation of motion where

$$m\frac{d\mathbf{V}_n}{dt} = \mathbf{F}^n_{hydro} + \mathbf{F}^n_{mag} + \mathbf{F}^n_{surf} + \mathbf{F}^n_{rand} \tag{2.1}$$

for bead n. On the left hand side of (2.1), $\mathbf{V}_n$ is the bead's translational velocity. The time scale associated with particle relaxation is given by $\tau_p = m/(6\pi a\eta)$ where η is the viscosity of the surrounding fluid. Using representative values of the radius $a \approx 1\mu m$, the viscosity of the fluid $\eta \approx 1cm^2/s$ and mass $m \approx 5 \times 10^{-15}kg$, the relaxation time scale for the paramagnetic particles is approximately $\tau_p \approx 2.7 \times 10^{-7}s$. Since this time scale is much shorter than that associated with the particle motion $a/V \approx 1s$, we may neglect the effects of particle inertia [92] and at each instant in time the forces on each bead n will balance

$$\mathbf{F}^n_{mag} + \mathbf{F}^n_{surf} + \mathbf{F}^n_{hydro} + \mathbf{F}^n_{rand} = \mathbf{0}. \tag{2.2}$$

Since the hydrodynamic forces will depend on the velocity of the particles and their configuration, (2.2) establishes a mobility problem that must be solved to determine the particle motion.

In the following sections, we describe the exact calculation of these four forces and introduce the models we employ to provide an accurate description of the physics using computationally efficient algorithms.

2.2 Hydrodynamic Forces

The fluid will exert the force $\mathbf{F}^n_{hydro}$ on bead n centered at $\mathbf{Y}_n$ moving with velocity $\mathbf{V}_n$ and rotating with angular velocity $\mathbf{\Omega}_n$. This force can be determined by solving the Navier-Stokes equations for a incompressible fluid [3, 75]

$$\rho\left(\frac{\partial \mathbf{u}}{\partial t} + (\mathbf{u}\cdot\boldsymbol{\nabla})\mathbf{u}\right) = -\boldsymbol{\nabla} p + \eta\nabla^2\mathbf{u} \tag{2.3}$$

$$\boldsymbol{\nabla}\cdot\mathbf{u} = 0 \tag{2.4}$$

subject to the no-slip boundary condition on surfaces of the beads

$$\mathbf{u} = \mathbf{V}_n + \mathbf{\Omega}_n \times (\mathbf{x} - \mathbf{Y}_n) \text{ at } |\mathbf{x} - \mathbf{Y}_n| = a. \tag{2.5}$$

Once the flow field $\mathbf{u}$ has been found, the force on bead n can be found from the fluid stress

$$\mathbf{F}^n_{hydro} = \int_{|\mathbf{x}-\mathbf{Y}_n|=a} \boldsymbol{\sigma}\cdot\hat{\mathbf{n}}dS \tag{2.6}$$

$$= \int_{|\mathbf{x}-\mathbf{Y}_n|=a} \left[-p\hat{\mathbf{n}} + \eta\left(\boldsymbol{\nabla}\mathbf{u} + (\boldsymbol{\nabla}\mathbf{u})^T\right)\right]\cdot\hat{\mathbf{r}}dS \tag{2.7}$$

where $\hat{\mathbf{r}}$ is the unit vector normal to the surface of the sphere. Similarly, the hydrodynamic torque on the particle is

$$\boldsymbol{\tau}^n_{hydro} = \int_{|\mathbf{x}-\mathbf{Y}_n|=a} (\mathbf{x} - \mathbf{Y}_n)\times\boldsymbol{\sigma}\cdot\hat{\mathbf{n}}dS \tag{2.8}$$

Given a characteristic fluid velocity U, we may non-dimensionalize the equations of motion for the fluid phase

$$\frac{\rho U a}{\eta}\left(\frac{\partial \mathbf{u}}{\partial t} + (\mathbf{u}\cdot\boldsymbol{\nabla})\mathbf{u}\right) = -\boldsymbol{\nabla} p + \eta\nabla^2\mathbf{u} \tag{2.9}$$

$$\boldsymbol{\nabla}\cdot\mathbf{u} = 0. \tag{2.10}$$

The quantity $\rho U a/\eta$ is the *Reynolds number* and quantifies the importance of the fluid inertia relative to the viscous stresses. The Reynolds number associated with the motion of paramagnetic particle is typically on the order of $\mathrm{Re} \approx 10^{-5} - 10^{-3}$. This allows us to reduce the Navier-Stokes equations to the linear Stokes equations

$$-\boldsymbol{\nabla} p + \eta\nabla^2\mathbf{u} = 0 \tag{2.11}$$

$$\boldsymbol{\nabla}\cdot\mathbf{u} = 0 \tag{2.12}$$

whose properties are described thoroughly in [65, 50]. The Stokes equations yield a linear relationship between the hydrodynamic force and the particle velocity. For a single spherical particle this relationship is

$$\mathbf{F} = -6\pi\eta a\mathbf{V}. \tag{2.13}$$

where the coefficient $6\pi\eta a$ is known as the Stokes drag law. Since the linear relationship is a result of the governing equations, it extends to particles of arbitrary shape and applies in more general situations where there is an ensemble of N translating and rotating particles

$$\begin{bmatrix} \mathcal{F}_{hydro} \\ \mathcal{T}_{hydro} \end{bmatrix} = -\mathcal{R}\begin{bmatrix} \mathcal{V} \\ \mathcal{W} \end{bmatrix} \tag{2.14}$$

with $\mathcal{F}_{hydro}$ being the $3N \times 1$ vector containing all the information regarding the hydrodynamic forces on all the beads. Similarly, $\mathcal{T}_{hydro}$, $\mathcal{V}$ and $\mathcal{W}$ are $3N \times 1$ vectors holding all the viscous torque, velocity and angular velocity information for all the particles respectively. The grand resistance matrix, $\mathcal{R}$, is now a $6N \times 6N$ matrix that depends on the configuration of the beads and couples the motion of one particle with that of another.

As the hydrodynamic forces on the paramagnetic beads balance the three other forces on the particles,

$$-\mathcal{R}\mathcal{V} + \mathcal{F}_{mag} + \mathcal{F}_{surf} + \mathcal{F}_{rand} = 0 \tag{2.15}$$

where $\mathcal{F}_{mag}$, $\mathcal{F}_{surf}$ and $\mathcal{F}_{rand}$ are $3N \times 1$ vector holding the magnetic forces, surface forces and Brownian forces for all the particles respectively. The motion of the beads at each time instant is then given by

$$\mathcal{V} = \mathcal{M}\left(\mathcal{F}_{mag} + \mathcal{F}_{surf} + \mathcal{F}_{rand}\right) \tag{2.16}$$

where $\mathcal{M} = \mathcal{R}^{-1}$ is the grand mobility matrix. Determining the motion of many paramagnetic beads requires that one first compute the external forces on the particle. Once this has been completed, the resistance matrix needs to be formulated and the linear system solved to obtain $\mathcal{V}$.

2.2.1 Solving the mobility problem: Force-coupling method

Once the non-hydrodynamic forces on the particles are determined, the particle configuration dependent resistance matrix $\mathcal{R}$ needs to be determined to compute the particle velocities and angular velocities. This involves solving the Stokes equations subject to the no-slip boundary conditions on each particle. For a system of many particles, performing this task directly is not tractable. We therefore employ a technique called the *force-coupling method* (FCM) [91, 81] to solve the mobility problem.

FCM is a two step method where the first step provides the representation of particle phase to the fluid phase. This is achieved through a low order finite force multipole expansion truncated at the dipole term

$$\begin{aligned} \boldsymbol{\nabla} p - \eta \nabla^2 \mathbf{u} &= \sum_{n=1}^{N} \mathbf{F}^n_{ext} \Delta_n(\mathbf{x} - \mathbf{Y}_n) + \sum_{n=1}^{N} \mathbf{G}^n \cdot \boldsymbol{\nabla} \Xi_n(\mathbf{x} - \mathbf{Y}_n) & (2.17) \\ \boldsymbol{\nabla} \cdot \mathbf{u} &= 0 & (2.18) \end{aligned}$$

where

$$\begin{aligned} \Delta_n(\mathbf{x}) &= (2\pi\sigma^2_{n,\Delta})^{-3/2} \mathrm{e}^{-r^2/2\sigma^2_{n,\Delta}} & (2.19) \\ \Xi_n(\mathbf{x}) &= (2\pi\sigma^2_{n,\Xi})^{-3/2} \mathrm{e}^{-r^2/2\sigma^2_{n,\Xi}}. & (2.20) \end{aligned}$$

The parameters $\sigma_{n,\Delta}$ and $\sigma_{n,\Xi}$ are set by matching the conditions for particle motion in Stokes flow and are related to the bead radius a_n as $\sigma_{n,\Delta} = a_n/\sqrt{\pi}$ and $\sigma_{n,\Delta} = a_n/(6\sqrt{\pi})^{1/3}$. $\mathbf{F}^n_{ext} = \mathbf{F}^n_{surf} + \mathbf{F}^n_{mag} + \mathbf{F}^n_{rand}$ is the total external force on bead n. If there is an external torque on the particles, the antisymmetric part of the tensor $\mathbf{G}^n$ is, in index notation, $G^n_{ij} = \frac{1}{2}\epsilon_{ijk}\tau^n_{ext,k}$. The symmetric part of this tensor is chosen so

$$\int \frac{1}{2}\left(\nabla\mathbf{u} + (\nabla\mathbf{u})^{\mathrm{T}}\right)\Xi_n(\mathbf{x}-\mathbf{Y}_n)d^3\mathbf{x} = \mathbf{0}. \tag{2.21}$$

The second step entails determining the velocity and angular velocity of bead n from the resulting flow field through

$$\mathbf{V}_n = \int \mathbf{u}(\mathbf{x})\Delta_n(\mathbf{x}-\mathbf{Y}_n)d^3\mathbf{x} \tag{2.22}$$

$$\boldsymbol{\Omega}_n = \frac{1}{2}\int \boldsymbol{\omega}(\mathbf{x})\Xi_n(\mathbf{x}-\mathbf{Y}_n)d^3\mathbf{x} \tag{2.23}$$

where $\boldsymbol{\omega}$ is the vorticity of the fluid.

FCM has been used successfully in a variety of numerical studies ranging from understanding platelet aggregation in capillaries [100] to optimizing the performance of colloidal micro-pumps [80]. FCM preserves a consistent balance between the viscous dissipation in the flow and the rate of work by the particle phase and the external forces. It further captures the corresponding degenerate multipole contributions to the flow and includes the Faxén corrections for particle motion in a spatially varying flow field [65]. Near contact flow features not resolved by FCM can be included using a lubrication force calculation [28]. Additionally, FCM can be employed to describe particle motion at finite Reynolds numbers [82, 24] up to $Re < 20$, or modified to consider ellipsoidal particles [79].

2.3 Magnetic Forces

When subject to a uniform applied field, each bead will acquire a magnetization that will in turn generate an additional field. The mutual interactions then give the interparticle magnetic forces. Here, we concern ourselves with the magnetic interactions between paramagnetic particles that have a low magnetic susceptibility and exhibit minimal hysteresis. We further limit our discussion to cases where the magnetization of a particle responds linearly to the applied field, $\mathbf{M} = \chi\mathbf{H}$ where $\mathbf{M}$ is the particle magnetization, χ is the particle magnetic susceptibility and $\mathbf{H}$ is the local magnetic field. For many of paramagnetic particles, the magnetic susceptibility $\chi \approx 1$. The linear response assumption suffices for the magnitudes of applied field $|\mathbf{H}| < 10^4 A/m$ that are employed in microfluidic applications mentioned in Chapter 1, for lab-on-a-chip devices [35] or structured materials [52], and over a certain range for standard MR fluids [68].

Consider N spheres of radius a and permeability $\mu = \mu_0(1+\chi)$ located $\mathbf{Y}_n, n = 1 \ldots N$, and subject to a uniform magnetic field $\mathbf{H}_0$. Since the fluid phase is assumed to have zero susceptibility, the permeability of fluid is that of free space, μ_0. Further, if there are no free currents in the system, Maxwell's equations [59] are

$$\boldsymbol{\nabla} \cdot \mathbf{B} = 0 \tag{2.24}$$

$$\boldsymbol{\nabla} \times \mathbf{H} = \mathbf{0} \tag{2.25}$$

with the magnetic flux density $\mathbf{B} = \mu_0 \mathbf{H}$ in the fluid and $\mathbf{B} = \mu \mathbf{H}$ in each sphere. Equation (2.25) allows the introduction of the scalar potentials such that $\mathbf{H} = -\boldsymbol{\nabla}\Phi^{out}$ in the fluid phase and $\mathbf{H} = -\boldsymbol{\nabla}\Phi_n^{in}$ inside sphere n for $n = 1, \ldots, N$. From the relationships between $\mathbf{B}$ and $\mathbf{H}$ and (2.24), we arrive at Laplace's equation for the fluid and particle phases,

$$\nabla^2 \Phi^{out} = 0 \tag{2.26}$$

$$\nabla^2 \Phi_n^{in} = 0. \tag{2.27}$$

For a coordinate system whose origin is located at $\mathbf{Y}_n$, we define $\mathbf{r}_n = \mathbf{x} - \mathbf{Y}_n$ with $r_n = |\mathbf{r}_n|$ and $\hat{\mathbf{r}}_n = \mathbf{r}_n / r_n$. At the surface of each sphere, the conditions

$$[\hat{\mathbf{r}}_n \cdot \mathbf{B}]_-^+ = 0 \tag{2.28}$$

$$[\hat{\mathbf{r}}_n \times \mathbf{H}]_-^+ = 0 \tag{2.29}$$

require the potential satisfy

$$\Phi_n^{in} = \Phi^{out} \tag{2.30}$$

$$\mu \frac{\partial \Phi_n^{in}}{\partial r_n} = \mu_0 \frac{\partial \Phi^{out}}{\partial r_n} \tag{2.31}$$

at $r_n = a$ for $n = 1 \ldots N$. Additionally, as $r_n \to \infty$

$$\Phi^{out} \to -\mathbf{H}_0 \cdot \mathbf{r}_n. \tag{2.32}$$

After solving for the potential and computing the field, the Maxwell stress tensor, given in index notation by

$$T_{ij} = \mu_0 H_i H_j - \frac{\mu_0}{2}\delta_{ij} H_k H_k, \tag{2.33}$$

is formed from the exterior field and the resultant force on bead n is determined from

$$\mathbf{F}_n = \int_{r_n=a} \mathbf{T}\cdot\hat{\mathbf{r}}_n dS. \tag{2.34}$$

The general solution to (2.26) can, in principle, be written down as a sum of the potential due to the external magnetic field and the sum of N spherical harmonic expansions, where the expansion for the n^{th} particle has the origin located at $\mathbf{Y}_n$. The complications arise through application of the boundary conditions (2.30) and (2.31) when one must truncate the expansions retaining L multipoles and relate the different coordinate systems to each other. Even if this is done successfully, one is left with, in general, an intractable linear system of equations to determine the unknown coefficients in each expansion.

In Chapter 3 we present the dipole models previously used and a new finite dipole and higher multipole inclusion method we introduce to determine the interparticle magnetic forces. All the models presented there are, in some way, a reduction of this general problem. Each model is classified not only by the degree to which the particles interact (dipole, quadrapole, etc.) but also by how many particles are involved in each interaction (two-body, three-body, etc.).

2.4 Surface and Contact forces

In suspensions containing polymeric particles, Van der Waals forces can lead to unwanted clumping of particles, or non-reversible magnetic aggregation in which these forces prevent a relaxation to a uniform suspension when the applied field is removed. To provide a stable colloidal dispersion where these effects are not a present, a surfactant is typically added to the fluid phase. For suspensions of polystyrene paramagnetic particles in water, the surfactant sodium dodecyl sulfate (SDS) is used as the stabilizing agent at concentrations of approximately $\phi \approx 8$ mM [43, 31]. The surfactant both binds to the surface of the particle modifying the surface characteristics and remains in solution allowing for double-layer repulsion between the particles. For a planar surface with potential ψ_0, the Debye-

Huckel approximation to the Poisson-Boltzmann equation [109, 58] gives

$$\psi(x) = \psi_0 \mathrm{e}^{-\kappa x} \tag{2.35}$$

for the potential ψ from the surface when a binary 1-1 electrolyte of concentration ϕ is present. In (2.35), κ^{-1} is the Debye length given by

$$\kappa^{-1} = \left(\frac{\epsilon k_B T}{2e^2\phi}\right)^{1/2} \tag{2.36}$$

where k_B is Boltzmann's constant, T is the temperature, ϵ is the dielectric constant of the fluid and e is the charge of an electron. The Debye length provides the length scale associated with the double-layer interactions. For two spheres of constant potential ψ_0 whose surfaces are separated by the distance $h << a$ that is much smaller than the radii of the spheres, a Derjagiun approximation calculation reveals the magnitude of the double layer repulsive force is given by [109]

$$F(h) = 2\pi\epsilon \left(\frac{k_B T}{e}\right)^2 \kappa a \psi_0^2 \frac{\mathrm{e}^{-\kappa h}}{1+\mathrm{e}^{-\kappa h}}. \tag{2.37}$$

For an SDS concentration $\phi = 8mM$ in water ($\epsilon_{H_2O} = 80\epsilon_0$) at $T = 300K$, the Debye length is $\kappa^{-1} = 3.5nm$ which is very small relative to the radius of the particle.

The inclusion of such a short ranged force in a simulation would require the resolution of a time scale very small compared to dynamics of interest. We therefore employ a generic pairwise collision barrier of the form

$$\mathbf{F}_{surf}^{nm} = -\frac{F_{ref}}{2a}\left(\frac{R_{ref}^2 - r_{nm}^2}{R_{ref}^2 - 4a^2}\right)^4 \mathbf{x}_{nm}. \tag{2.38}$$

between beads n and m where $\mathbf{x}_{nm} = \mathbf{Y}_n - \mathbf{Y}_m$ and $r_{nm} = |\mathbf{x}_{nm}|$. In the computations, this force also serves the non-physical purpose of preventing particle overlap as they come into contact as a result of magnetic attraction. In our simulations, $R_{ref} = 2.2a$ and $F_{ref} = 1.05F_{con}$ where F_{con} is the magnitude of the attractive force at contact given by the magnetic model employed in the simulation. In Chapter 4, we examine the effects of the collision barrier on the oscillation dynamics of a bead pair in a rotating field. Previously, the effects of this type of interparticle force on the mean settling velocity and velocity fluctuations in sedimenting suspensions were investigated [27].

2.5 Random Brownian Forces

As a result of collisions with the molecules that compose a surrounding fluid medium, micron-sized particles will perform a random walk typically called Brownian motion. This behavior leads to the diffusion of particles from regions of high concentration to low concentration. At the particle level, Brownian motion can be treated as a stochastic process whose statistics reproduce the correct diffusive behavior.

We first consider a collection of particles with concentration $\phi(\mathbf{x}, t)$ and subject to force $\mathbf{F} = -\boldsymbol{\nabla}\Phi$, where Φ is the potential energy. In equilibrium, the concentration will be given by a Boltzmann distribution

$$\phi_{equil}(\mathbf{x}) = \phi_o e^{-\Phi/k_B T}. \tag{2.39}$$

Additionally, the total flux of particles across any surface is zero and the flux of particles as a result of any external forces is balanced by the flux of particles due to diffusion [4]

$$-D\boldsymbol{\nabla}\phi_{equil} + \phi_{equil}\mathcal{M}\mathbf{F} = \mathbf{0}. \tag{2.40}$$

From (2.39) and the relationship between the force and the potential, the diffusion tensor is found to be

$$\mathcal{D} = k_B T \mathcal{M} \tag{2.41}$$

For a very dilute suspension, the mobility of each particle is approximately $\mathcal{M} = \mathcal{I}/(6\pi a\eta)$ where $\mathcal{I}$ is the identity matrix which gives the Stokes-Einstein [34] relation for the diffusion coefficient in the dilute limit

$$\mathcal{D} = \frac{k_B T}{6\pi a\eta}\mathcal{I}. \tag{2.42}$$

We are, however, interested in determining the motion of individual particles and accordingly would like to introduce forces on the particles that will, over time, give the correct diffusion of the particles. This is achieved by including a random force $\mathbf{F}_{rand}$ into the force balance for a given particle [109]

$$-\mathcal{R}\mathbf{V} + \mathbf{F}_{rand} = \mathbf{0}. \tag{2.43}$$

where $\mathbf{F}_{rand}$ is a random Gaussian vector that has zero mean and is uncorrelated in time

$$\begin{aligned}
\langle \mathbf{F}_{rand}(t) \rangle &= \mathbf{0} &(2.44)\\
\left\langle \mathbf{F}_{rand}(t)\mathbf{F}_{rand}(t') \right\rangle &= \mathcal{B}(t')\delta(t-t'). &(2.45)
\end{aligned}$$

The brackets $\langle \cdot \rangle$ indicate the average over an ensemble of particles. The tensor $\mathcal{B}$ needs to be chosen such that the over time, the proper diffusion coefficient is recovered. We may immediately write down the solution to (2.43) at time t and integrate further to obtain the position

$$\begin{aligned}
\mathbf{V}(t) &= \mathcal{M}(t)\mathbf{F}_{rand}(t) &(2.46)\\
\mathbf{Y}(t) &= \int_{-\infty}^{t} \mathcal{M}(t')\mathbf{F}_{rand}(t')dt'. &(2.47)
\end{aligned}$$

With this expression for the position, the position autocorrelation in index notation is given by

$$\langle Y_i(t)Y_j(t) \rangle = \int_{-\infty}^{t}\int_{-\infty}^{t} \mathcal{M}_{ik}(t')\mathcal{M}_{jl}(t'') \left\langle F_{rand,k}(t')F_{rand,l}(t'') \right\rangle dt'dt'' \qquad (2.48)$$

which the time correlation relation for the forces reduces to

$$\langle Y_i(t)Y_j(t) \rangle = \int_{-\infty}^{t}\int_{-\infty}^{t} \mathcal{M}_{ik}(t')\mathcal{M}_{jl}(t'')\mathcal{B}_{kl}(t'')\delta(t'-t'')dt'dt''. \qquad (2.49)$$

We may integrate the expression of the right hand side over t' to obtain

$$\langle Y_i(t)Y_j(t) \rangle = \int_{-\infty}^{t} \mathcal{M}_{ik}(t'')\mathcal{M}_{jl}(t'')\mathcal{B}_{kl}(t'')dt'.' \qquad (2.50)$$

which upon differentiation gives

$$\frac{d}{dt}\langle Y_i(t)Y_j(t) \rangle = \mathcal{M}_{ik}(t)\mathcal{M}_{jl}(t)\mathcal{B}_{kl}(t). \qquad (2.51)$$

Owing to the fact that the diffusion coefficient is given by

$$\mathcal{D}_{ij} = \frac{1}{2}\frac{d}{dt}\langle Y_i(t)Y_j(t) \rangle, \qquad (2.52)$$

and $D = k_B T \mathcal{M}$ we arrive at the expression for $\mathcal{B}_{ij}$

$$\mathcal{B}_{ij} = 2k_B T \mathcal{R}_{ij}. \tag{2.53}$$

The relative importance of Brownian motion on the motion of paramagnetic particles is provided by

$$\Lambda = \frac{\mu_0 \pi a^3 \chi^2 H_0^2}{9kT} \tag{2.54}$$

which is the ratio of the magnetic dipole interaction energy to the thermal energy [102, 25]. When $\Lambda \gg 1$ the effects of Brownian motion are dominated by the applied field. In experiments, the values of Λ can range from $1 < \Lambda < 5000$ [102, 31, 93, 43, 42]. In this work, we are primarily concerned with understanding the interplay between the hydrodynamic and interparticle magnetic forces and for simplicity, we ignore completely the effects of Brownian motion. In examining the behavior of suspensions subject to rotating fields, it was found that the results were not affected for values of $\Lambda > 50$ [94]. Therefore, even though we do ignore Brownian motion, results from our simulations may still be compared with a majority of the experiments.

2.6 Conclusions

In this chapter, we described the theoretical background associated with the forces experienced by paramagnetic particles in suspension. In addition, we presented models that we introduce to provide an effective simulation of ensembles ranging from tens to thousands of beads. In the following chapter, we provide a detailed account of the models developed and employed for the magnetic force calculation described in §2.3. These models provide the basis for our numerical studies of suspension dynamics and the artificial micro-swimmer.

Chapter 3

Models for determining the interparticle magnetic forces between paramagnetic beads

3.1 Introduction

For a linearly susceptible material, an exact computation of the magnetic interactions involves generating the solution to Laplace's equation subject to the appropriate boundary conditions [59]. The force on a given bead is then determined by formulating the Maxwell stress tensor from the resultant field and integrating the normal projection of this tensor over the bead's surface. This process is rather cumbersome and is only viable when considering systems of very few particles in symmetric configurations [23]. As a result, only dipole–dipole interactions are usually considered in simulations and in theoretical studies of MR fluids [94, 93, 25, 69]. Such point dipole methods require two steps. First, the values of the induced dipole moments for each particle need to be determined. Depending on the number of particles, this calculation can require solving a large system of linear equations. Once the dipole moments are computed, the resulting interparticle magnetic forces can be evaluated. This calculation requires depleted sums to avoid self-singular terms and scales inherently as $O(N^2)$ where N is the number of particles.

Although dipole simulations illustrate the general behavior of the aggregates, a more detailed description of the magnetic interactions is necessary to accurately quantify chain deformation and yield strengths in microfluidic devices. Beyond the point–dipoles description mentioned above, Ly et al. [84] have employed a combination of fast multipole methods (FMM) and boundary integral computations to resolve the magnetic interactions in two dimensional systems. Far-field interactions can be handled efficiently by FMM [49], where the domain is divided into cells and the effects of source terms in a distant cell are represented by a summed multipole series based on the moments of these source terms. Other models have been developed to simulate the interactions between dielectric particles in electrorheological (ER) fluids. Klingenberg et. al. [66, 70] determined the field resulting from two dielectric spheres in a uniform field from which they constructed an interparticle force function. With this functional form of the force, a molecular dynamics type of simulation was performed. Bonnecaze and Brady [14, 15, 16] approached the problem by constructing an approximate grand capacitance matrix. The matrix relates the multipole moments of each particle to the electric potential and its derivatives evaluated at the particles' locations, and aims to capture both the many–body, dipole interactions and the local two–body, higher multipole interactions. From this matrix, the electrostatic energy density is determined and differentiated to obtain the interparticle forces.

Here, we first develop a new model to accelerate the calculation of many–body dipole interactions. In this model, each bead's magnetization is represented as a finite distribution of current density. This eliminates the need for depleted sums to avoid singular self-interaction terms. For a sufficiently large number of particles the computational complexity scales as $O(N)$ where N is the number of particles. The finite nature of the distributions allows the model to be implemented with a variety of numerical algorithms or in combination with FMM solvers. Second, we present the exact solution to the two-body problem and introduce a technique to blend this result with a many-body dipole calculation. This inclusion procedure is general and can be used in conjunction with the finite dipole method presented here or any other dipole or higher-order multipole method.

In this chapter, we summarize and describe the point dipole models commonly used in MR fluid simulations. The interparticle forces given by these dipole methods are compared to exact calculations. We then formulate and present the finite–dipole model through exact solutions to Maxwell's equations and establish an iterative method to solve for particle interactions. The exact two–body calculation is described and from this calculation the far–field modification procedure is explained and implemented in a series of three–body problems.

3.1.1 Fixed Dipole Model

The simplest and most commonly used model is the fixed dipole model. In this model, only the magnetization induced by the external field is considered. Thus, the basis of this model is the solution to the general problem described for a single, isolated particle ($N = 1$). The coordinate system is aligned so $\mathbf{H}_0 = H_0\hat{\mathbf{z}}$. Symmetry conditions impose the lack of azimuthal dependence of the solution and the boundary conditions eliminate terms other than the $P_1(\cos\theta)$ term in the spherical harmonic expansion. The solution is, see [59],

$$\begin{aligned} \Phi_{in} &= -H_0 \frac{3\mu_0}{\mu + 2\mu_0} r\cos\theta && (3.1) \\ \Phi_{out} &= -H_0 r\cos\theta + H_0 a^3 \frac{\mu - \mu_0}{\mu + 2\mu_0}\frac{\cos\theta}{r^2}. && (3.2) \end{aligned}$$

For a linearly susceptible material, the induced magnetic dipole density $\mathbf{M} = \chi\mathbf{H}_{in}$, with $\chi = \mu/\mu_0 - 1$. The dipole moment, $\mathbf{m}$, is therefore

$$\mathbf{m} = \int_{sphere} \mathbf{M} d^3\mathbf{x} = \int_{sphere} \chi\mathbf{H}_{in} d^3\mathbf{x} = \frac{4}{3}\pi a^3 \chi_{eff}\mathbf{H}_0 \qquad (3.3)$$

where $\chi_{eff} = 3\chi/(\chi + 3)$. The field resulting from second term in (3.2) is equal to that due to a point dipole of strength $\mathbf{m}$ located at the sphere's center. Therefore, in the fixed dipole model, the field due to bead n is

$$\mathbf{H}_{dip}(\mathbf{x} - \mathbf{Y}_n) = \frac{1}{4\pi}\left(\frac{3\mathbf{m}\cdot(\mathbf{x} - \mathbf{Y}_n)}{r^5}(\mathbf{x} - \mathbf{Y}_n) - \frac{\mathbf{m}}{r^3}\right) \qquad (3.4)$$

with $r = |\mathbf{x} - \mathbf{Y}_n|$. The force on the point dipole $\mathbf{m}$ due to field $\mathbf{H}$ is given by [59]

$$\mathbf{F} = \mu_0 \boldsymbol{\nabla}\left(\mathbf{m}\cdot\mathbf{H}\right). \qquad (3.5)$$

Thus, for an ensemble of N spheres each having dipole moment $\mathbf{m}$, the resulting force on bead n due to the other beads is

$$\mathbf{F}^n = \mu_0 \boldsymbol{\nabla}_{\mathbf{Y}_n}\left(\mathbf{m}\cdot\sum_{k=1,k\neq n}^{N}\mathbf{H}_{dip}(\mathbf{Y}_n - \mathbf{Y}_k)\right). \qquad (3.6)$$

Note that in (3.5) a depleted summation necessary to avoid self-singular terms. The applied field, $\mathbf{H}_0$, itself does not exert any force on the beads since the gradient of this field is zero.

3.1.2 Mutual Dipole Model

In the fixed–dipole model, only the external field was considered in the calculation of the dipole moments of the beads. The mutual dipole model allows for the fields of the other beads to contribute to the magnetization of the bead under consideration. This model is equivalent to providing a solution of the N-sphere problem with spherical harmonic expansions truncated at the dipole level, $L = 1$ [59]. Therefore, each sphere behaves as though isolated and immersed in a field whose strength is equal the sum of the external field and the fields due to the other beads evaluated at the sphere's center. Consequently, the dipole moment of bead n is

$$\mathbf{m}_n = \frac{4}{3}\pi a^3 \chi_{eff} \left(\mathbf{H}_0 + \sum_{k=1, k\neq n}^{N} \mathbf{H}_{dip}^{k}(\mathbf{Y}_n - \mathbf{Y}_k) \right). \tag{3.7}$$

As the dipole moments of the beads may now differ, we label the dipole field in (3.7) with a superscript to denote the dipole moment producing the field. The dipole moments are unknown quantities and equations (3.4) and (3.7) provide the $3N \times 3N$ linear system of equations needed to determine the dipole moments. Once the dipole moments have been found the force on sphere n is then

$$\mathbf{F}^n = \mu_0 \boldsymbol{\nabla}_{\mathbf{Y}_n} \left(\mathbf{m}_n \cdot \sum_{k=1, k\neq n}^{N} \mathbf{H}_{dip}^{k}(\mathbf{Y}_n - \mathbf{Y}_k) \right). \tag{3.8}$$

To discuss the accuracy of the fixed and mutual dipole models, we compare the force between two spheres in a uniform field given by these models with the exact solution. The exact solution is provided by the calculation described in section 3.3. In Figure 3.1(a), we plot the force as a function of separation distance with the applied field parallel to the line of centers. In Figure 3.1(b), the applied field is perpendicular to the line of centers. In both of these two plots $\mu/\mu_0 = 2$ and $\chi = 1$. It should be noted that when the field is aligned with the line of centers, the force is attractive whereas when it is perpendicular, the force is repulsive. As one expects, the mutual dipole model performs better than the

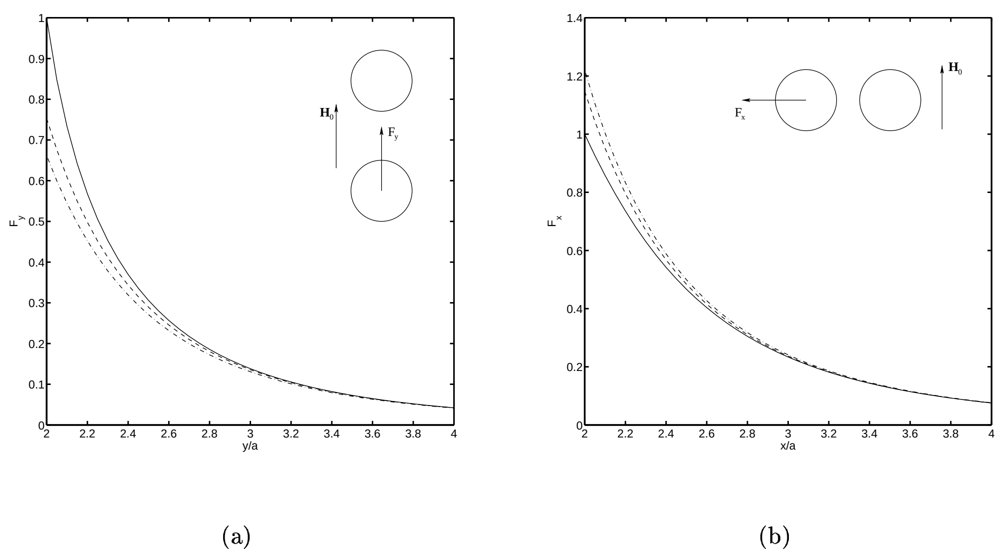

Figure 3.1: Values of the interbead force for two beads in a uniform field $\mathbf{H_0} = (0, 1, 0)$ with $\mu/\mu_0 = 2$. 3.1(a): F_y as a function of separation. The values of F_y are normalized by the value of F_y of the exact solution at separation $y/a = 2$. 3.1(b): F_x as a function of separation. The values of F_x are normalized by the value of F_x of the exact solution at separation $x/a = 2$. In the plots: $(- \cdot - \cdot -)$ fixed dipole; $(- - -)$ mutual dipole; (——) exact solution.

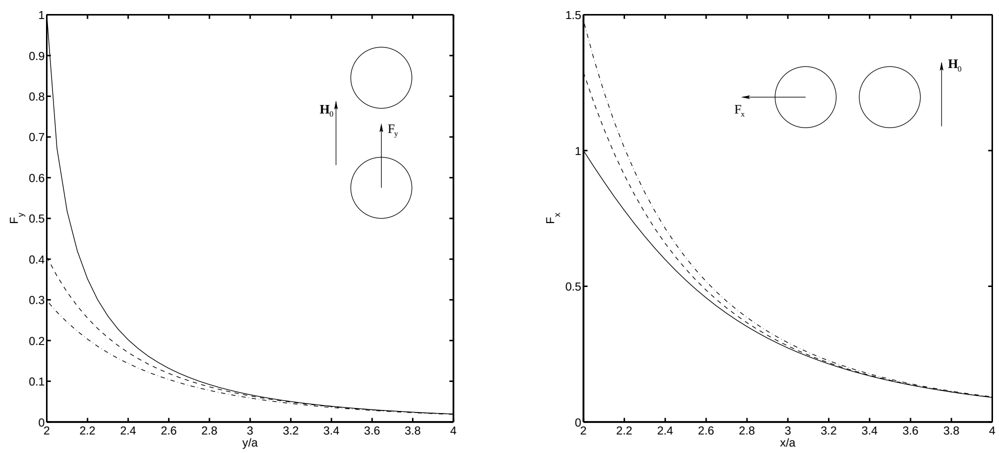

(a) (b)

Figure 3.2: Values of the interbead force for two beads in a uniform field $\mathbf{H_0} = (0, 1, 0)$ with $\mu/\mu_0 = 5$. 3.1(a): F_y as a function of separation. The values of F_y are normalized by the value of F_y of the exact solution at separation $y/a = 2$. 3.1(b): F_x as a function of separation. The values of F_x are normalized by the value of F_x of the exact solution at separation $x/a = 2$. In the plots: (– · – · –) fixed dipole; (– – –) mutual dipole; (——) exact solution.

fixed dipole model. Both models, however, break down as the particles come into contact and the neglected higher multipoles become important. Figures 3.2(a) and 3.2(b) show the same configurations with $\mu/\mu_0 = 5$. As compared with the $\mu/\mu_0 = 2$ cases, the difference in the force given by the dipole models and the exact calculation is much more severe at separations less than three radii.

Other examples involving sets of three particles or eight particles are discussed later in §3.3.2.

3.2 Finite–Dipole Model

We have presented two dipole models commonly used to handle the magnetic interactions between paramagnetic beads. Both the fixed-dipole and mutual dipole models required an $O(N^2)$ pairwise calculation to determine the interparticle forces and to determine the dipole moments, in the case of the mutual dipole model. In this section, we present a new dipole model based on finite distributions of current density. Such a model is easily handled by many numerical techniques and readily adapts to confined geometries where boundary conditions on the magnetic field need to be imposed. Also, the finite nature of the resulting field eliminates the need for exclusive sums that are present in the other models due to the self-induced singular terms.

3.2.1 Finite–Dipole Model: Single Particle

To begin, we discuss how to represent a given magnetization by a distribution of current. First, consider a distribution of current sources in a vacuum. For this situation, Maxwell's equations [59] are

$$\begin{aligned} \boldsymbol{\nabla} \cdot \mathbf{B} &= 0 \qquad (3.9) \\ \boldsymbol{\nabla} \times \mathbf{H} &= \mathbf{J} \qquad (3.10) \\ \mathbf{B} &= \mu_0 \mathbf{H}. \qquad (3.11) \end{aligned}$$

Equation (3.9) allows us to introduce the vector potential, $\mathbf{A}$, such that $\mathbf{B} = \boldsymbol{\nabla} \times \mathbf{A}$. The choice of the Coloumb gauge, $\boldsymbol{\nabla} \cdot \mathbf{A} = 0$, and the remaining two equations, (3.10) and

(3.11), reveal

$$\nabla^2 \mathbf{A} = -\mu_0 \mathbf{J}. \tag{3.12}$$

Now, consider a system absent of any current sources, but where an induced magnetization, $\mathbf{M}$ is present. Here, Maxwell's equations give [59]

$$\begin{aligned} \boldsymbol{\nabla} \cdot \mathbf{B} &= 0 && (3.13) \\ \boldsymbol{\nabla} \times \mathbf{H} &= \mathbf{0} && (3.14) \\ \mathbf{B} &= \mu_0 \left(\mathbf{H} + \mathbf{M} \right). && (3.15) \end{aligned}$$

We again introduce the vector potential, $\mathbf{A}$ and substitute the expression for $\mathbf{B}$ into the above equations and find

$$\nabla^2 \mathbf{A} = -\mu_0 \boldsymbol{\nabla} \times \mathbf{M}. \tag{3.16}$$

By comparing (3.12) and (3.16), we can represent the magnetization $\mathbf{M}$ by a current distribution $\mathbf{J}$ by requiring $\mathbf{J} = \boldsymbol{\nabla} \times \mathbf{M}$. The current density distribution associated with a point dipole located at the origin is [97]

$$\mathbf{J}_\delta(\mathbf{x}) = \boldsymbol{\nabla} \times \mathbf{m}\delta(\mathbf{x}). \tag{3.17}$$

We wish to to remove the singularity while maintaining the localized nature of the distribution. To do this, we replace the Dirac delta function with a smoothly varying Gaussian function

$$\Delta(\mathbf{x}) = (2\pi\sigma^2)^{-3/2} \exp(-r^2/2\sigma^2). \tag{3.18}$$

Therefore, our current density is now

$$\mathbf{J}_\Delta = \boldsymbol{\nabla} \times \mathbf{m}\Delta(\mathbf{x}) \tag{3.19}$$

and we are left with solving

$$\nabla^2 \mathbf{A}_\Delta = -\mu_0 \mathbf{J}_\Delta. \tag{3.20}$$

The solution to (3.20) is

$$\mathbf{A}_\Delta = \mu_0 \frac{\mathbf{m} \times \mathbf{x}}{r} G'(r) \tag{3.21}$$

with the functions $G(r)$ and its derivative $G'(r)$ given by, see [91],

$$G(r) = -\frac{1}{4\pi r}\text{erf}\left(\frac{r}{\sigma\sqrt{2}}\right) \tag{3.22}$$

$$G'(r) = \frac{1}{4\pi r^2}\left[\text{erf}\left(\frac{r}{\sigma\sqrt{2}}\right) - \left(\frac{r}{\sigma}\right)\left(\frac{2}{\pi}\right)^{1/2}\exp(-r^2/2\sigma^2)\right]. \tag{3.23}$$

The magnetic field $\mathbf{H}$ is then evaluated as,

$$\mathbf{H}_\Delta(\mathbf{x}) = \mathbf{m}\Delta(\mathbf{x}) - \boldsymbol{\nabla}\left(\mathbf{m}\cdot\boldsymbol{\nabla}G(r)\right) \tag{3.24}$$

or, explicitly,

$$\begin{aligned}\mathbf{H}_\Delta(\mathbf{x}) &= \frac{1}{4\pi}\left(\frac{3\mathbf{m}\cdot\mathbf{x}}{r^5}\mathbf{x} - \frac{\mathbf{m}}{r^3}\right)\text{erf}\left(\frac{r}{\sigma\sqrt{2}}\right) \\ &\quad + \left[\left(\mathbf{m} - \frac{\mathbf{m}\cdot\mathbf{x}}{r^2}\mathbf{x}\right) + \left(\mathbf{m} - \frac{3\mathbf{m}\cdot\mathbf{x}}{r^2}\mathbf{x}\right)\left(\frac{\sigma}{r}\right)^2\right]\Delta(\mathbf{x}).\end{aligned} \tag{3.25}$$

In (3.25), the second term decays exponentially fast, and the dipole field is achieved once r/σ is large enough that $\text{erf}(r/\sigma\sqrt{2})$ is close to one. The vector potential contours associated with (3.25) and those corresponding to a point dipole are depicted in Figure 3.3. We notice the finite–dipole current distribution smoothes out the field in the region near the origin. Physically, the finite–dipole current distribution can be thought of as a current loop whose finite radius is represented by the size of the Gaussian envelope, σ.

Since this model is to be applied to particles of finite size, the ratio of a/σ will determine how well the field just outside the bead is resolved. In Figures 3.4(a) and 3.4(b), we compare profiles of the magnetic field generated by finite–dipole current distributions of different σ with those of a point dipole field. Naturally, the approximation of the point dipole improves as we decrease the size of the Gaussian envelope, with the size ratio $a/\sigma = 4$ resolving nearly all the field at any distance from the surface of the sphere. Also, we observe the resolution of the field along the x-axis for a given a/σ is worse than along the y-axis.

3.2.2 Mutual Finite–Dipole Model

So far, we have presented the representation of a single dipole from a finite distribution of current. Based on these results, we now formulate an iterative method to compute the magnetic interactions of a collection of paramagnetic spheres. First, suppose the beads have

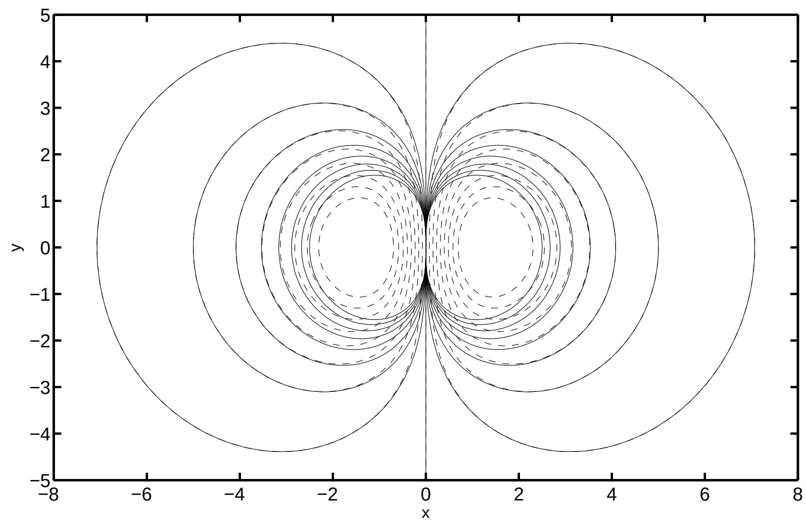

Figure 3.3: Vector potential contours for a point dipole (——) and a finite-dipole current distribution (– – –) with $\sigma = 1$. In both cases $\mathbf{m} = (0, 1, 0)$.

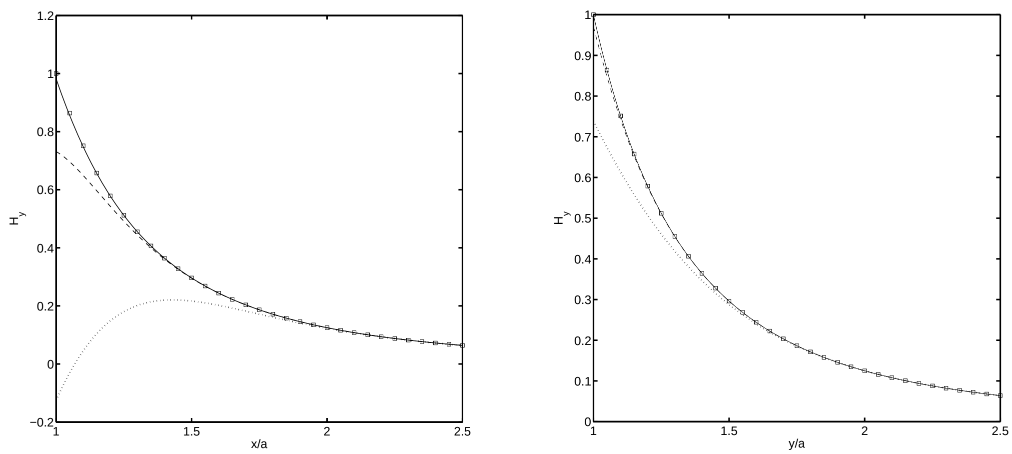

(a) (b)

Figure 3.4: Profiles of H_y for an isolated bead with $\mathbf{m} = 4\pi\chi a^3\mathbf{H_0}/3$, $\mathbf{H_0} = (0,1,0)$, and $\chi = 1$. 3.4(a): H_y along the x-axis where the values of H_y are normalized by the value of H_y of the true dipole at $x/a = 1$. 3.4(b): H_y along the y-axis with the values of H_y normalized by the value of H_y of the true dipole at $x/a = 1$. In the plots: $(\cdot\ \cdot\ \cdot\ \cdot\ \cdot)$ $a/\sigma = 2$; $(-\ -\ -)$ $a/\sigma = 3$; (——) $a/\sigma = 4$; $(\square)$ point dipole.

initial dipole moments $\mathbf{m}_{n,0}$ for $n = 1 \dots N$. These initial dipole moments may be those due to the external field or those from a previous timestep or iteration. Now, to motivate the method, we recall (3.7) and rewrite it as

$$\mathbf{m}_n = \frac{4}{3}\pi a^3 \chi_{eff} \left(\mathbf{H}_0 + \sum_{k=1, k\neq n}^{N} \int \mathbf{H}^k_{dip}(\mathbf{x} - \mathbf{Y}_k)\delta(\mathbf{x} - \mathbf{Y}_n) d^3\mathbf{x} \right). \tag{3.26}$$

In the mutual finite-dipole model, the dipole moment of bead n is given by

$$\mathbf{m}_n = \frac{4}{3}\pi a^3 \chi_{eff} \left(\mathbf{H}_0 + \sum_{k=1, k\neq n}^{N} \int \mathbf{H}^k_{\Delta}(\mathbf{x} - \mathbf{Y}_k)\Delta(\mathbf{x} - \mathbf{Y}_n) d^3\mathbf{x} \right). \tag{3.27}$$

In (3.27), the fields of the other beads are induced by moments $\mathbf{m}_{n,0}$ and given by (3.25). As a result everything on the right hand side of (3.27) is known. Also, the delta–function in the convolution is replaced by the Gaussian distribution (3.18). Therefore, rather than using the value of the field at a particle's center, a locally spatially averaged value of the field is considered in the computation of that particle's dipole moment.

In contrast to a singular point dipole, the field of a finite–dipole is finite and well defined at the dipole's location. We may then write

$$\mathbf{m}_n = \frac{4}{3}\pi a^3 \chi_{eff} \left(\int \left(\mathbf{H}_{tot}(\mathbf{x}) - \mathbf{H}^{(n)}_{\Delta}(\mathbf{x} - \mathbf{Y}_n) \right) \Delta(\mathbf{x} - \mathbf{Y}_n) d^3\mathbf{x} \right) \tag{3.28}$$

where

$$\mathbf{H}_{tot}(\mathbf{x}) = \mathbf{H}_0 + \sum_{k=1}^{N} \mathbf{H}^k_{\Delta}(\mathbf{x} - \mathbf{Y}_k). \tag{3.29}$$

Since the volume average of a particle's own field is

$$\int \mathbf{H}^n_{\Delta}(\mathbf{x} - \mathbf{Y}_n)\Delta(\mathbf{x} - \mathbf{Y}_n) d^3\mathbf{x} = \frac{\mathbf{m}_{n,0}}{12(\pi\sigma^2)^{3/2}}, \tag{3.30}$$

we arrive at

$$\mathbf{m}_n = \frac{4}{3}\pi a^3 \chi_{eff} \left(\int \mathbf{H}_{tot}(\mathbf{x})\Delta(\mathbf{x} - \mathbf{Y}_n) d^3\mathbf{x} - \frac{\mathbf{m}_{n,0}}{12(\pi\sigma^2)^{3/2}} \right). \tag{3.31}$$

Using the finite current density representation, the force on bead n is

$$\mathbf{F}^n = \mu_0 \int \mathbf{J}^n_\Delta \times (\mathbf{H}_{tot} - \mathbf{H}^n_\Delta(\mathbf{x} - \mathbf{Y}_n)\, d^3\mathbf{x}. \tag{3.32}$$

We may eliminate the need to subtract the self–induced forces since, in fact,

$$\int \mathbf{J}^n_\Delta \times \mathbf{H}^n_\Delta d^3\mathbf{x} = 0. \tag{3.33}$$

Therefore, the force on bead n is simply

$$\mathbf{F}^n = \mu_0 \int \mathbf{J}^n_\Delta \times \mathbf{H}_{tot} d^3\mathbf{x}. \tag{3.34}$$

Summarizing the above results, the numerical procedure with the mutual finite–dipole model is as follows:

1. Using the values of the dipole moments from a previous timestep or iteration, $\mathbf{m}_{n,0}$ for $n = 1 \ldots N$, construct the current density distribution $\sum_{n=1}^{N} \mathbf{J}_\Delta(\mathbf{x} - \mathbf{Y}_n)$.

2. Solve $\nabla^2\mathbf{A} = -\mu_0 \sum_{n=1}^{N} \mathbf{J}_\Delta(\mathbf{x} - \mathbf{Y}_n)$ for the vector potential $\mathbf{A}$ and compute $\mathbf{H} = \boldsymbol{\nabla} \times \mathbf{A}$.

3. Determine the new dipole moments

$$\mathbf{m}_n = \frac{4}{3}\pi a^3 \chi_{eff} \left(\int \mathbf{H}(\mathbf{x})\Delta(\mathbf{x} - \mathbf{Y}_n) d^3\mathbf{x} - \frac{\mathbf{m}_{n,0}}{12(\pi\sigma^2)^{3/2}} \right) \tag{3.35}$$

   for $n = 1 \ldots N$.

4. Check dipole moments for convergence. If $|\mathbf{m}_n - \mathbf{m}_{n,0}| > \epsilon$ then set $\mathbf{m}_{n,0} = \mathbf{m}_n$ and go to Step 1.

5. If $|\mathbf{m}_n - \mathbf{m}_{n,0}| < \epsilon$ then evaluate the forces on the beads

$$\mathbf{F}^n = \mu_0 \int \mathbf{J}_\Delta(\mathbf{x} - \mathbf{Y}_n) \times \mathbf{H}(x) d^3\mathbf{x} \tag{3.36}$$

   for $n = 1 \ldots N$.

The scheme described above can be implemented in variety of ways depending on the number of particles and the boundary conditions. For isolated configurations of few parti-

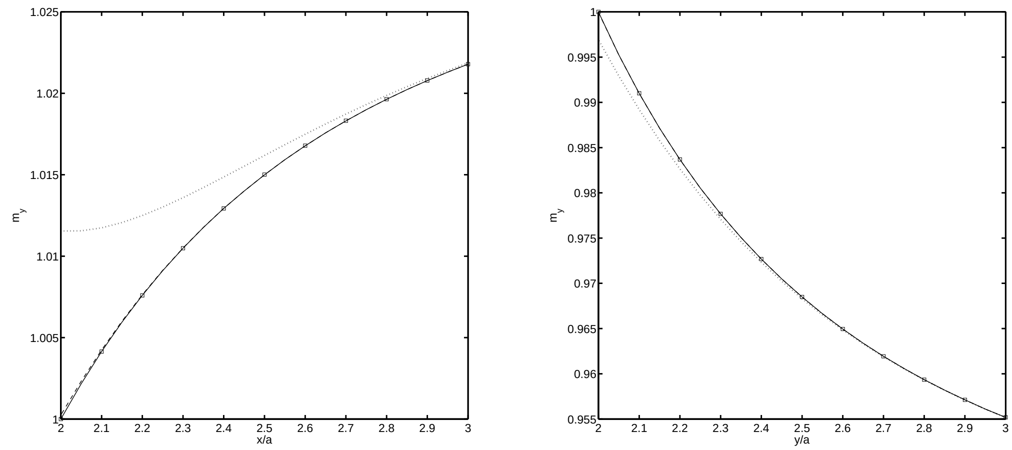

(a) (b)

Figure 3.5: Values of m_y as a function of separation for two beads in a uniform field $\mathbf{H_0} = (0,1,0)$ and $\mu/\mu_0 = 2$. 3.5(a): Separation along the x-axis. The values of m_y are normalized by the value of m_y of the mutual dipole at separation $x/a = 2$. 3.5(b): Separation along the y-axis. The values of m_y are normalized by the value of m_y of the mutual dipole at separation $y/a = 2$. In the plots: (....) $a/\sigma = 2$; (- - - -) $a/\sigma = 3$; (—) $a/\sigma = 4$; ($\square$) point dipole.

cles, one can construct a local grid for each particle and with the results (3.20) and (3.21) compute the integrals in steps (3) and (5). This method will, however, scale computationally as $O(N^2)$. In situations where many particles need to be considered, or boundaries are present, a fixed mesh over the entire domain can be constructed and a numerical solution for the vector potential (step (2)) can be determined. The integrals in steps (3) and (5) can then be computed using values of $\mathbf{H}_{tot}$ on nearby mesh points. The cost of computing the total magnetic field can be considered fixed. The cost of an additional particle is associated with the additional source term and the extra dipole and force integrations, which results in a method that scales computationally as $O(N)$. With the fixed mesh approach, there is the restriction that the grid spacing be small enough compared to the characteristic length scale of the distribution, σ as discussed in the following paragraph.

In order to analyze the how well the mutual finite–dipole model represents the mutual dipole model, we consider first two interacting spheres in a uniform magnetic field. In Fig. 3.5(a), we plot the dipole moments from the mutual dipole method and the mutual finite–

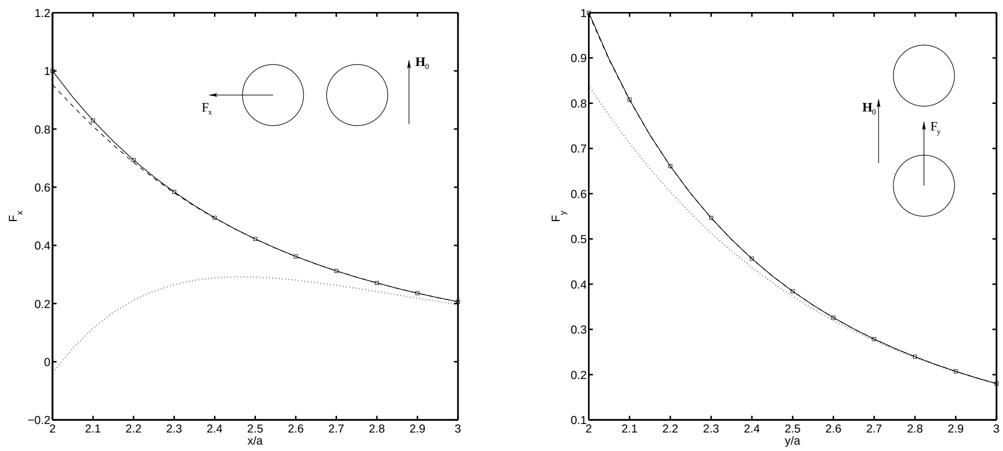

(a) (b)

Figure 3.6: Values of interparticle force for two beads in a uniform field $\mathbf{H_0} = (0, 1, 0)$ and $\mu/\mu_0 = 2$. 3.6(a): The values of F_x as a function of separation normalized by the value of F_x of the mutual dipole at separation $x/a = 2$. 3.6(b): Values of F_y versus separation normalized by the value of F_y of the mutual dipole at separation $y/a = 2$. In the plot: $(\cdot\cdot\cdot\cdot)$ $a/\sigma = 2$; $(---)$ $a/\sigma = 3$; (——) $a/\sigma = 4$; ($\square$) point dipole.

dipole model using several different values of a/σ with the applied field perpendicular to the axis of separation. Figure 3.5(b) shows the dipole moments when the field is parallel to the line of centers. Figures 3.6(a) and 3.6(b) show the force computed from (3.34) as a function of separation for the perpendicular field and the parallel field respectively. Provided the finite current distributions are sufficiently localized, the dipole moments and the forces for both configurations are nearly identical to those given by the mutual dipole method. We also notice that even though the field near the surface of a sphere is not fully resolved when $a/\sigma = 3$, the particle interactions are well accounted for. The results presented here are for $\mu/\mu_0 = 2$. Higher permeability ratios were also considered but not plotted here since the relative error for a choice of a/σ is not affected by this ratio.

Table 3.1: The magnitude of the magnetic dipole moment, $|\mathbf{m}|$, for each bead in an eight-bead chain with the chain axis aligned with the applied field, $|\mathbf{H}_0| = 1$ and $\chi = 1$. The dipole moments are computed using the mutual dipole method and the finite–dipole method with various values of a/σ.

Bead	Mutual Dipole	$a/\sigma = 3/2$	$a/\sigma = 2$	$a/\sigma = 5/2$	$a/\sigma = 3$
1	3.412583	3.358042	3.400500	3.411038	3.412467
2	3.627707	3.524409	3.604898	3.624793	3.627488
3	3.667280	3.558145	3.643083	3.664185	3.667074
4	3.677247	3.566890	3.652764	3.674115	3.677012

Table 3.2: The magnetic forces, F/μ_0, on each bead in an eight-bead chain with the chain axis aligned with the applied field, $|\mathbf{H}_0| = 1$ and $\chi = 1$. The forces are computed using the mutual dipole method and the finite–dipole method with various values of a/σ.

Bead	Mutual Dipole	$a/\sigma = 3/2$	$a/\sigma = 2$	$a/\sigma = 5/2$	$a/\sigma = 3$
1	0.399889	0.212705	0.338805	0.388854	0.398762
2	0.059832	0.041282	0.053863	0.058807	0.059732
3	0.014335	0.010425	0.013117	0.014129	0.014315
4	0.003119	0.002323	0.002874	0.003078	0.003115

Additionally, we have considered how well the mutual finite–dipole model recovers the dipolar interactions in a linear chain of particles. In this example, successive particles are in contact and the chain is aligned with the applied field, with $\mu/\mu_0 = 2$ or $\chi = 1$. Table 3.1 shows the dipole moments for each bead in the chain for a range of values for a/σ. For values of $a/\sigma \geq 2$ the resulting dipole moments compare well with those given by the mutual dipole model. To obtain an accurate quantification of magnetic force on each bead, see Table 3.2, requires a more localized distribution with values of $a/\sigma > 2.5$ yielding good estimates. It should be noted that the mutual dipole model underestimates the actual interaction forces between the particles due to the neglect of higher-order interaction effects. This is discussed in the next section.

In FCM, the ratio a/σ is chosen to exploit the self–induced velocity of a particle subject to an external body force by matching the local spatial average of this field to the settling velocity of the particle [91]. This specific choice further gives the proper balance between the work done on the fluid and the viscous dissipation. For the mutual finite–dipole model, the self–induced moment can not be exploited and must, in fact, be removed. As a result, there is no preferred choice of a/σ and its value may be chosen for numerical accuracy or efficiency. As a/σ increases, the dipole moments and the forces given by the finite–dipole model become more accurate, however, the spatial grid size must decrease to resolve the more localized Gaussian. The goal is to choose a value that correctly reproduces the point dipole interactions up to a certain distance but requires a reasonable number of grid points per particle radius. In the previous section, we saw that the force computed using the mutual dipole model begins to diverge from the exact calculation at a separation of three radii. With values $a/\sigma = 2.5$–3.0, the mutual finite–dipole model resolves the force at this separation. Also, with this range of values of a/σ, the resulting dipole moments agree quite well with the mutual dipole model at any separation. This is important for the inclusion of higher multipoles to be effective when using the procedure that will be described in Section 3.3.2.

3.2.3 Computational effort

In the standard mutual dipole model, the number of equations in (3.7) grows as the number of particles increases. An advantage of the finite–dipole model is its computational scalability. To include additional beads, one needs only to add the associated current density distribution of the extra bead to the equation for the vector potential. To illustrate how the computational cost increases as we increase the number of particles, we conducted several simulations of the aggregation of paramagnetic beads from a homogeneous random suspension in response to an external magnetic field. In addition to the magnetic forces we include

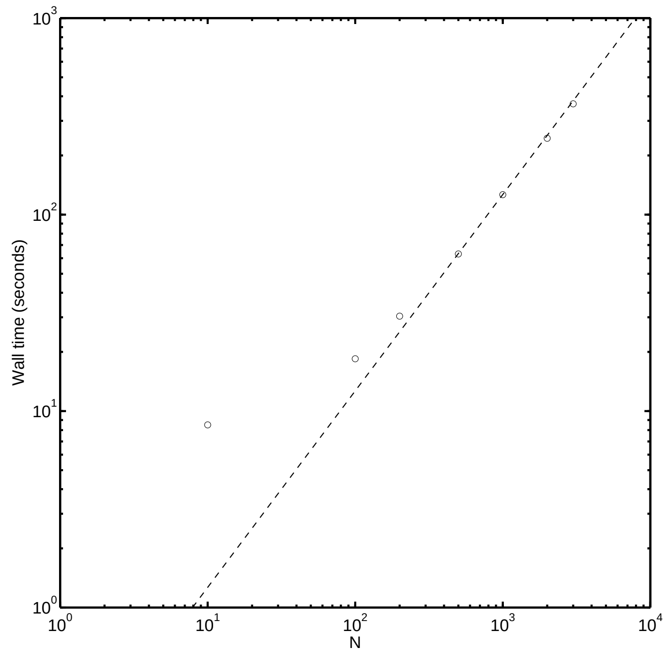

Figure 3.7: Computational time for one hundred time steps ($T = 100\Delta t$) associated with the mutual finite–dipole model as a function of the number of beads. (∘) measured wall time; (– – –) $O(N)$.

hydrodynamic and solid–body contact forces

$$\mathbf{F}^n_{hydro} + \mathbf{F}^n_{mag} + \mathbf{F}^n_{surf} = \mathbf{0}. \tag{3.37}$$

As described the in previous chapter, the surface force are determined using the pairwise collision barrier and the hydrodynamic interactions are provided by FCM. In this simulation, the boundary conditions in each direction are periodic so a Fourier collocation method with 144^3 grid points is used to solve for the magnetic vector potential. The hydrodynamic interactions are given by FCM and a Fourier collocation method with 96^3 grid points provides the solution to the Stokes equations. A different grid spacing is used for the magnetic field as opposed to the flow field since the length scale of the Gaussian in the finite–dipole model is two–thirds that of FCM. As the barrier forces vanish beyond separation distances of R_{ref}, a linked list algorithm is employed to handle efficiently the pairwise interactions. The simulation is run for 100 timesteps on two 2.4GHz Intel Xeon processors and the time needed to update the dipole moments is recorded. In the finite–dipole computations, it

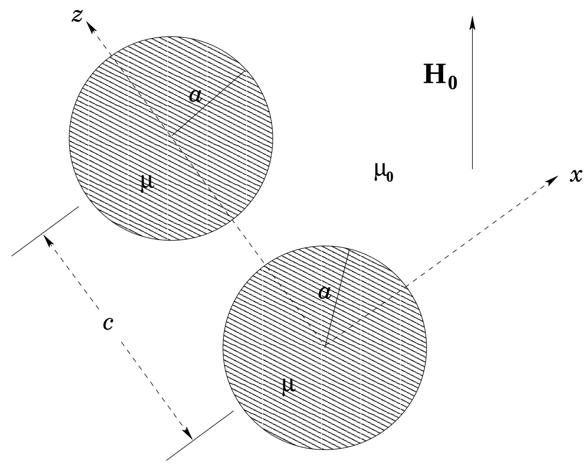

Figure 3.8: The two body problem.

typically required 2-3 iterations per timestep for the magnetic dipole moments to converge. This time is plotted in Fig. 3.7. When there are few particles, the simulation time remains constant as the time required to distribute the current sources on the grid is less than the fixed time associated with solving the equations. As we increase the number of beads and the computational time required to distribute the sources exceeds the solve time, we observe that the computational work scales as $O(N)$.

3.3 Incorporating Higher Multipoles

Until now, we have discussed various dipole models to account for the magnetic interactions of paramagnetic beads. As shown in figures 3.1(a) and 3.2(a), the dipole models provide reliable estimates for the inter-particle forces at larger separation distances but become inaccurate when the gap between particles is less than half a radius. In this section, we present the exact two-body calculation for the pairwise interaction of particles. The results will be then used to include the effects of higher-order multipole terms in a refined dipole model.

3.3.1 Solution to the Two-body Problem

Consider the general problem described in §2.3 with $N = 2$, $\mathbf{Y}_1 = (0, 0, c)$, $\mathbf{Y}_2 = (0, 0, 0)$ and the applied magnetic field resolved into components parallel to and orthogonal to the line of centers, $\mathbf{H}_0 = H_\perp \hat{\mathbf{x}} + H_{||}\hat{\mathbf{z}}$. The problem is depicted in Fig. 3.8 and is based on that performed in [61]. It is also a specific case considered in [23]. As stated earlier, the solution to this problem is given by a sum of spherical harmonics. For this problem we have

$$\Phi_n^{in} = \sum_{l=0}^{\infty} \sum_{m=0}^{1} \alpha_{lm}^{(n)} r_n^l P_l^m(\cos\theta_n) \cos m\phi \tag{3.38}$$

$$\Phi^{out} = -H_\perp x - H_{||} z + \sum_{n=1}^{2} \sum_{l=0}^{\infty} \sum_{m=0}^{1} \beta_{lm}^{(n)} \frac{P_l^m(\cos\theta_n)}{r_n^{l+1}} \cos m\phi \tag{3.39}$$

where (r_n, θ_n, ϕ) are the spherical coordinates of a system whose origin coincides with the center of sphere n. The associated Legendre functions are defined as

$$P_l^m(\cos\theta) = (-1)^m (1-\cos^2\theta)^{m/2} \frac{d^m}{d(\cos\theta)^m} P_l(\cos\theta). \tag{3.40}$$

In order find the coefficients $\alpha_{lm}^{(n)}$ and $\beta_{lm}^{(n)}$ that satisfy boundary conditions (2.30) and (2.31), we must express the general solution in terms of a single coordinate system. To accomplish this task, we employ the Hobson formula [61, 23] which state

$$\frac{P_l^m(\cos\theta_1)}{r_1^{l+1}} = \sum_{s=m}^{\infty} (-1)^{s+m} (-1)^{l+s} \binom{l+s}{s+m} \frac{r_2^s}{c^{l+s+1}} P_s^m(\cos\theta_2) \tag{3.41}$$

$$\frac{P_l^m(\cos\theta_2)}{r_2^{l+1}} = \sum_{s=m}^{\infty} (-1)^{s+m} \binom{l+s}{s+m} \frac{r_1^s}{c^{l+s+1}} P_s^m(\cos\theta_1) \tag{3.42}$$

On substituting the general solution into the boundary conditions, applying the Hobson formula, and eliminating $\alpha_{lm}^{(n)}$ we find that for each $m = 0, 1$

$$\begin{aligned} &\left(\tfrac{\mu}{\mu_0} l + l + 1\right) \beta_{lm}^{(1)} \\ &\quad + \textstyle\sum_{s=1}^{\infty} \beta_{sm}^{(2)} (-1)^{l+m} \binom{l+s}{s+m} \frac{a^{2l+1}}{c^{l+s+1}} \left(\frac{\mu}{\mu_0} l - l\right) = \delta_{1j} a^3 \left(1 - \frac{\mu}{\mu_0}\right) \\ &\qquad \times \left(\delta_{1m} H_\perp - \delta_{0m} H_{||}\right) \end{aligned} \tag{3.43}$$

$$\begin{aligned} &\left(\tfrac{\mu}{\mu_0} l + l + 1\right) \beta_{lm}^{(2)} \\ &\quad + \textstyle\sum_{s=1}^{\infty} \beta_{sm}^{(1)} (-1)^{l+s} (-1)^{l+m} \binom{l+s}{s+m} \frac{a^{2l+1}}{c^{l+s+1}} \left(\frac{\mu}{\mu_0} l - l\right) = \delta_{1j} a^3 \left(1 - \frac{\mu}{\mu_0}\right) \\ &\qquad \times \left(\delta_{1m} H_\perp - \delta_{0m} H_{||}\right) \end{aligned} \tag{3.44}$$

By including only a finite number of multipoles, $l = 0 \ldots L$, (3.43) and (3.44) establish two

$2L \times 2L$ linear systems of equations. Specifically, for each $m = 0, 1$ we need to solve

$$\left(\begin{array}{c|c} \mathbf{X} & \boldsymbol{\Delta}_m \\ \hline \boldsymbol{\Gamma}_m & \mathbf{X} \end{array}\right) \left(\begin{array}{c} \boldsymbol{\beta}_m^{(1)} \\ \hline \boldsymbol{\beta}_m^{(2)} \end{array}\right) = \left(\begin{array}{c} \mathbf{q}_m \\ \hline \mathbf{q}_m \end{array}\right) \tag{3.45}$$

where

$$\boldsymbol{\beta}_m^{(1)} = \left(\beta_{1m}^{(1)}, \beta_{2m}^{(1)}, \ldots, \beta_{Lm}^{(1)}\right)^{\mathrm{T}} \tag{3.46}$$

$$\boldsymbol{\beta}_m^{(2)} = \left(\beta_{1m}^{(2)}, \beta_{2m}^{(2)}, \ldots, \beta_{Lm}^{(2)}\right)^{\mathrm{T}} \tag{3.47}$$

$$\mathbf{q}_0 = \left(H_{\|} a^3 \left(1 - \mu/\mu_0\right), 0, \ldots, 0\right)^{\mathrm{T}} \tag{3.48}$$

$$\mathbf{q}_1 = \left(-H_{\perp} a^3 \left(1 - \mu/\mu_0\right), 0, \ldots, 0\right)^{\mathrm{T}} \tag{3.49}$$

and the $L \times L$ matrices are

$$X_{ij} = \delta_{ij} \left(i \frac{\mu}{\mu_0} + i + 1\right) \tag{3.50}$$

$$\Delta_{ij;m} = (-1)^{i+m} \left(i \frac{\mu}{\mu_0} - i\right) \binom{i+j}{j+m} \frac{a^{2i+1}}{c^{i+j+1}} \tag{3.51}$$

$$\Gamma_{ij;m} = (-1)^{i+j} \Delta_{ij;m}. \tag{3.52}$$

After solving for the $\beta_{lm}^{(n)}$, the contribution of the field from the particles in the fluid is

$$\begin{aligned} H_r = & \sum_{l=0}^{L} \sum_{m=0}^{1} \Bigg((l+1) \beta_{lm}^{(1)} \frac{P_l^m(\cos\theta_1)}{r_1^{l+2}} \\ & - \beta_{lm}^{(2)} \sum_{s=m}^{L} (-1)^{s+m} \binom{l+s}{s+m} s \frac{r_1^{s-1}}{c^{l+s+1}} P_s^m(\cos\theta_1) \Bigg) \cos m\phi \end{aligned} \tag{3.53}$$

$$\begin{aligned} H_\theta = & - \sum_{l=0}^{L} \sum_{m=0}^{1} \Bigg(\frac{\beta_{lm}^{(1)}}{r_1^{l+2}} \frac{dP_l^m(\cos\theta_1)}{d\theta_1} \\ & + \beta_{lm}^{(2)} \sum_{s=m}^{L} (-1)^{s+m} \binom{l+s}{s+m} \frac{r_1^{s-1}}{c^{l+s+1}} \frac{dP_s^m(\cos\theta_1)}{d\theta_1} \Bigg) \cos m\phi \end{aligned} \tag{3.54}$$

$$\begin{aligned} H_\phi = & \sum_{l=0}^{L} \Bigg(\frac{\beta_{l1}^{(1)}}{r_1^{l+2} \sin\theta_1} P_l^1(\cos\theta_1) \\ & + \beta_{l1}^{(2)} \sum_{s=1}^{L} (-1)^{s+1} \binom{l+s}{s+1} \frac{r_1^{s-1}}{c^{l+s+1} \sin\theta_1} P_s^1(\cos\theta_1) \Bigg) \sin\phi \end{aligned} \tag{3.55}$$

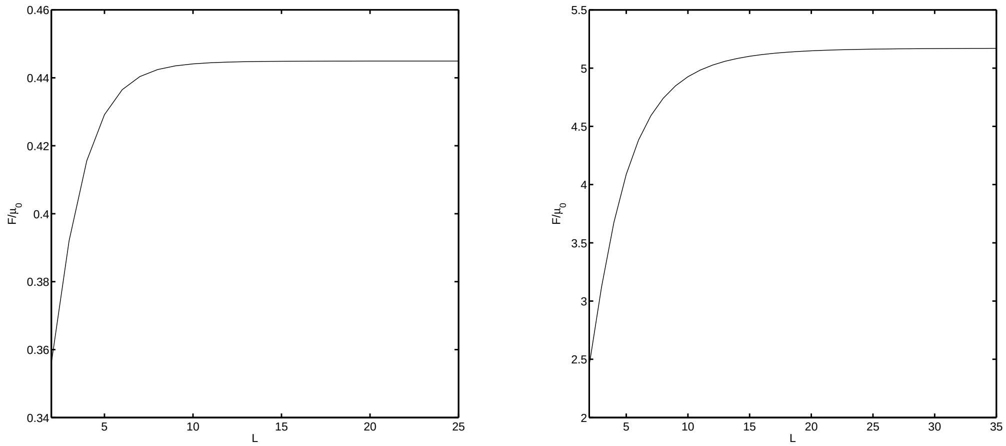

(a) (b)

Figure 3.9: Resulting attractive force as a function of the number of multipoles. The field is aligned with the line of centers and $|\mathbf{H_0}| = 1$. 3.9(a): $\mu/\mu_0 = 2$ and 3.9(b): $\mu/\mu_0 = 5$.

with

$$\frac{dP_l^m(\cos\theta)}{d\theta} = \frac{l\cos\theta P_l^m(\cos\theta) - (l+m)P_{l-1}^m(\cos\theta)}{\sin\theta}. \tag{3.56}$$

In (3.53)–(3.55), the coordinate system is (r_1, θ_1, ϕ), but using the Hobson formula, the field can also be expressed in terms of (r_2, θ_2, ϕ). With the field known, the Maxwell stress tensor, (2.33), can be formed and the force is then

$$F_x = \int_{r_n=a} T_{xr}\,dS \tag{3.57}$$

$$F_y = 0 \tag{3.58}$$

$$F_z = \int_{r_n=a} T_{zr}\,dS. \tag{3.59}$$

The simple form of the azimuthal dependence of the field allows the integration over ϕ to be evaluated analytically while the polynomial dependence of the field on $\cos\theta$ makes Gaussian integration viable for the integration over θ.

In the calculation, the infinite summation is truncated at a finite value, L. It is important that this value be large enough to include the important multipoles, but not so large that the matrix inversion becomes cumbersome. Figures 3.9(a) and 3.9(b) show the value of the force as a function of L between two spheres in contact with the axis of separation parallel to the applied field with $\mu/\mu_0 = 2$ and $\mu/\mu_0 = 5$ respectively. When $\mu/\mu_0 = 2$, having $L = 10$ resolves nearly all the force where as a value of $L = 20$ is needed to provide the same level of accuracy if $\mu/\mu_0 = 5$.

3.3.2 Inclusion of Two-Body effects into Dipole Models

We have already seen that as two bodies come into contact, the various dipole models fail to give an accurate representation of the magnetic force between a pair of particles. We, therefore, would like to incorporate higher order multipoles to yield correct estimates of the near contact force. One way to accomplish this is to compute the pairwise interactions using a higher multipole representation of the interactions [70]. While computing the forces this way will give a more accurate estimation of the near contact force, this method will not produce the correct asymptotic results for a many-body problem where the particles are widely separated. Consequently, we seek to develop a method that blends an N–body dipole calculation to determine the many body interactions and two-body, higher multipole calculations between particles that are sufficiently close. Such a model will provide the necessary adjustments for the near contact interactions while preserving the correct far-field forces given by the dipole computation. The method we propose to include the near field magnetic interactions is described here considering an ensemble of N spheres each of permeability μ and radius a.

Step 1: Far-field/Dipole Calculation

First, one must perform the N-body dipole calculation obtaining the resulting dipole moments $\mathbf{m}_n$ and magnetic forces $\mathbf{F}^n_{mag}$ on each bead n. This computation can be handled using either the mutual dipole or the mutual finite-dipole method depending on the choice of the user. The procedure to include the higher order multipoles is general and available to both methods.

Step 2: Determine if $c < R_c$

Since higher multipoles become important only near contact, we introduce R_c which defines the maximum inter-bead separation distance where higher multipoles will be included in the force calculations. Therefore, after computing the dipole interactions, one must determine if a pair of particles are close enough such that higher multipoles should be considered. In our simulations this is handled using a linked list algorithm [1] to avoid pairwise checking over all N particles and checking if the separation distance $c = |\mathbf{Y}_p - \mathbf{Y}_q|$ is less than R_c.

Step 3: Compute higher order multipoles

For each pair whose separation distance is less than R_c we perform the two body calculation (3.45) to determine the vectors $\boldsymbol{\beta}_m^{(1)}$ and $\boldsymbol{\beta}_m^{(2)}$ for $m = 0, 1$ which hold the coefficients for the L multipoles. In the two body calculation, the axes are aligned such that

$$\hat{\mathbf{z}} = \frac{\mathbf{Y}_p - \mathbf{Y}_q}{c} \tag{3.60}$$

$$\hat{\mathbf{x}} = \frac{\mathbf{H}_0 - (\mathbf{H}_0 \cdot \hat{\mathbf{z}})}{|\mathbf{H}_0 - (\mathbf{H}_0 \cdot \hat{\mathbf{z}})|} \tag{3.61}$$

$$\hat{\mathbf{y}} = \hat{\mathbf{z}} \times \hat{\mathbf{x}} \tag{3.62}$$

$$\tag{3.63}$$

so

$$H_{||} = \mathbf{H}_0 \cdot \hat{\mathbf{z}} \tag{3.64}$$

$$H_{\perp} = \mathbf{H}_0 \cdot \hat{\mathbf{x}}. \tag{3.65}$$

This calculation can performed on the fly at each time step, as needed, since only two $2L \times 2L$ linear systems need to be solved for each pair, and $L = 10$ for $\mu/\mu_0 = 2$ and $L = 20$ for $\mu/\mu_0 = 5$.

Step 4: Adjust two-body dipole moments to include far-field effects

Before computing the interparticle force, we first modify the dipole coefficients from the two body calculations $\beta_{1m}^{(p),2B}$ and $\beta_{1m}^{(q),2B}$ to include far-field effects. This allows information from the far-field to influence the two-body force calculation. With the relations

$$\beta_{10}^{(n),dip} = \frac{\mathbf{m}_n \cdot \hat{\mathbf{z}}}{4\pi a^3} \tag{3.66}$$

$$\beta_{11}^{(n),dip} = \frac{-\mathbf{m}_n \cdot \hat{\mathbf{x}}}{4\pi a^3} \tag{3.67}$$

we determine the new dipole coefficients

$$\beta_{1m}^{(n)} = \beta_{1m}^{(n),2B} + \beta_{1m}^{(n),dip} - \beta_{1m}^{(n),2Bdip} \tag{3.68}$$

for each $m = 0, 1$. In (3.68), $\beta_{1m}^{(n),2Bdip}$ is given by a dipole calculation where only the interactions of the two bodies are considered. This value corresponds to the outer expansion of the inner solution and is the overlap of the two solutions that must be subtracted to avoid it being counted twice.

Step 5: Determine the resulting field

With the modified coefficients $\beta_{lm}^{(n)}$ we now determine the field in the fluid phase (3.53)–(3.55). In general, one needs to add the out of plane component of the field due to the out of plane component of the dipole moment from the far-field calculation

$$\mathbf{H} = -\boldsymbol{\nabla}\Phi_y = -\frac{\mathbf{m}_n \cdot \hat{\mathbf{y}}}{4\pi a^3} \frac{P_1^1(\cos\theta)\sin\phi}{r^2}. \tag{3.69}$$

Step 6: Form and evaluate the Maxwell stress tensor

Once the components of the field are found, the Maxwell stress tensor (2.33) can be determined and evaluated over the surface of each particle to obtain the force (2.34), $\mathbf{F}_{mag}^{(n),2B}$.

Step 7: Correct the total magnetic force

The total magnetic force on a given particle must now be adjusted to replace the magnetic force between particles p and q with the corrected force $\mathbf{F}_{mag}^{pq,2B}$. The total force is

$$\mathbf{F}^p = \mathbf{F}_{dip}^p + \mathbf{F}_{2B}^{pq} - \mathbf{F}_{dip2B}^{pq} \tag{3.70}$$

$$\mathbf{F}^q = \mathbf{F}_{dip}^q - \mathbf{F}_{2B}^{pq} + \mathbf{F}_{dip2B}^{pq} \tag{3.71}$$

where $\mathbf{F}_{dip2B}^{pq}$ is the dipolar force between particles p and q.

3.3.3 Example results

To test the effectiveness of this procedure, we consider several three-particle configurations with different values of μ/μ_0. Two-particle problems are not considered since the inclusion

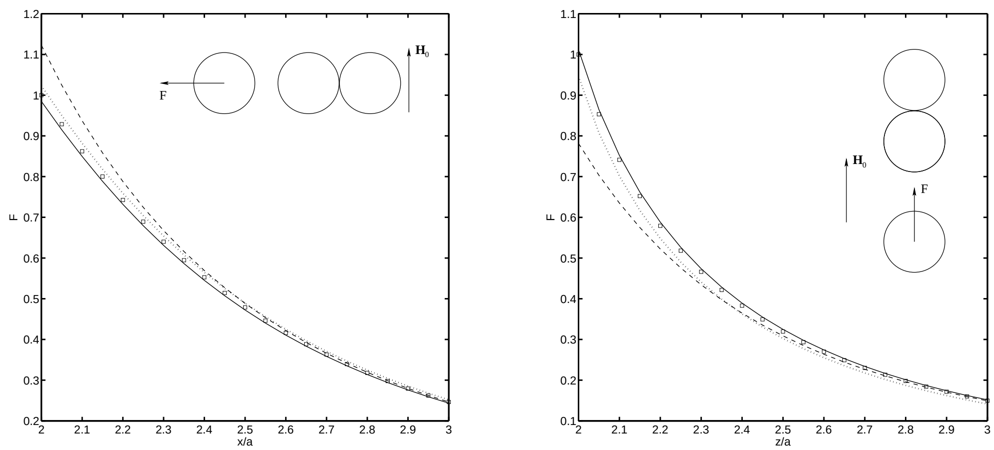

(a) (b)

Figure 3.10: Force on a bead due to a doublet with $\mu/\mu_0 = 2$. The data are normalized by the value of the exact solution at contact. 3.10(a): The applied field is perpendicular to the separation axis. 3.10(a): The applied field is parallel to the separation axis. In the plots: $(\cdot\ \cdot\ \cdot\ \cdot\ \cdot)$ two body calculation; $(-\ -\ -)$ mutual dipole; (——) inclusion model; ($\Box$) exact solution.

procedure, described above, already gives exact results for the interparticle force. For the three–body problems, the interparticle forces are computed in turn from the mutual dipole method, a combination of simple pairwise two–body calculations [70] and the inclusion model. These results are compared to the exact forces. The results of the two–body calculation are obtained by summing the forces from the two-body calculation for each pair in turn [70]. Figures 3.10(a) and 3.10(b) show the force on a bead due to a collinear pair of beads in contact. The axis of separation is aligned with the axis of the doublet pair and the applied magnetic field is taken in turn to be perpendicular and parallel to this direction. The magnetic susceptibility is $\chi = 1$ and $\mu/\mu_0 = 2$. When the magnetic field is aligned with the axis of the three-particle chain the results of the inclusion model agree well with the exact values. In this configuration, the forces are attractive and the agreement indicates how well the models can characterize the yield behavior of the chain structures commonly found in MR fluids. When the field is perpendicular to the chain, the forces are repulsive and the particles tend to separate. The error from the inclusion model is small and is a significant improvement over the estimates from the other methods. In figures 3.11(a) and 3.11(b), the same bead configurations are used, but now $\mu/\mu_0 = 5$.

The trends in the discrepancies in the differences between the models and the exact computations are the same for both permeability ratios but more dramatic in the case of $\mu/\mu_0 = 5$ where the higher multipoles are more influential. In each case, the mutual dipole method performed well at large separations, but diverged from the exact force near contact. Simply adding the forces from pairwise two–body calculations gives a better estimate of the force near contact and a good estimate at any separation when the chain axis is perpendicular to the applied field. This method does, however, suffer from not being able to provide an accurate characterization of the far-field force where the chain axis is aligned with the applied field. For the higher permeability ratio, the relative error at contact is still large at 15% (Figure 3.11(b)). In each of these three–particle configurations and for both permeability ratios, we see the inclusion of the higher multipoles from the two body calculation with the many-body dipole model provides the force enhancement needed to resolve the near contact interactions while also ensuring the proper asymptotic behavior as the separation increases. Of the four cases considered here, the largest relative error is approximately 5% (Figure 3.11(b)).

The inclusion model may be applied to the example of a collinear chain of eight para-

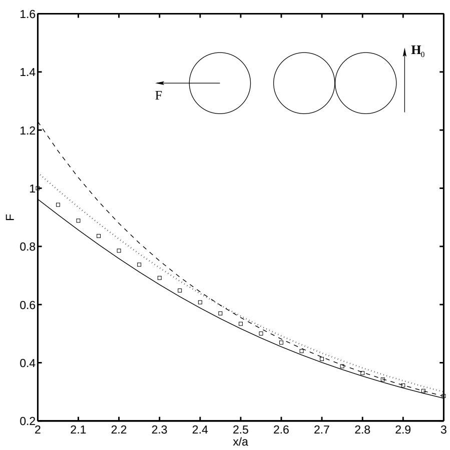

(a)

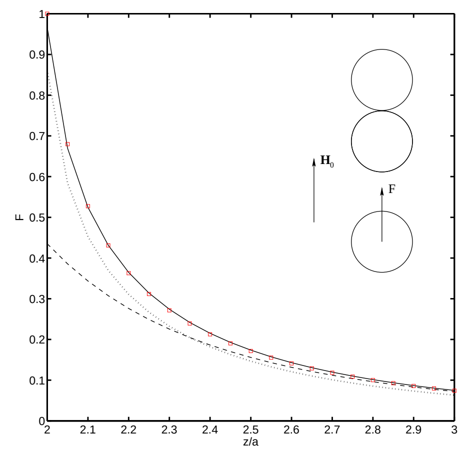

(b)

Figure 3.11: Force on a bead due to a doublet with $\mu/\mu_0 = 5$. The data are normalized by the value of the exact solution at contact. 3.10(a): The applied field is perpendicular to the separation axis. 3.10(a): The applied field is parallel to the separation axis. In the plots: $(\cdot\ \cdot\ \cdot\ \cdot\ \cdot)$ two body calculation; $(-\ -\ -)$ mutual dipole; (——) inclusion model; $(\square)$ exact solution.

Table 3.3: The resultant magnetic forces, F/μ_0, on each bead in an eight-bead chain with the chain axis aligned with an applied field of unit magnitude, $|\mathbf{H}_0| = 1$. The forces are computed using different models described here. Only the forces on beads 1–4 are provided since the forces on 5–8 are equal and opposite to these values.

Bead	Fixed Dipole	Mutual Dipole	Two Body	Inclusion Method	Exact
1	0.318540	0.399889	0.469333	0.514543	0.507733
2	0.023898	0.059832	0.024279	0.063490	0.056234
3	0.005258	0.014335	0.005279	0.015035	0.013690
4	0.001150	0.003119	0.001153	0.003260	0.003052

magnetic beads in contact, previously considered in section 3.2.2, with the applied field aligned with the chain. The resultant magnetic forces on each particle in the chain are evaluated using the different methods and listed in Table 3.3. The results are compared to the exact values. The inclusion procedure provides a good quantification of the force on each particle resolving the underestimate associated with the mutual dipole method at the end, and the pairwise two-body calculation in the middle. The attractive magnetic force between any two beads in the chain is given by summing the resultant forces from the end of the chain. The attractive force is strongest between the two beads, numbers 4 and 5, at the center of the chain and diminishes towards the ends. It should be noted that for this specific configuration the resultant force in the middle of the chain is dominated by the dipole interactions.

The inclusion model performs exceptionally well when the particles are distributed along a line. Problems arise, however, when the configuration is no longer collinear. These configurations are present at high volume fractions [89] or when the suspension is subject to a rapidly rotating field [93]. In Figure 3.12, a triangular configuration is subject to a uniform field. The forces are attractive. The results are compared with the exact force taken from [23]. In this case, the 40% error in the force at contact is reduced to 10% with the inclusion model. Although the inclusion model provides a better approximation of the force than the other models, its performance is not as good as it was in the previous cases. Extending the far-field calculation to include quadrupole moments may be a way to improve this result.

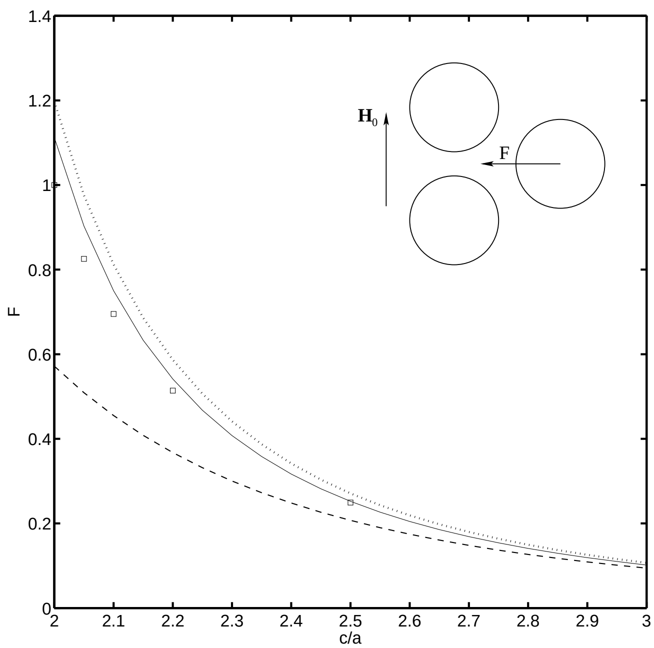

Figure 3.12: Force on a bead in a triangular arrangement. The configuration is depicted in the drawing with the bead in question indicated. The data are normalized by the value of the exact solution at contact. The exact computation is provided by [23]. In the plot: (· · · · ·) two body calculation; (– – –) mutual dipole; (——) inclusion model; (□) exact solution.

3.4 Summary

The purpose of this study is to develop a method to estimate accurately and efficiently the magnetic forces between paramagnetic particles that is applicable for systems of thousands of particles. An accurate quantification of the interparticle forces is necessary to determine the rheological properties of MR fluids or the performance of micro-fluidic devices, where unsteady magnetic fields or shear flows introduce viscous stresses on the self-assembled chains. Accurately describing the yield strength and deformation of the structure while considering a large number of particles are necessary to determine the properties of the bulk suspension.

In the preceding sections, we have presented and described a finite–dipole model which resolves the many-body dipole interactions in MR fluids. In this model, the induced magnetization of a particle is represented as a localized Gaussian distribution of current, with characteristic length scale σ, that is then a source term in the Poisson equation for the vector potential of the magnetic field. This equation can be solved using any standard numerical solver, whether it be a finite difference or spectral code, and may also accommodate different boundary conditions on the domain. Further, the results present here can be used in the formulation of a particle-mesh Ewald method [29] if one is interested in recovering the point–dipole model. The computational work associated with the finite–dipole model comprises a fixed cost associated with solving the Poisson equation and an $O(N)$ growth associated with distributing the current sources over the grid points. A fixed numerical mesh is commonly used for simulating the fluid dynamics of a suspension of paramagnetic particles and the extra cost of solving the additional Poisson equation represents a modest increase in the overall computational effort. The choice of a/σ is discussed in the context of providing an accurate description of the force between point dipoles while ensuring the number of grid points in a particle radius is not too large. Although only the interactions between particles of the same size and magnetic properties are considered, the finite–dipole description can readily be extended to cases of polydispersity in the particle radius or the magnetic susceptibility.

In order to capture the near-field interactions of particles, the mutual dipole and finite dipole models have been modified to include locally higher-order multipole terms through a pairwise interaction scheme. This is based on the exact solution for two paramagnetic particles placed in a locally uniform magnetic field. This inclusion scheme is self-consistent in that it preserves both the correct far-field and near-field expansion limits, and removes the overlapping terms of the expansions. Although the inclusion scheme is intended for use with the finite–dipole model, its formulations is general and available for use in conjunction with other dipole or higher-order multipole models. The procedure yields very accurate solutions to collinear three-body problems. The scheme is not as accurate when considering other configurations but represents a significant improvement over existing methods. Further improvements may be possible by including more information from the far field (i.e. quadrupole moments). Introducing nonuniform magnetic fields into the two-body, near-field model would significantly increase the complexity of the pairwise computations.

Chapter 4

The dynamics of self-assembled structures of paramagnetic beads in suspensions

4.1 Introduction

In a variety of the microfluidic and MR fluid devices discussed in Chapter 1, a suspension or a small group of paramagnetic particles is subject to a time-dependent applied field or an external flow field. In these situations, the motion of the structures leads to hydrodynamic forces that may deform or break the aggregates. A linear shear flow, for example, will rotate a chain and apply straining forces that may pull it apart (Figure 4.1). Similarly, a chain subject to a rotating field will experience hydrodynamic forces the prevent it from remaining aligned with the applied field. The *Mason number*, Ma, provides a measure of the relative strength of the viscous forces as compared the to the magnetic forces and its definition depends on the situation being considered. For a shear flow, the Mason number is typically defined as [88]

$$Ma_{shear} = \frac{\eta\gamma}{2\mu_0\beta^2 H_0^2} \tag{4.1}$$

where γ is the shear rate, η is the fluid viscosity, μ_0 is the permeability of free-space, H_0 is the magnitude of the applied field, and $\beta = \chi/(\chi+3)$ with χ being the particle susceptibility.

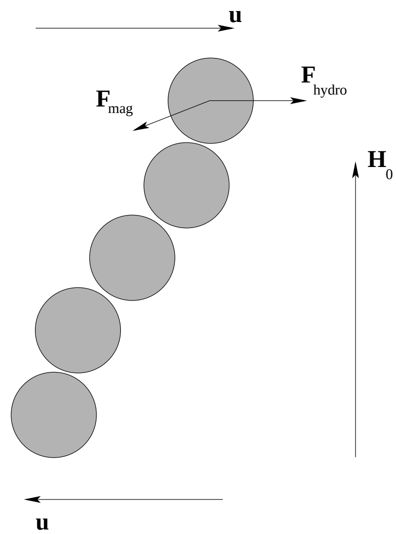

Figure 4.1: Sketch of a chain of $N = 5$ beads deforming in response to a shear flow.

When a rotating applied field is considered, the usual definition becomes [93]

$$Ma_{rot} = \frac{144\eta\omega}{\mu_0 \chi_{eff}^2 H_0^2}, \text{ or } \frac{16\eta\omega}{\mu_0 \beta^2 H_0^2} \tag{4.2}$$

where $\chi_{eff} = 3\chi/(\chi + 3) = 3\beta$ and ω is the angular frequency of the applied field. The equilibrium lengths and shapes of chains of paramagnetic particles in shear flows and rotating fields will be affected by the value of Ma_{shear} and Ma_{rot}. For a chain of N beads one can introduce a critical Mason number, Ma_{shear}^{crit} or Ma_{rot}^{crit}, that is defined as the maximum value of Ma_{shear} or Ma_{rot} for which the chain will not break. The value of Ma_{shear} or Ma_{rot} will also affect the properties of suspensions of paramagnetic beads subject to flow fields or time-dependent applied fields. For example, the value of the Ma_{rot} can dramatically affect the structures formed by particles in suspensions subject to rotating fields [93]. At low values of Ma_{rot}, the particles will aggregate to form chains that rotate nearly aligned with the applied field. As Ma_{rot} increases, viscous stresses will begin to deform the chains causing them to break decreasing the average chain length. When $Ma_{rot} > 1$, the suspension structure changes abruptly to where one now observes oscillating binary pairs and small, planar clusters.

Using the simulation techniques described in the previous two chapters we have conducted a variety of simulations to understand the behavior of collections of both a small group of several and suspensions of thousands of particles. We first consider the dynamics of a pair of particles in a rotating field. Above a critical frequency of the applied field, the separation distance between the particles will undergo frequency dependent oscillations. By conducting simulations of this behavior, we quantify the effects of the collision barrier on the resulting dynamics. We then examine the equilibrium shapes achieved by chains of paramagnetic particles in shear flows and rotating fields. In each case, we obtain the critical Mason number over a range of chain lengths. To show the importance of correctly resolving the hydrodynamic interactions along the length of the chain, the simulation results are compared with values of the critical Mason number obtained by a simple Stokes drag law chain model [88, 94]. Finally, we consider the behavior of a suspension of particles allowed to aggregate under the influence of a rotating field and compare these results with similar experiments [93].

4.2 Doublet dynamics in a rotating field

We consider first the dynamics of an isolated binary pair of paramagnetic particles subject to a rotating field. The viscous forces create a phase lag in the turning of the doublet relative to the applied magnetic field. Below a critical Mason number Ma_{rot}^{crit}, the vector joining the centers will be at a fixed angle ϕ relative to the applied field such that the interparticle magnetic forces will remain attractive causing the two particles to remain in contact. Above Ma_{rot}^{crit}, ϕ will increase to where the magnetic forces change from being attractive to repulsive. In this regime, the separation distance between the particles oscillates in time (Figure 4.2). The frequency and magnitude of the oscillations will depend on the frequency of the applied field (4.3) with the magnitude decreasing and the frequency increasing with Ma_{rot}. The experiments by Helgesen *et al.* [51] concerning a pair of nonmagnetic particles in a ferrofluid were the first to observe these dynamics. While [51] examined changes in the non-constant rotational frequency of the doublet axis, more recent studies quantified the frequency and magnitude of the oscillations [98] and the effects of surface roughness on the resulting dynamics [63].

Although the overall dynamics are governed by the hydrodynamic and magnetic interactions, differences in the near-contact dynamics can affect the magnitude and frequency of the oscillations [63]. In Figure 4.3, we compare results from two different simulations with the experimentally measured oscillations taken from [98]. In the first simulation, we resolve

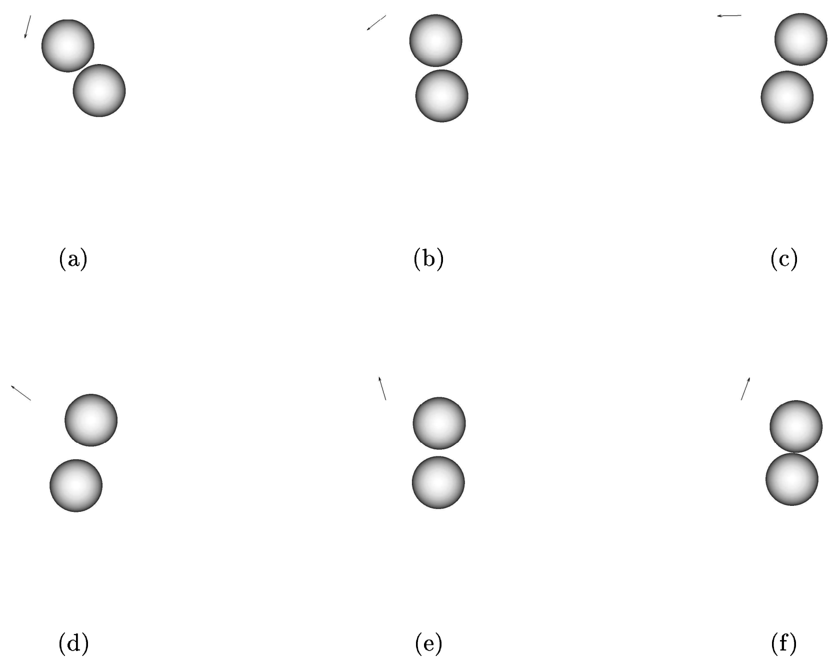

Figure 4.2: A pair of paramagnetic beads in a clockwise rotating field with $Ma_{rot} > Ma_{rot}^{crit}$. The images show the beads over the course of one oscillation. The arrows indicate the direction of the applied field. In (c) and (d) the force between the beads is repulsive.

completely the hydrodynamic interactions between the particles using the lubrication force correction for FCM [28]. In the second simulation, we ignore the lubrication effects, but employ the short-range collision barrier (2.38). When only lubrication effects are considered, the resulting oscillations are only a fraction of those determined experimentally. The simulation employing the collision barrier, however, provide oscillations that are comparable those found by [98]. These results indicate that particle surface roughness and/or interparticle surface forces are present and are captured by the generic collision barrier in the simulations.

Further, we may examine how the oscillatory dynamics will change with variations in R_{ref}. The balance between the collision barrier force and the magnetic attractive force established a minimum separation distance between the particles. This sets an effective hydrodynamic radius of the particles and a maximum value of the interparticle magnetic forces. To examine these effects, we vary the cut-off radius over the range $2.025a < R_{ref} < 2.3a$. For a bead with a radius of $a = 1\mu m$, this range corresponds to the forces acting over $25 - 300nm$ from the surface of the particle. The barrier force for the different values of R_{ref} are shown in Figure 4.4.

In varying R_{ref} over the range considered here, we found that the critical Mason number will increase by approximately ≈20% (Table 4.1). For lower values of R_{ref}, the minimum separation distance is reduced and the hydrodynamic and magnetic forces keeping the particles in contact increase. The magnitude of the oscillations are determined over a range of Ma_{rot} above Ma_{rot}^{crit} and are shown in Figure 4.5. Above the critical frequency, we found the magnitude of the oscillations are reduced when the value of R_{ref} is decreased. Decreasing R_{ref} will uniformly shift the magnitudes to lower values, but the scaling with frequency is also found to be slightly modified. Along with the magnitude, we find that the frequency of the oscillations to be affected by the value of R_{ref} (Figure 4.6). The ratio of the oscillation frequency to the frequency of the applied field is lower for lower values of R_{ref}. Here, the values of this ratio do collapse onto a single curve when plotted against $Ma_{rot} - Ma_{rot}^{crit}$.

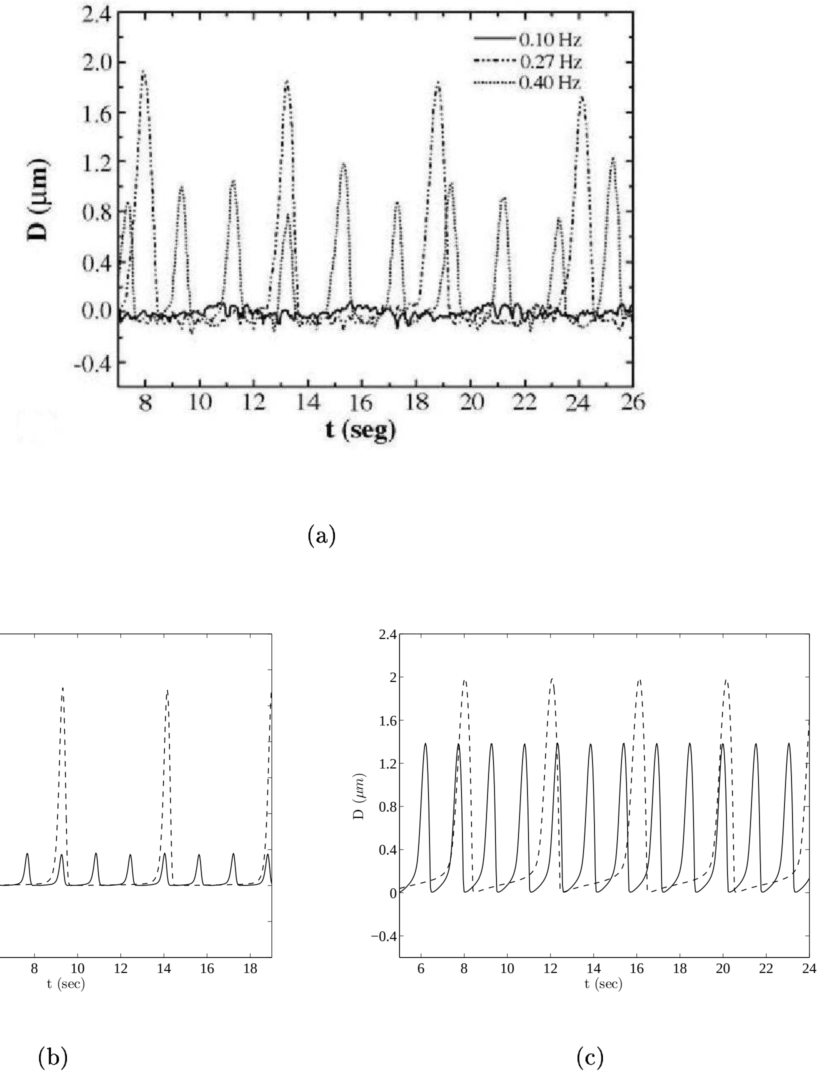

Figure 4.3: Oscillations in the distance between particle surfaces for an oscillating doublet as given by (a) experiments of [98], (b) FCM simulations with lubrication corrections and (c) standard FCM simulations with the collision barrier ($F_{ref} = 1.05F_{con}$ and $R_{ref} = 2.1a$). In the experiments the critical frequency was determined to be $f_{crit} \approx 0.25Hz$ and $a = 4\mu m$. In (b) and (c), the dashed line corresponds to $f = 0.27Hz$ in the experiments while the solid line corresponds to $f = 0.4Hz$.

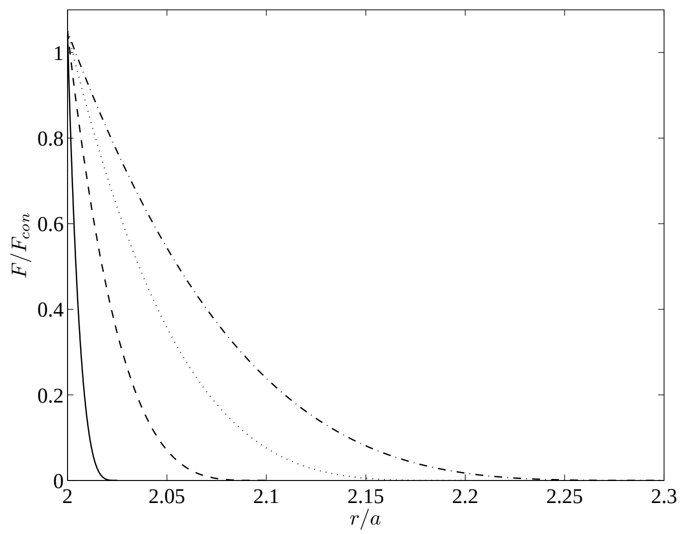

Figure 4.4: Normalized collision barrier force F/F_{con} as a function of separation distance for $R_{ref} = 2.025a$ (solid line), $R_{ref} = 2.1a$ (dashed line), $R_{ref} = 2.2a$ (dotted line) and $R_{ref} = 2.3a$ (dash-dotted line).

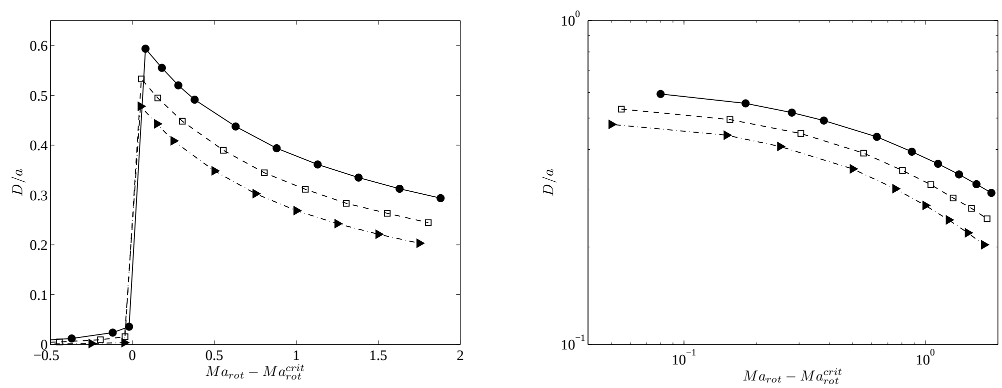

(a) (b)

Figure 4.5: Magnitude of the oscillations versus $Ma_{rot} - Ma_{rot}^{crit}$ (a) and again in log-log scale (b). The solid line with the circular markers corresponds to $R_{ref} = 2.2$, the dashed line with open square markers $R_{ref} = 2.1$, and the dash-dotted line with triangles $R_{ref} = 2.025$.

R_{ref}	Ma_{rot}^{crit}
2.025a	1.25
2.05a	1.23
2.1a	1.195
2.15a	1.158
2.2a	1.12
2.25a	1.09
2.3a	1.045

Table 4.1: The critical Mason number, Ma_{rot}^{crit}, for each value of R_{ref} considered.

4.3 Deformation and fracture of chains in shear flows and rotating fields

The unique rheological properties of MR fluid are provided by the linear structures that form parallel to the applied field and resist deformation as a result of an applied shear. In addition, quantifying the yield of the chains in applied flow fields or in time dependent fields is important to the operation of microfluidic devices employing the self-assembled structures. Understanding the behavior of a chain of particles in a linear shear flow or a rotating applied field provides information essential to quantifying rheology properties and the performance of microdevices. We conduct simulations of both these scenarios and in each case ascertain the critical Mason number for a chain of N beads. This behavior has been previously examined using drag based chain models [88, 94, 99]. We compare our results with these models and demonstrate the importance of the hydrodynamic interactions along the length of the chain.

4.3.1 Chain in a shear flow

In 1922, Jeffery [60] demonstrated that a torque-free spheroidal particle in the linear shear flow

$$\mathbf{u} = \gamma y \hat{\mathbf{x}} \tag{4.3}$$

that has its axis of symmetry exclusively in the xy-plane, will rotate with a period

$$T = \frac{2\pi}{\gamma}\left(r + \frac{1}{r}\right) \tag{4.4}$$

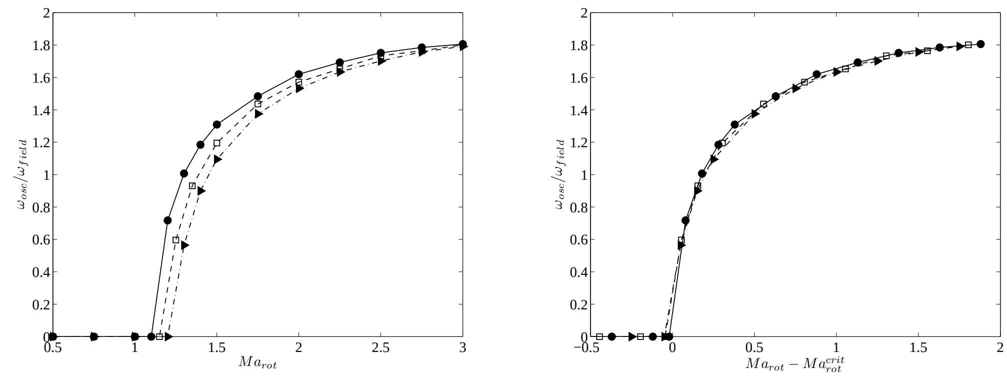

(a) (b)

Figure 4.6: Frequency of the oscillations divided by the frequency of the applied field versus (a) $Ma_{rot} - Ma_{rot}^{crit}$ and (b) $Ma_{rot} - Ma_{rot}^{crit}$. The solid line with the circular markers corresponds to $R_{ref} = 2.2$, the dashed line with open square markers $R_{ref} = 2.1$, and the dash-dotted line with triangles $R_{ref} = 2.025$.

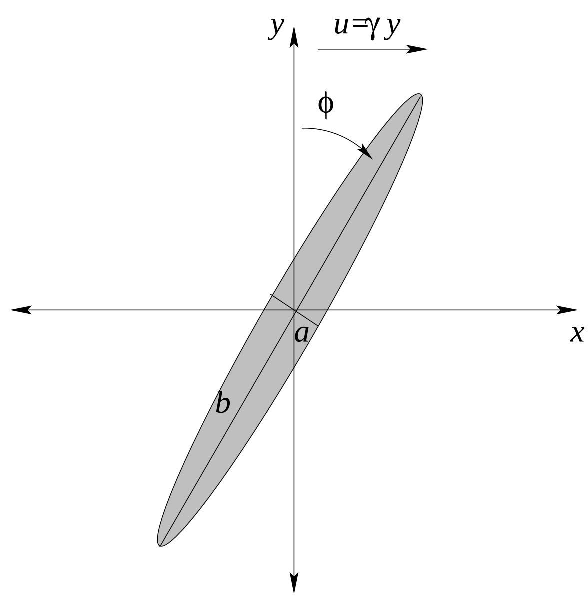

Figure 4.7: An illustration of an ellipsoidal particle in a linear shear flow.

where the angle ϕ (Figure 4.7) as a function of time is given by

$$\tan\phi = r\tan\left(\frac{2\pi t}{T}\right). \tag{4.5}$$

where $r = b/a$ is the spheroidal axis ratio. Zia, Cox and Mason [122] demonstrated that any axisymmetric body, including a chain of spherical particles, will behave in this manner with an *effective* spheroidal axis ratio r_e.

The period of a Jeffrey orbit can be dramatically altered by introducing an applied torque on the object. Goldsmith and Mason [46] examined the behavior of a dielectric spheroid subject to a shear flow (4.3) and an electric field in the y-direction. They found that below a critical value of the magnitude of the applied field, the particle will still make a complete orbit, but the time spent in the first and third quadrants is lengthened while the time in the second and fourth quadrants is diminished. Above a critical value of the applied field, the spheroid will not be able to complete its orbit and will reach equilibrium at a fixed angle ϕ_{equil} measured from the y-axis.

The situation may be further modified if the structure is no longer rigid and allowed to deform or rupture. A chain of paramagnetic particles subject to both a shear flow and a constant applied magnetic field is the case we are interested in here. This problem has been analyzed previously in [88] using simple drag-based chain models. In the simplest standard chain model, the interparticle magnetic forces are provided by fixed point dipoles which gives the force between two beads with their line of centers at an angle ϕ_n to the applied field as

$$\mathbf{F}^n_{mag} = b\left[(3\cos^2\phi_n - 1)\hat{\mathbf{r}}_n + \sin(2\phi_n)\hat{\boldsymbol{\phi}}_n\right] \tag{4.6}$$

where $\hat{\mathbf{r}}_n = \cos\phi_n\hat{\mathbf{x}} + \sin\phi_n\hat{\mathbf{y}}$ is the unit vector tangent to the chain axis, $\hat{\boldsymbol{\phi}}_n = \sin\phi_n\hat{\mathbf{x}} - \cos\phi_n\hat{\mathbf{y}}$ is the unit vector perpendicular to the chain axis and

$$b = \frac{3\pi a^2\eta\gamma}{8Ma_{shear}}. \tag{4.7}$$

The hydrodynamic force on bead n centered at Y_n as a result of the shear flow (4.3) is provided by the Stokes drag approximation, $\mathbf{F}^n_{drag} = 6\pi\eta a\gamma(\mathbf{Y}_n\cdot\hat{\mathbf{y}})\hat{\mathbf{x}}$. If we consider a chain of N beads, the total hydrodynamic force on bead n is

$$\mathbf{F}^n_{hydro} = \sum_{k=n+1}^{N} \mathbf{F}^k_{drag}. \tag{4.8}$$

If we are interested in ascertaining the maximum angle and maximum number of beads in the chain for a given Ma_{shear} we need only to consider this balance in the center of the chain where the total hydrodynamic force will be maximum. The force balance between the tangential and radial components of the hydrodynamic and magnetic forces at the chain center are

$$12\pi a^2 \eta\gamma \cos^2\phi \sum_{k=1}^{N/2} k = \frac{3\pi a^2 \eta\gamma}{8Ma_{shear}} \sin(2\phi) \tag{4.9}$$

$$12\pi a^2 \eta\gamma \cos\phi \sin\phi \sum_{k=1}^{N/2} k = \frac{3\pi a^2 \eta\gamma}{8Ma_{shear}} (3\cos^2\phi - 1). \tag{4.10}$$

Using the relationship $\sum_{k=1}^{N/2} k = N(N+1/2)/8$, the force balance yields

$$2Ma_{shear} N(N+1/2) = \tan\phi \tag{4.11}$$

$$4Ma_{shear} N(N+1/2) = \frac{3\cos^2\phi - 1}{\cos\phi \sin\phi} \tag{4.12}$$

giving the maximum angle and number of beads

$$\tan\theta = \sqrt{2/3} \tag{4.13}$$

$$N = -\frac{1}{4} + \sqrt{\frac{1}{16} + \frac{\sqrt{2/3}}{2Ma_{shear}}}. \tag{4.14}$$

The chain model ignores both the hydrodynamic interactions between the beads and higher-order corrections to the magnetic interactions. To include these effects, we perform simulations of a chain of N paramagnetic beads with magnetic susceptibility $\chi = 1$ ($\chi_{eff} = 0.75$) in the shear flow (4.3) with the applied field $\mathbf{H} = H_0\hat{\mathbf{y}}$. The simulations are conducted employing the techniques described in the previous chapters with the hydrodynamic interactions provided by FCM, the magnetic interactions are provided by the mutual dipole method augmented by the higher-order multipole inclusion method. In the barrier force, $R_{ref} = 2.2a$ and $F_{ref} = 1.05F_{con}$. Initially, the chain axis is aligned with the applied

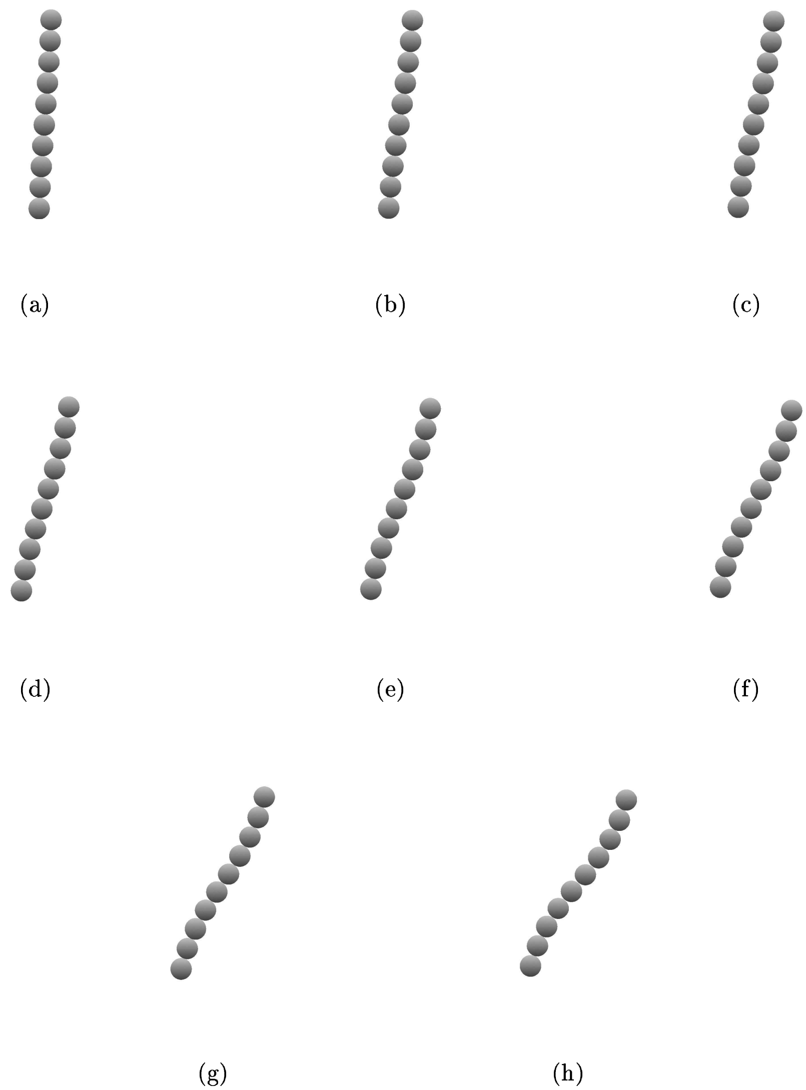

Figure 4.8: Equilibrium shape of a chain of $N = 10$ beads in a shear flow with different values of Ma_{shear}. The applied magnetic field is in the vertical direction. (a) $Ma_{shear} = 0.0009$, (b) $Ma_{shear} = 0.0018$, (c) $Ma_{shear} = 0.0027$, (d) $Ma_{shear} = 0.0036$, (e) $Ma_{shear} = 0.0045$, (f) $Ma_{shear} = 0.0054$, (g) $Ma_{shear} = 0.0063$, (e) $Ma_{shear} = 0.0072$

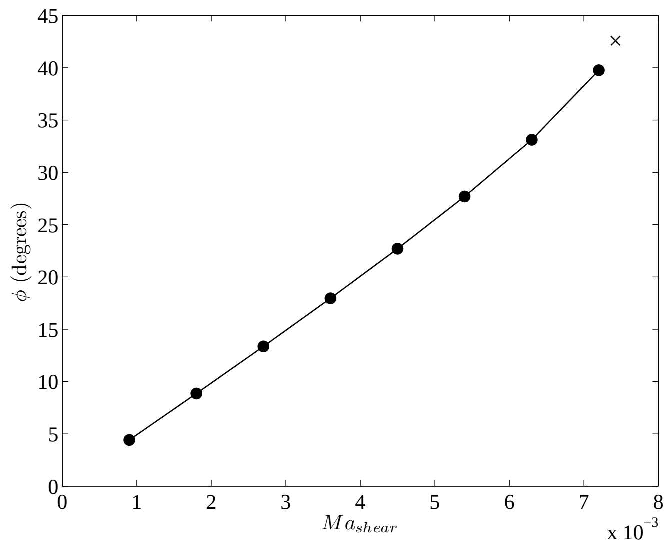

Figure 4.9: The angle ϕ between the chain axis in the center of the chain and the applied field over a range of Ma_{shear} for a chain of $N = 10$ beads.

field and as time evolves the shear flow rotates, deforms and, if strong enough, breaks the chain. Figure 4.8 shows the equilibrium shape of a chain of $N = 10$ beads over a range of Mason numbers below the critical value ($Ma_{shear}^{crit} = 0.007425$). The shear flow exerts a torque on the chain which creates an angle between the chain axis and the applied field. This effect is exhibited at all Ma_{shear} (Figure 4.8). This angle ϕ measured at the center of the chain is shown as a function of Mason number in Figure 4.9. At low Ma_{shear}, ϕ grows linearly with the shear rate and at higher Ma_{shear} grows steeply to the point at which the chain fractures. In addition to the growth of ϕ, we see that at high shear rates the chain will deviate from its linear shape into an S-shape (Figures 4.8(e)-4.8(h)).

We perform a series of simulations to determine the maximum Mason number Ma_{shear}^{crit} that a chain of N beads will not break. These simulations are performed for chains containing up to $N = 15$ beads. The number of beads N is plotted as a function of the maximum Mason number given by the full simulations in Figures 4.10(b) and 4.10(a). The maximum number of beads in a chain decreases with the Mason number since the hydrodynamic force on the chain increases with the chain length. As compared to the chain model, (4.14) and the dashed line in Figure 4.10(b), the simulations predict a greater chain length for $Ma_{shear} < 0.04$. In addition, at low Ma_{shear}, the simulations yield a decay in chain length faster than that given by the chain model ($N \sim Ma_{shear}^{-1/2}$).

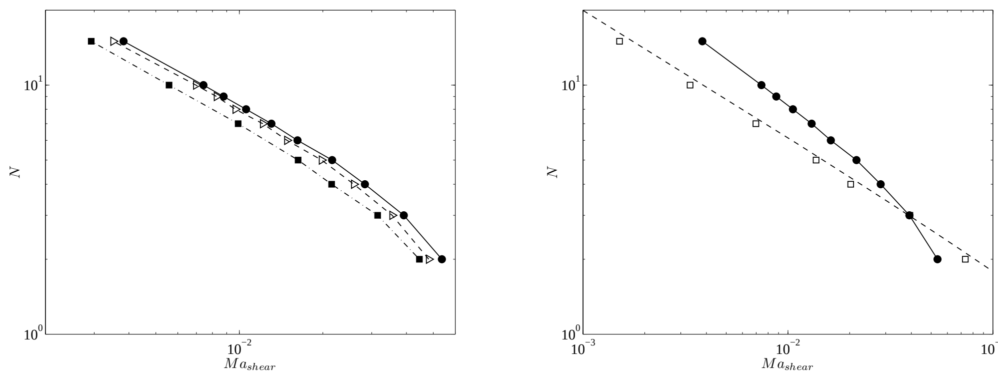

(a) (b)

Figure 4.10: (a) Maximum number of beads N in a chain as a function of Ma_{shear} as given by FCM with the fixed dipole model (dash-dotted line with square markers), the mutual dipole model (dashed line with open triangular markers) and the full magnetic model (solid line with circular markers). (b) Maximum number of beads N in a chain as a function of Ma_{shear} as given by FCM with the full magnetic model (solid line with circular markers), Stokes drag law with fixed dipole model (open square markers) and the chain model (4.14) (dashed line).

To understand the reason behind the difference between the chain model and the simulations results, we perform additional simulations where we first employ the fixed and mutual dipole models for the magnetic interactions between the beads but retain a complete description of the hydrodynamic interactions. These results are shown in Figure 4.10(a). We see that the inclusion of the higher multipoles shifts the critical Mason number to higher values, but does change the scaling of N with Ma_{shear}. In a second set of simulations, in addition to using only point dipoles to resolve the magnetic interactions, we ignore the hydrodynamic interactions between the beads. We obtain results (open squares in Figure 4.10(b)) that correspond well with the values predicted by the chain model. Therefore, employing a Stokes drag approximation introduces an underestimation of the maximum chain length and fails to recover the proper scaling of this value with the Mason number.

The hydrodynamic effects along the length of the chain may be included into the chain model using a slender body approximation which give drag coefficients per unit length as

$$\zeta_{||} = \frac{2\pi\eta}{\log(L/2a) - 1/2} \tag{4.15}$$

$$\zeta_{\perp} = \frac{4\pi\eta}{\log(L/2a) + 1/2}. \tag{4.16}$$

Therefore, the drag on a bead in the $\hat{\mathbf{r}}$-direction is $2a\zeta_{||}$ and $2a\zeta_{\perp}$ is that in the $\hat{\boldsymbol{\phi}}$-direction. These modifications in the drag yield the revised chain model equations

$$4a^2\zeta_{\perp}\gamma\cos^2\phi\sum_{k=1}^{N/2} k = \frac{3\pi a^2\eta\gamma}{8Ma_{shear}}\sin(2\phi) \tag{4.17}$$

$$4a^2\zeta_{||}\cos\phi\sin\phi\sum_{k=1}^{N/2} k = \frac{3\pi a^2\eta\gamma}{8Ma_{shear}}(3\cos^2\phi - 1) \tag{4.18}$$

which with $L = 2aN$ give

$$\frac{8}{3}\frac{Ma_{shear}N(N+1/2)}{\log N + 1/2} = \tan\phi \tag{4.19}$$

$$\frac{8}{3}\frac{Ma_{shear}N(N+1/2)}{\log N - 1/2} = \frac{3\cos^2\phi - 1}{\cos\phi\sin\phi}. \tag{4.20}$$

For long chains $\log N + 1/2 \approx \log N - 1/2$, and $\phi \approx 45°$ and

$$\frac{N(N+1/2)}{\log N + 1/2} \approx \frac{3}{8Ma_{shear}}. \tag{4.21}$$

In Figure 4.11 we plot the results from the full simulations and the values given by (4.21). Although the values still differ by a factor of ≈ 1.4, the agreement is much better and the scaling is well reproduced. A similar modification to the chain model has been considered [88], but the logarithmic terms in the denominators of the drag coefficients that are essential to reproduce the correct scaling were ignored.

4.3.2 Chain subject to a rotating field

Just as we did in analyzing the behavior of a chain in a shear flow, we first discuss the equilibrium of a chain of paramagnetic particles in the rotating field

$$\mathbf{H} = H_0(\sin(\omega t), \cos(\omega t), 0) \tag{4.22}$$

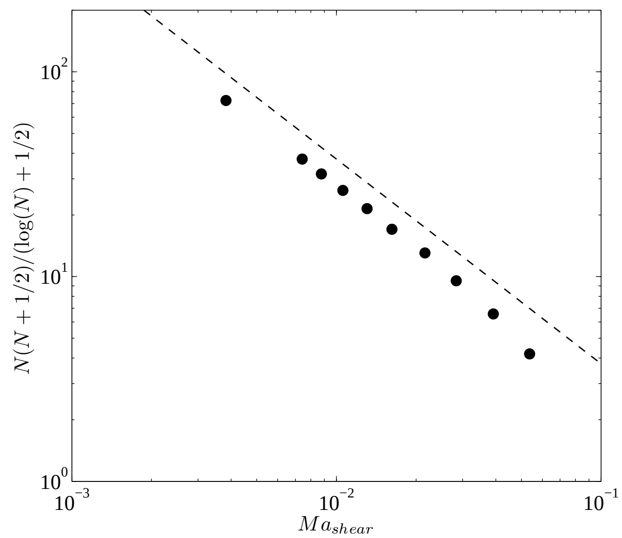

Figure 4.11: Maximum number of beads N in a chain as a function of Ma_{shear} as given by FCM with the full magnetic model (solid line with circular markers) and the corrected chain model (4.21) (dashed line).

using the chain model as presented in [94]. We may rewrite the strength of the interparticle dipole force b in terms of Ma_{rot} as

$$b = \frac{12\pi a^2 \eta\omega}{Ma_{rot}} \tag{4.23}$$

and adopt a reference frame fixed with respect to the rotating field. Taking the Stokes drag approximation, the drag force on bead n is given by

$$\mathbf{F}^n_{drag} = 6\pi a\eta\omega r_n \hat{\boldsymbol{\phi}}. \tag{4.24}$$

where $r_n = \sqrt{\mathbf{Y}_n \cdot \mathbf{Y}_n}$ and $\hat{\boldsymbol{\phi}}$ is the unit vector in the ϕ-direction in a cylindrical coordinate system centered at the origin. For a linear chain, this force will be in the direction perpendicular to the chain axis. Unlike the case of the shear flow, we need only to consider the force balance at the chain center in the direction perpendicular to the chain axis

$$12\pi a^2\eta\omega \sum_{k=1}^{N/2} k \quad = \quad \frac{12\pi a^2\eta\omega}{Ma_{rot}} \sin(2\phi) \tag{4.25}$$

which becomes

$$\frac{Ma_{rot}N}{8}\left(N+\frac{1}{2}\right) \quad = \quad \sin(2\phi). \tag{4.26}$$

Since there is no hydrodynamic force in the direction of the chain axis, the chain will break once the interparticle magnetic forces in this direction become zero. This occurs when

$$3\cos^2\phi - 1 = 0 \tag{4.27}$$

or when $\cos\phi = \sqrt{1/3}$ ($\phi \approx 54.7°$). While this is the angle at which the chain will break, the interparticle magnetic force perpendicular to the chain axis is maximum when $\phi = 45°$. Therefore if a chain at $\phi = 45°$ to the applied field is not able to balance the hydrodynamic forces, it will inevitably rotate to the critical value of $\phi \approx 54.7°$ and break [94]. Based on this, we take the value of $\phi = 45°$ to calculate the maximum number of beads in the chain giving the maximum number of beads as

$$N \quad = \quad -\frac{1}{4} + \sqrt{\frac{1}{16} + \frac{8}{Ma_{rot}}}. \tag{4.28}$$

From the particle-based simulations, we see that a chain subject to a rotating field will behave in a manner similar to a chain in a shear flow. At low values of Ma_{rot}, the chain will remain linear but the viscous stresses will establish an angle between the chain axis and the applied field. At higher values of Ma_{rot}, but still below the critical value, the angle between the chain axis and the applied field will increase and the chain will deviate from its linear shape and develop into a curved S-shape. The different equilibrium shapes exhibited by a chain of $N = 10$ beads in this regime are shown in Figure 4.12. The angle between the applied field and the chain axis as a function of Ma_{rot} is shown in Figure 4.13.

As with the shear flow, we perform particle-based simulations of the chain using a variety of magnetic and hydrodynamic models to obtain the critical Mason number for chains of up to bead number $N = 15$. As before, modifying the magnetic interactions shifted the maximum allowable number of beads to lower values, but preserved the scaling of N with Ma_{rot} (Figure 4.14(a)). When the hydrodynamic interactions between the particles were ignored, the scaling changed and the predictions of the linear chain model (4.28) were reproduced (Figure 4.14(b)). We again incorporate the hydrodynamic effects into the chain

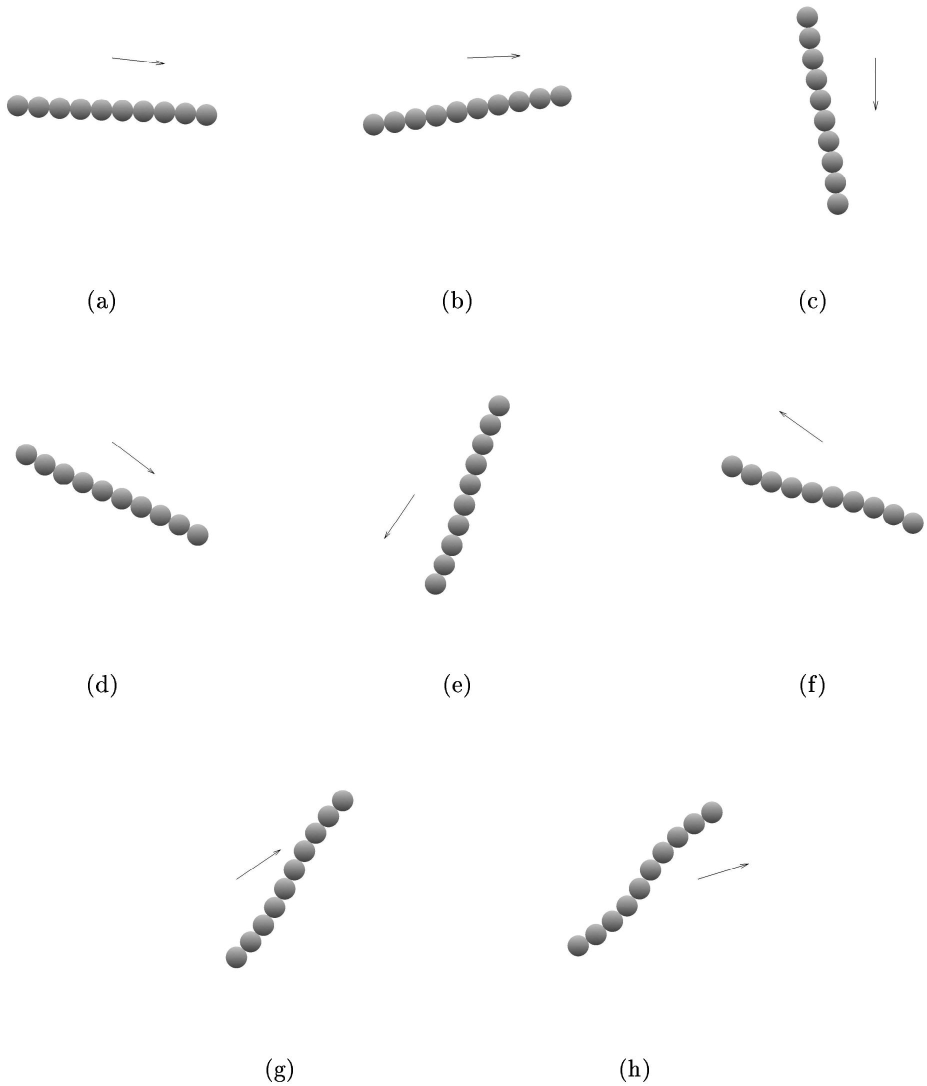

Figure 4.12: Equilibrium chain configurations and orientations for a chain of $N = 10$ beads relative to a clockwise rotating field with different values of Ma_{rot}. The direction of the applied magnetic field in each image is shown by the arrow. (a) $Ma_{rot} = 0.03$, (b) $Ma_{rot} = 0.05$, (c) $Ma_{rot} = 0.07$, (d) $Ma_{rot} = 0.09$, (e) $Ma_{rot} = 0.11$, (f) $Ma_{rot} = 0.13$, (g) $Ma_{rot} = 0.15$, (e) $Ma_{rot} = 0.17$

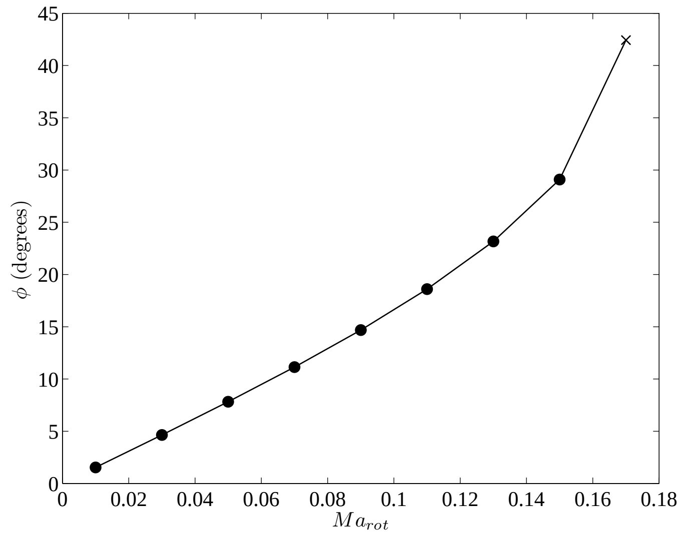

Figure 4.13: The angle ϕ between the chain axis in the center of the chain and the applied field over a range of Ma_{rot} for a chain of $N = 10$ beads.

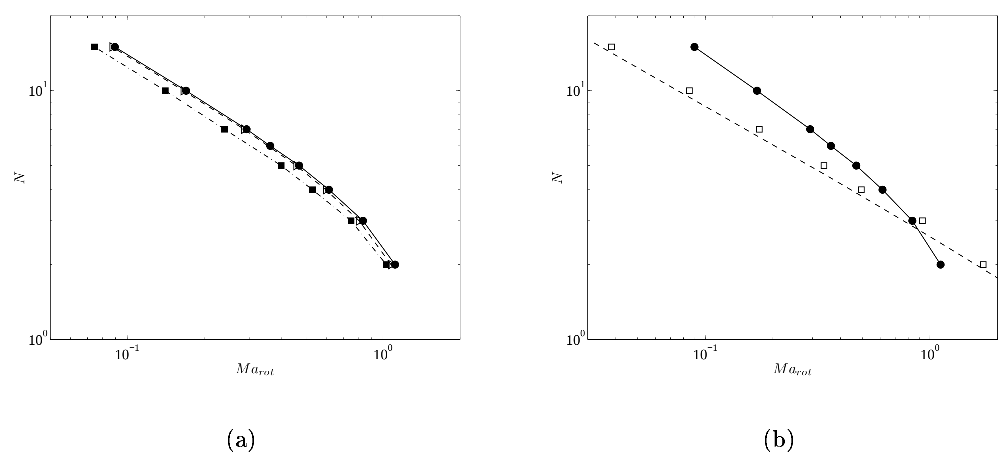

Figure 4.14: (a) Maximum number of beads N in a chain as a function of Ma_{rot} as given by FCM with the fixed dipole model (dash-dotted line with square markers), the mutual dipole model (dashed line with open triangular markers) and the full magnetic model (solid line with circular markers). (b) Maximum number of beads N in a chain as a function of Ma_{rot} as given by FCM with the full magnetic model (solid line with circular markers), Stokes drag law with fixed dipole model (open square markers) and the chain model (4.28) (dashed line).

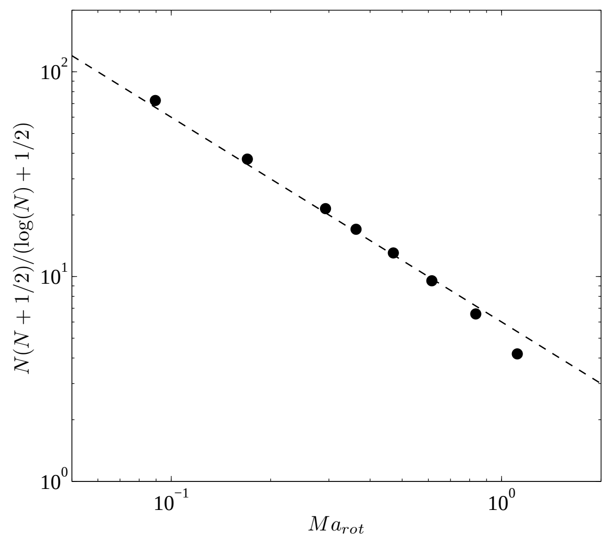

Figure 4.15: Maximum number of beads N in a chain as a function of Ma_{rot} as given by FCM with the full magnetic model (solid line with circular markers) and the corrected chain model (4.30) (dashed line).

model by using a slender body approximation for the drag per unit length perpendicular to the chain axis $\zeta_\perp$. With this modification, the resulting perpendicular force balance is

$$4a^2\zeta_\perp\omega\sum_{k=1}^{N/2}k = \frac{12\pi a^2\eta\omega}{Ma_{rot}}\sin(2\phi) \tag{4.29}$$

which becomes with $\phi = 45°$

$$\frac{N(N+1/2)}{\log N + 1/2} = \frac{6}{Ma_{rot}}. \tag{4.30}$$

Figure 4.15 shows (4.30) compared with the results from the full simulations. Here, excellent agreement is found indicating the importance of the hydrodynamic interactions to obtain the correct predictions of chain fracture.

4.4 Suspensions of paramagnetic particles in rotating fields

A recent series of experimental studies [93, 115] examined the evolution of an initially homogeneous suspension of paramagnetic particles subject to an applied rotating field. They observed that for low values of Ma_{rot}, the particles aggregate to form linear chains that rotate with the frequency of the applied field. The average length of the chains will decrease with Ma_{rot} until a critical value is reached. This critical value corresponds with the value of Ma_{rot} at which a doublet will first exhibit oscillations in the separation distance. While the chain structure is no longer stable when $Ma_{rot} > Ma_{rot}^{crit}$, aggregation still occurs and instead one observes the formation of small planar structures. To simulate this behavior, we consider an initially homogeneous distribution of paramagnetic particles in a three-dimensional domain with periodic boundary conditions in each direction. The mutual finite-dipole model of §3.2.2 supplemented by the multipole inclusion model provides the magnetic interactions while FCM resolves the hydrodynamic interactions. The collision barrier with $F_{ref} = 1.02F_{con}$ and $R_{ref} = 2.2a$ provides the solid body contact. At each timestep, the Stokes equations and the equations for the magnetic field are solved using a Fourier collocation method where 384^3 points are used in the magnetic field calculation and 256^3 are used to solve the Stokes equations. The simulations are performed using a parallel code run on 32 processors and the Adams-Bashforth second order scheme is used to update the particle positions. The simulation contains $N = 1320$ particles which corresponds to a volume fraction of $c = 0.007$.

We consider two values of Ma_{rot}, $Ma_{rot} = 0.2$ which is below the critical value and $Ma_{rot} = 2.0$ which is above the critical value. As in the experiments, we see that if Ma_{rot} is below the critical value, chains do form and rotate with the applied field (Figure 4.16). We also observe the deformation and fracture of the aggregates as they reach a critical length. Based on the results of the previous sections, the maximum chain length for this case is $N \approx 10$. Above the critical Mason number, we observe a variety of stable two dimensional structures (Figure 4.17) identical to those seen in the experiments. When compared to the $Ma_{rot} = 0.2$ case, fewer particles were found to aggregate. The clusters formed up to cluster size $n_c = 7.0$ are shown in Figure 4.18. Unlike linear aggregation, we see that above $n_c > 5$, two dimensional clusters of a certain size can have different shapes. The behavior of these types of aggregates in shear flows has been investigated experimentally in [122].

To examine the change in shape and number of clusters formed above Ma_{rot}^{crit}, Melle *et al.* [93] conducted dichroism experiments where they measured the difference Δn_0 in light extinction parallel and perpendicular to the axis of the clusters. The found that below the critical Mason number, Δn_0 remains constant since the chain structure is stable and comparable numbers of particles can aggregate. Above the critical value where fewer, planar structures form, $\Delta n_0 \sim Ma^{-1}$ (Figure 4.19). To compare with these results, we determine

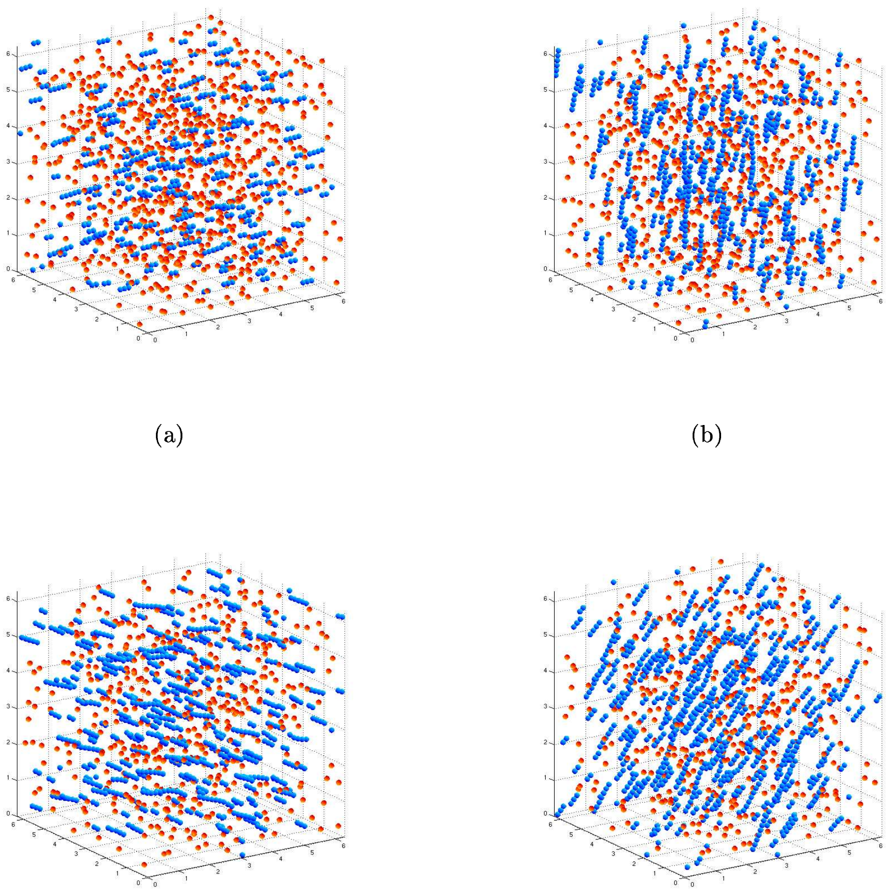

(a) (b)

(c) (d)

Figure 4.16: Aggregation of paramagnetic particles subject to a rotating magnetic field with $Ma_{rot} = 0.2$: (a) $t/T_{field} = 0.764$, (b) $t/T_{field} = 1.560$, (c) $t/T_{field} = 2.356$ and (d) $t/T_{field} = 3.151$ with T_{field} being the period of the applied field. In these images, the bead is colored blue if it is a member of an aggregate and red it remains unattached.

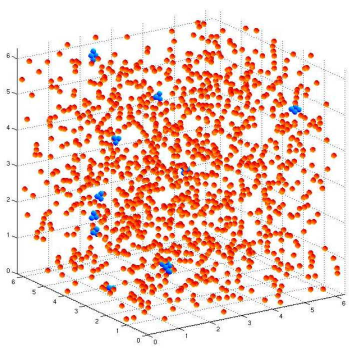

(a)

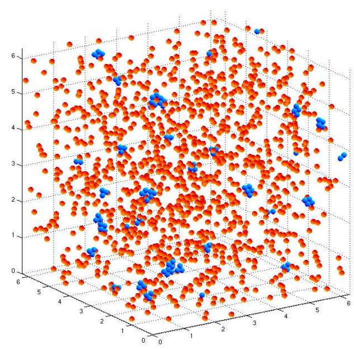

(b)

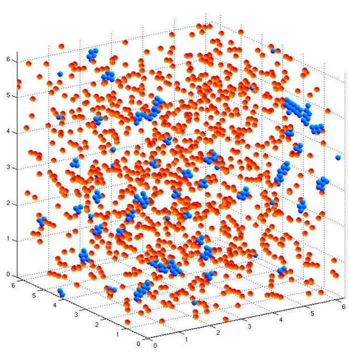

(c)

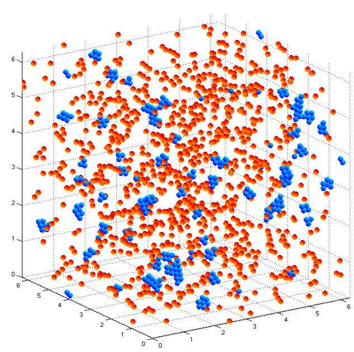

(d)

Figure 4.17: Aggregation of paramagnetic particles subject to a rotating magnetic field with $Ma_{rot} = 2.0$: (a) $t/T_{field} = 7.639$, (b) $t/T_{field} = 15.597$, (c) $t/T_{field} = 23.555$ and (d) $t/T_{field} = 31.513$ with T_{field} being the period of the applied field. In these images, the bead is colored blue if it is a member of an aggregate and red it remains unattached.

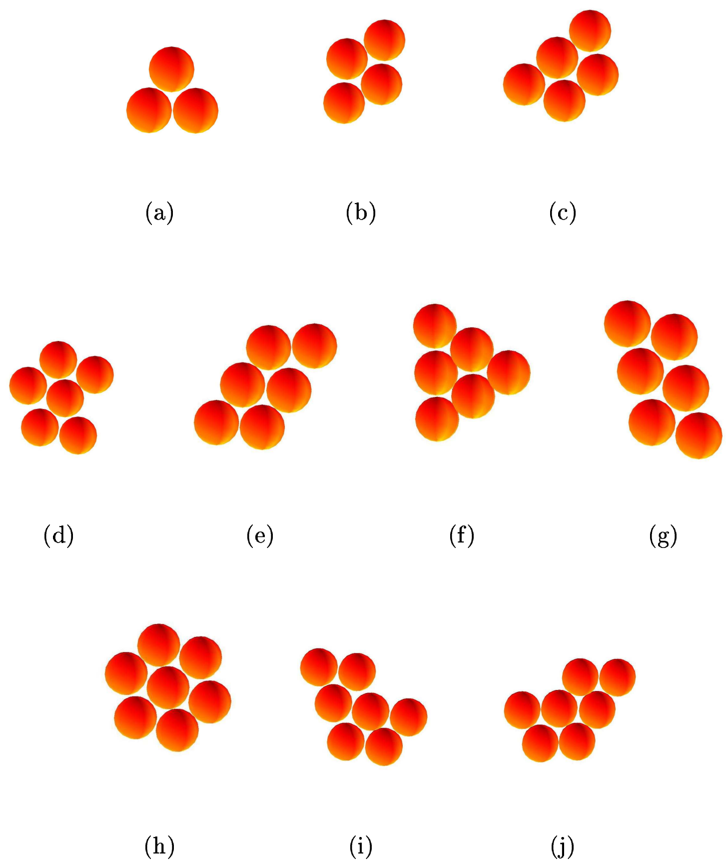

Figure 4.18: Stable clusters formed in a suspension of paramagnetic beads subject to a rotating magnetic field with $Ma_{rot} = 2.0$: (a) $n_c = 3$, (b) $n_c = 4$, (c) $n_c = 5$, (d)–(g) $n_c = 6$ and (h)–(j) $n_c = 7$.

the value [93]

$$\Delta n_0^{sim} = \left\langle \frac{N_a}{N} \sum_{n=1}^{N_c} \frac{\sqrt{I_n^{max}} - \sqrt{I_n^{min}}}{\sqrt{I_n^{max}} + \sqrt{I_n^{min}}} \right\rangle \tag{4.31}$$

were N_a is the number of particles that have aggregated, N_c is the total number of clusters and I_n^{max} and I_n^{min} are the maximum and minimum eigenvalue of the tensor

$$\mathcal{I}_{ij}^n = \sum_{k=1}^{n_c} \frac{(\mathbf{Y}_k - \mathbf{Y}_n^{cm})_i (\mathbf{Y}_k - \mathbf{Y}_n^{cm})_j}{a^2} \tag{4.32}$$

for an individual cluster n of n_c particles with $\mathbf{Y}_n^{cm} = \sum_{k=1}^{n_c} \mathbf{Y}_k / n_c$. In 4.31, the term N_a/N accounts for the number of particles aggregated and $(\sqrt{I_n^{max}} - \sqrt{I_n^{min}})/(\sqrt{I_n^{max}} + \sqrt{I_n^{min}})$ accounts for the cluster shape, since for a chain the value of this ratio is 1 whereas for a circle it is 0. As these experimental measurements were performed once the aggregation has stopped, we must run the simulations until an equilibrium is reached. We, therefore, perform three small simulations ($N = 50$) at $c = 0.007$ for each value of $Ma_{rot} = 2$, 4, 6 and 8 considered. The values of Δn_0^{sim} for each Ma_{rot} are averaged over the three simulations. These averaged values are shown as the blue circles in Figure 4.19 and even with the small number of particles considered, agreement with between the simulations and experiments is found.

4.5 Conclusions

In this chapter, we examined the dynamics of small and large ensembles of paramagnetic particles in situations where an external flow is present, or the applied field is time dependent. We first looked at the oscillatory dynamics exhibited by a pair of beads in a rotating field and the effects of the collision barrier on this behavior. We demonstrated that including the collision barrier captures physically relevant effects such as surface forces and particle roughness. We determined the decrease in Ma_{rot}^{crit} and the increase in the magnitude of the oscillations as a result of increasing R_{ref}. The behavior of a chain of particles in a shear flow and in a rotating field were then considered. In each case, the hydrodynamic interactions along the length of the chain are needed to reproduce the correct torque on the chain. Not including these effects will yield the incorrect scaling of N with Ma_{shear} or Ma_{rot} and underestimate the maximum chain length that can exist at a given Ma_{shear} or Ma_{rot}. The formation of aggregates in suspensions of paramagnetic particles subject to

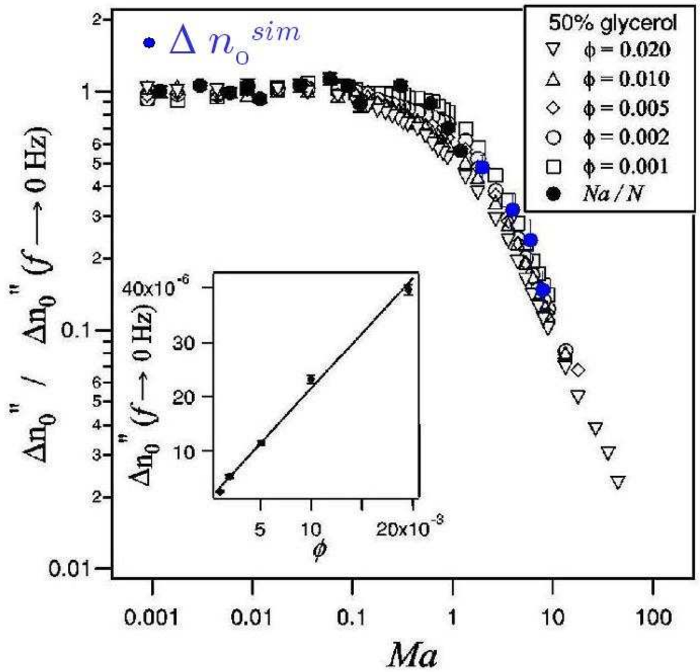

Figure 4.19: Simulation results (blue circles) as compared with the dichroism data from [93].

rotating fields, and as in the experiments [93, 115], we found that below Ma_{rot}^{crit} chains of particles formed that rotated with the applied field, where as above Ma_{rot}^{crit} planar aggregates were observed. Determining the number and shape of these planar clusters allowed for a favorable comparison with the results from dichroism experiments [93].

Chapter 5

The artificial micro-swimmer and models for describing the elastic coupling between particles in magnetic filaments

5.1 Introduction

In Chapter 2, we discussed how both fluid and particle inertia can be ignored when considering the motion of small objects in a viscous fluid and as a result, low Reynolds number flows are kinematically reversible. To generate a net translation a micro-swimmer's cyclic strategy must therefore be one that is non-reciprocal [103]. Many of the single cell micro-organisms that propel themselves in this environment utilize a long flagellum tail connected to the cell body. Purcell categorizes the majority of these flagella or one-armed swimmers as either those that use a "flexible oar" strategy, or a"corkscrew" strategy. The "flexible oar" swimmers, such as spermatozoa, swim by propagating bending waves down the length of their flagellum tail, while swimmers applying the "corkscrew" strategy, such as *E. coli* bacteria, rotate their helically shaped flagellum or flagellar bundles which afford the conversion of rotational to translational motion.

Beginning with G. I. Taylor's study of a swimming sheet [113] and subsequent analysis concerning motions associated with waves generated along a cylindrical tail [114], the development of model systems has been essential to understanding the fundamental principles surrounding the swimming of micro-organisms. Recent investigations that keep with this approach include studies of Purcell's three link swimmer [103, 5] and the measurements of the lateral force generated by filament when one end is displaced transversely in an oscillatory manner [116, 117, 121, 76]. A promising candidate for an additional model system is the artificial magnetic micro-swimmer produced by Dreyfus *et al.* [33]. While originally introduced to experimentally examine the prediction of an optimal frequency of the propulsive force for a "flexible oar" swimmer [116, 72], the artificial swimmer may serve as a physical model to explore other aspects of low Reynolds number swimming such as alternative propulsion strategies and swimmer-swimmer interactions.

In this chapter, we first discuss the findings of the artificial swimmer experiments [33]. We then introduce an elastic coupling scheme to represent the elastic properties of a magnetic filament and employ this model to examine the deformations of a microfilament settling in a viscous fluid. Simulations of the artificial micro-swimmer are then presented and the resulting swimming speeds are compared with the experiments and other simulations [44].

5.2 Summary of the Micro-swimmer Experiments

The artificial swimmer consists of a flexible magnetic flagellum-like tail connected to a human red blood cell, see Figure 5.1 [33]. The magnetic filament is comprised of monodisperse paramagnetic beads of radius $a = 0.5\mu m$ that are manufactured for the purpose of biochemical separation. The surfaces of these beads are treated with the active binding agent streptavidin that readily bonds with the chemical biotin. To form the magnetic filament, the streptavidin coated beads are first allowed to aggregate under the influence of a uniform magnetic field, forming chains aligned with the applied field ([102]). A flexible biotin-ended DNA molecules are then introduced and irreversibly link the beads together. The resulting flexible micro-filament can then be manipulated by adjusting external applied magnetic field. The elastic properties of such filaments have been studied by [48] and [9] and used as a key component of a mixing device by [10]. The red blood cell provides a necessary component as the magnetic filament, if homogeneous in elastic and magnetic properties, lacks the asymmetry necessary to produce a net translate. The increase in hydrodynamic drag at the tethered end allows for bending waves to propagate from the tip of the tail

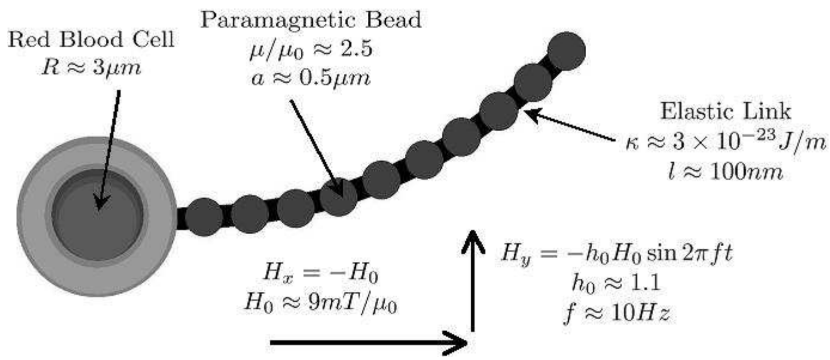

Figure 5.1: Sketch of the artificial micro-swimmer.

toward the red blood cell which results in tail first swimming.

In [33], the motion of the swimmer driven by an oscillating magnetic field of the form

$$\mathbf{H} = -H_0(1, h_0 \cos \omega t, 0). \tag{5.1}$$

where a typical frequency of the applied field is $\omega = 62.8\text{rad}/s$. With the viscosity of the surrounding fluid, η, being that of water, the Reynolds number corresponding to the motion is $Re = \rho \omega a^2/\eta \approx 10^{-5}$ [107]. Further, they identified three dimensionless parameters that govern the dynamics of the swimmer. The first is h_0; the ratio of the transverse field to the constant field. The second parameter is is the *sperm number*, Sp, given by

$$Sp = \left(\frac{4\pi\eta\omega L^4}{K_b}\right)^{1/4} \tag{5.2}$$

where L is the length of the tail and K_b is the effective bending modulus of the filament. The sperm number gives the ratio of the viscous to elastic forces and provides the ratio of the length of the filament to the elastohydrodynamic length $l_{EH} = (K_b/4\pi\eta\omega)^{1/4}$ [116] over which bending will occur. The third parameter is the *magnetoelastic number*, Mn

$$Mn = \frac{\pi\mu_0(\chi_{eff} a H_0 L)^2}{6K_b(1 - \chi_{eff}/6)(1 + \chi_{eff}/12)} \tag{5.3}$$

which provides a measure of the strength of the magnetic forces relative to the elastic forces. The scaled swimming speed of the device $U = V/(L\omega)$ was then measured over a range of

Sp with the parameters h_0 and Mn fixed. Specifically, the experiments were conducted over the range $1 \leq Sp \leq 6.3$ for $Mn = 4.5, 11.7$ and 16 with $h_0 = 1.07 - 1.16$. They found that the scaled swimming speed initially increases with Sp. The scaled swimming speed then attains a peak value after which it decays monotonically with Sp.

Our goal is to provide an effective simulation of this device based on the methods already developed to study interacting paramagnetic particles. The challenge here is to incorporate the elastic properties of the DNA molecules linking the beads together.

5.3 Modeling the Elastic-coupling

The dynamics of magnetic filaments have been addressed using two different approaches. The first approach ignores the discrete nature of the filament and treats it as a continuous elastic rod with a bending modulus K_b. This type of modeling has been instrumental in the understanding of the dynamics of elastic filaments in a viscous fluid [116, 118, 6] and studies of low Reynolds number propulsion [116, 76, 5]. The hydrodynamic forces are incorporated using simple drag laws based on slender body theory where the drag coefficient per unit length is that for a line of Stokeslets translating through fluid [65]. To incorporate the effects of the applied field, magnetic torques along the length of the filament are considered. In the context of magnetic filaments, elastic rod models have been the basis of a number of studies including the discussion by [33] of their experiments with the artificial swimmer, elastic defect driven swimming in [107], and the dynamics of magnetic filaments in rotating fields and shear flows considered in [20, 21, 19].

Using an alternative approach, Gauger *et al.* [44] employ a particle-based description of the magnetic filament tail in their simulations of the artificial swimmer. Here, the N beads comprising the tail interacted magnetically through fixed dipole interactions and experienced fluid forces based on the Rotne-Prager mobility. Additionally, the resistance to bending was represented by a wormlike chain, see [73, 83], that reproduces the bending of a continuous elastic rod in the limit $N \to \infty$.

While these models have been instrumental in the understanding of the behavior of microfilaments in viscous fluids, simplifications of the dynamics introduced by both models limit their ability to describe accurately the dynamics of magnetic filaments. In the case of the continuous elastic rod models, the hydrodynamic forces along the length of the filament

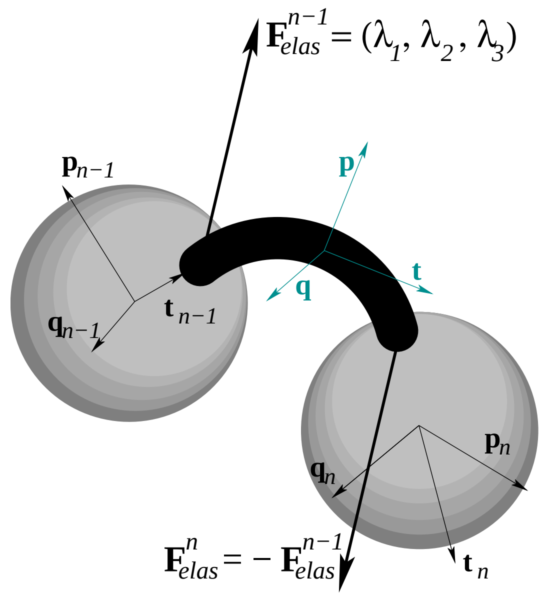

Figure 5.2: Sketch of two neighboring particles of the filament. The link exerts a force $\mathbf{F}_{elas}^{n-1}$ on bead $n-1$ and an equal and opposite force on bead n. The shape of the link is characterized by the coordinate system $(\mathbf{t}, \mathbf{p}, \mathbf{q})$ that varies along the length and attains values $(\mathbf{t}_{n-1}, \mathbf{p}_{n-1}, \mathbf{q}_{n-1})$ at the left attachment point, and $(\mathbf{t}_n, \mathbf{p}_n, \mathbf{q}_n)$ at the opposite end.

are treated using a drag model that is only valid in the rigid limit where the filament remains straight. In addition, these drag based models cannot recover the Jeffrey orbit behavior of an axisymmetric body in a shear flow [6] or reproduce the deformation exhibited by a settling filament [73]. While the particle based approach adopted by [44] allows for hydrodynamic interactions along the length of the filament, it comes at the expense of the resolution of the elastic properties of filament that now artificially depend on the number of beads in the filament N [44], [83].

To move past these limitations, we introduce an elastic coupling model specifically designed for magnetic filaments. We employ a particle based model where the hydrodynamic interactions are provided by FCM §2.2.1 and magnetic dipoles §3.1.2 are used to reproduce the interparticle magnetic interactions. The elastic coupling between the particles is achieved by representing each chemical link as an inextensible elastic rod. By treating each link separately, we have removed the influence of the number of particle on the resolution of the elastic forces.

The chemically formed links produce elastic forces and bending moments that act to return a bent filament to its original linear configuration. This effect is captured by treating each link as an inextensible, but flexible rod of length l. In such a description, the force and moment balance [74] for a link are

$$\frac{d\mathbf{N}}{ds} + \mathbf{K} = \mathbf{0} \tag{5.4}$$

$$\frac{d\mathbf{M}}{ds} + \mathbf{t} \times \mathbf{N} + \boldsymbol{\tau} = \mathbf{0}. \tag{5.5}$$

$\mathbf{N}(s)$ is the resultant internal stress on a cross-section and $\mathbf{M}(s)$ is the moment of the internal stresses on the cross-section. Both $\mathbf{N}(s)$ and $\mathbf{M}(s)$ vary with arclength $0 \leq s \leq l$ and balance the applied forces per unit length $\mathbf{K}$ and torques per unit length $\boldsymbol{\tau}$. In (5.5), $\mathbf{t}$ denotes the vector tangent to the centerline of the link. The moment $\mathbf{M}$ is related to the deformation of the link through the constitutive law

$$\mathbf{M} = \kappa \mathbf{t} \times \frac{d\mathbf{t}}{ds} + C\mathbf{t}\frac{d\Psi}{ds} \tag{5.6}$$

where κ is the bending modulus, C the twist modulus, and Ψ the twist angle.

Consider the link connecting beads $n-1$ and n centered at $\mathbf{Y}_{n-1}$ and $\mathbf{Y}_n$ respectively. Each bead has local body axes $(\mathbf{t}_{n-1}, \mathbf{p}_{n-1}, \mathbf{q}_{n-1})$ and $(\mathbf{t}_n, \mathbf{p}_n, \mathbf{q}_n)$. The link joining these beads begins $(s = 0)$ at the point $\mathbf{Y}_{n-1} + a_{n-1}\mathbf{t}_{n-1}$ on the surface of bead $n-1$ and ends $(s = l)$ at $\mathbf{Y}_n - a_n\mathbf{t}_n$ on the surface of bead n as shown in Figure 5.2. At the points of contact, the centerline of link is taken to be perpendicular to the surfaces of the spheres corresponding to the clamped-end boundary conditions $\mathbf{t} = \mathbf{t}_{n-1}$ at $s = 0$ and $\mathbf{t} = \mathbf{t}_n$ at $s = l$. The link is inextensible and there is the constraint

$$(\mathbf{Y}_n - \mathbf{Y}_{n-1}) - a_n\mathbf{t}_n - a_{n-1}\mathbf{t}_{n-1} = \int_0^l \mathbf{t}\, ds \tag{5.7}$$

on the components of the vector pointing from the attachment site on bead $n-1$ to that on bead n. Associated with this constraint are the force on bead $n-1$, $\mathbf{F}^{n-1}_{elas} = \lambda_1\mathbf{t}_{n-1} + \lambda_2\mathbf{p}_{n-1} + \lambda_3\mathbf{q}_{n-1}$ and the equal and opposite force on bead n, $\mathbf{F}^{n}_{elas} = -\mathbf{F}^{n-1}_{elas}$. These forces will produce opposite forces that act on the ends of the link and serve as boundary conditions for the force balance (5.4). As we do not consider any other forces ($\mathbf{K} = \mathbf{0}$) on the link, (5.4) becomes

$$\frac{d\mathbf{N}}{ds} = \mathbf{0} \tag{5.8}$$

and from the boundary conditions $\mathbf{N} = \mathbf{F}_{elas}^{n-1}$. Since there are no external torques on the link, $\boldsymbol{\tau} = \mathbf{0}$ and the moment balance (5.5) reduces to

$$\frac{d\mathbf{M}}{ds} + \mathbf{t} \times \mathbf{F}_{elas}^{n-1} \quad = \quad \mathbf{0}. \tag{5.9}$$

It remains to determine the resulting link shape by solving (5.9) with the constitutive law (5.6). Using the Euler angles $(\Phi(s), \Theta(s), \Psi(s))$ to describe the continuous deformation of the link between the two ends, the orientation of the coordinate system $(\mathbf{t}, \mathbf{p}, \mathbf{q})$ along the link relative to the coordinate system at $s = 0$ $(\mathbf{t}_{n-1}, \mathbf{p}_{n-1}, \mathbf{q}_{n-1})$ is

$$\begin{bmatrix} \mathbf{t} \\ \mathbf{p} \\ \mathbf{q} \end{bmatrix} = \mathcal{A}(s) \begin{bmatrix} \mathbf{t}_{n-1} \\ \mathbf{p}_{n-1} \\ \mathbf{q}_{n-1} \end{bmatrix}. \tag{5.10}$$

with

$$\mathcal{A} = \begin{bmatrix} \cos\Theta\cos\Phi & \cos\Theta\sin\Phi & -\sin\Theta \\ \sin\Psi\cos\Phi\sin\Theta - \sin\Phi\cos\Psi & \sin\Psi\sin\Phi\sin\Theta + \cos\Phi\cos\Psi & \sin\Psi\cos\Theta \\ \cos\Phi\cos\Psi\sin\Theta + \sin\Psi\sin\Phi & \cos\Psi\sin\Phi\sin\Theta - \sin\Psi\cos\Phi & \cos\Psi\cos\Theta \end{bmatrix}. \tag{5.11}$$

Using this expression for $\mathbf{t}$ in (5.6) and (5.9) and recognizing Ψ as the twist angle we obtain the differential equations

$$\begin{aligned} C\frac{d^2\Psi}{ds^2} &= 0 \\ \kappa\frac{d^2\Theta}{ds^2} + \kappa\cos\Theta\sin\Theta\left(\frac{d\Phi}{ds}\right)^2 + C\cos\Theta\frac{d\Phi}{ds}\frac{d\Psi}{ds} &= \lambda_1\cos\Phi\sin\Theta \\ &\quad +\lambda_2\sin\Phi\sin\Theta + \lambda_3\cos\Theta \\ \kappa\cos\Theta\frac{d^2\Phi}{ds^2} - 2\kappa\sin\Theta\frac{d\Theta}{ds}\frac{d\Phi}{dl} - C\frac{d\Theta}{ds}\frac{d\Psi}{ds} &= \lambda_1\sin\Phi - \lambda_2\cos\Phi. \end{aligned} \tag{5.12}$$

In the experiments, the length of the DNA molecules linking the beads are a fraction (10%) of a bead's diameter [33] and, therefore, we do not expect a large variation in the radius of curvature along the length of the link. We are then justified in considering the linearized version of (5.12)

$$\begin{aligned} C\frac{d^2\Psi}{ds^2} &= 0 && (5.13)\\ \kappa\frac{d^2\Theta}{ds^2} &= \lambda_1\Theta + \lambda_3 && (5.14)\\ \kappa\frac{d^2\Phi}{ds^2} &= \lambda_1\Phi - \lambda_2. && (5.15) \end{aligned}$$

Finally, to obtain the shape of the link, we solve equations (5.13)-(5.15) subject to clamped end boundary conditions

$$\begin{aligned} (\Psi,\Theta,\Phi) &= (0,0,0) \text{ at } s=0\\ (\Psi,\Theta,\Phi) &= (\Psi_n,\Theta_n,\Phi_n) \text{ at } s=l && (5.16) \end{aligned}$$

The solution to (5.13) with these boundary conditions is

$$\Psi(s) = C\frac{\Psi_n}{l}s. \tag{5.17}$$

The solutions to the bending equations (5.14) and (5.15) depend on the sign of λ_1 and are provided below.

In addition to the forces $\mathbf{F}^{n-1}_{elas}$ and $-\mathbf{F}^{n}_{elas}$, the link exerts elastic torques on the particles,

$$\begin{aligned} \boldsymbol{\tau}^{n-1}_{elas} &= \mathbf{M}(0) + a_{n-1}(\mathbf{t}_{n-1}\times\mathbf{F}^{n-1}_{elas})\\ \boldsymbol{\tau}^{n}_{elas} &= -\mathbf{M}(l) - a_n(\mathbf{t}_n\times\mathbf{F}^{n}_{elas}) && (5.18) \end{aligned}$$

that are balanced by the viscous torques on each bead

$$\boldsymbol{\tau}^{n}_{hydro} + \boldsymbol{\tau}^{n}_{elas} = 0. \tag{5.19}$$

The value of effective bending modulus of the filament, K_b, is related to the bending modulus of the link through $K_b = (2a+l)\kappa/l$. This is a result of requiring that the bending moment of a continuous filament of constant radius of curvature and length $2a+l$ be equal to that generated by a short link of length l connecting two rigid segments each of length a if the beginning and end points in the two scenarios are coincident.

5.3.1 Case I: $\lambda_1 = 0$

In this case, (5.14) and (5.15) reduce to

$$\kappa \frac{d^2\Phi}{ds^2} = -\lambda_2 \tag{5.20}$$

$$\kappa \frac{d^2\Theta}{ds^2} = \lambda_3 \tag{5.21}$$

which after applying the boundary conditions have solutions

$$\Phi(s) = \frac{-\lambda_2}{2\kappa}(s-l)s + \Phi_n s/l \tag{5.22}$$

$$\Theta(s) = \frac{\lambda_3}{2\kappa}(s-l)s + \Theta_n s/l. \tag{5.23}$$

5.3.2 Case II: $\lambda_1 < 0$

In this situation we have

$$\kappa \frac{d^2\Phi}{ds^2} + |\lambda_1|\,\Phi = -\lambda_2 \tag{5.24}$$

$$\kappa \frac{d^2\Theta}{ds^2} + |\lambda_1|\,\Theta = \lambda_3. \tag{5.25}$$

which have general solutions

$$\Phi(s) = D_1 \cos\left(\sqrt{|\lambda_1|/\kappa} s\right) + D_2 \sin\left(\sqrt{|\lambda_1|/\kappa} s\right) - \lambda_2/|\lambda_1| \tag{5.26}$$

$$\Theta(s) = D_3 \cos\left(\sqrt{|\lambda_1|/\kappa} s\right) + D_4 \sin\left(\sqrt{|\lambda_1|/\kappa} s\right) + \lambda_3/|\lambda_1| \tag{5.27}$$

Upon applying the clamped end boundary conditions, we see

$$D_1 = \lambda_2/|\lambda_1| \tag{5.28}$$

$$D_2 = \frac{\Phi_n - \lambda_2/|\lambda_1|\left(\cos\left(\sqrt{|\lambda_1|/\kappa} l\right) - 1\right)}{\sin\left(\sqrt{|\lambda_1|/\kappa} l\right)} \tag{5.29}$$

$$D_3 = -\lambda_3/|\lambda_1| \tag{5.30}$$

$$D_4 = \frac{\Theta_n + \lambda_3/|\lambda_1|\left(\cos\left(\sqrt{|\lambda_1|/\kappa} l\right) - 1\right)}{\sin\left(\sqrt{|\lambda_1|/\kappa} l\right)} \tag{5.31}$$

5.3.3 Case III: $\lambda_1 > 0$

Here,

$$\kappa \frac{d^2\Phi}{ds^2} - |\lambda_1|\,\Phi \quad = \quad -\lambda_2 \tag{5.32}$$

$$\kappa \frac{d^2\Theta}{ds^2} - |\lambda_1|\,\Theta \& = \quad \lambda_3. \tag{5.33}$$

The general solutions are

$$\Phi(s) \quad = \quad E_1 \cosh\left(\sqrt{|\lambda_1|/\kappa}s\right) + E_2 \sinh\left(\sqrt{|\lambda_1|/\kappa}s\right) + \lambda_2/|\lambda_1| \tag{5.34}$$

$$\Theta(s) \quad = \quad E_3 \cosh\left(\sqrt{|\lambda_1|/\kappa}s\right) + E_4 \sinh\left(\sqrt{|\lambda_1|/\kappa}s\right) - \lambda_3/|\lambda_1| \tag{5.35}$$

and the boundary conditions imply

$$E_1 \quad = \quad -\lambda_2/|\lambda_1| \tag{5.36}$$

$$E_2 \quad = \quad \frac{\Phi_n + \lambda_2/|\lambda_1|\left(\cosh\left(\sqrt{|\lambda_1|/\kappa}l\right) - 1\right)}{\sinh\left(\sqrt{|\lambda_1|/\kappa}l\right)} \tag{5.37}$$

$$E_3 \quad = \quad \lambda_3/|\lambda_1| \tag{5.38}$$

$$E_4 \quad = \quad \frac{\Theta_n - \lambda_3/|\lambda_1|\left(\cosh\left(\sqrt{|\lambda_1|/\kappa}l\right) - 1\right)}{\sinh\left(\sqrt{|\lambda_1|/\kappa}l\right)} \tag{5.39}$$

5.3.4 Filament Falling Under Gravity

Before examining the artificial swimmer, we test the elastic coupling scheme by first considering a microfilament settling under gravity in a viscous fluid. The filament is initially straight and subject to constant force per unit length of strength $\mathbf{F}_x = F_x\hat{\mathbf{y}}$ that is perpendicular to the filament's axis of symmetry. This problem was initially considered in [73] employing a particle based model with a worm-like chain description of the elastic forces [83], $\mathbf{F}^n_{elas}$, and using Stokeslets to provide the hydrodynamic interactions. The motion for each particle is therefore

$$\mathbf{V}^n = \frac{\mathbf{F}^n}{\gamma_0} + \frac{1}{8\pi\eta}\sum_{m\neq n}\left(\frac{\mathbf{F}^m}{r_{nm}} + \mathbf{F}^m \cdot \frac{\mathbf{x}_{nm}\mathbf{x}_{nm}}{r^3_{nm}}\right). \tag{5.40}$$

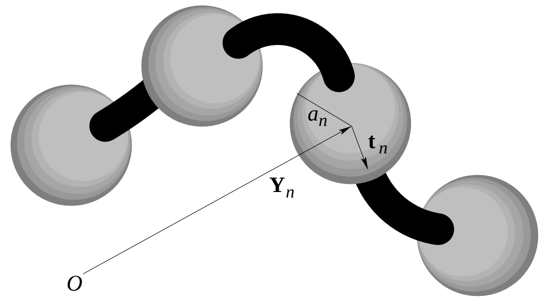

Figure 5.3: Sketch of a section of the filament tail showing the position, $\mathbf{Y}_n$, radius a_n, and the unit vector $\mathbf{t}_n$ for bead n. The vector $\mathbf{t}_n$ points from the particle's center to attachment point of the link.

where N is the number of beads, $F^n = \mathbf{F}^n_{elas} + \mathbf{F}_x L/N$, and γ_0 is the drag coefficient for a single bead.

Depending on the magnitude of the gravitational force relative to bending forces $B = L^3 F_x/K_b$, the filament will deform into different shapes as it settles. For low values of B, the filament bends slightly and the amplitude of this deformation grows linearly with the B. At moderate values of B, the deformation a nonlinear regime emerges. The filament takes on a 'U' shape and the net drag coefficient, $\gamma_\perp = F_x L/V_s$, where V_s is the equilibrium settling velocity, changes abruptly. At high values of B, the filament first forms a metastable 'W' shape which eventually relaxes to a 'horseshoe' shape. In this regime, the amplitude of the deformation and the net drag coefficient are independent of changes in B.

In our simulations of this behavior, we consider a chain of $N = 31$ beads. Each bead $n = 1 \ldots N$ centered at $\mathbf{Y}_n$ has local body axes $(\mathbf{t}_n, \mathbf{p}_n, \mathbf{q}_n)$ and is of radius a_n, where $a_n = a$ for $n = 1 \ldots N$. The unit vector $\mathbf{t}_n$ is defined such that the locations of points on the surface of sphere n where the two links are attached are $\mathbf{Y}_n \pm a_n \mathbf{t}_n$ 5.3. The length of the links between the beads was set to $l = 0.2a$ and the total length of the filament is taken to be $L = N(2a + l) - l$. The elastic forces and torques on each bead is determined using the elastic coupling method described in the previous section and the mobility problem is solved using the full FCM formulation (monopole and dipole) to obtain $\mathbf{V}_n$ and $\mathbf{\Omega}_n$. We then numerically integrate the equations of motion

$$\frac{d\mathbf{Y}_n}{dt} = \mathbf{V}_n \tag{5.41}$$

$$\frac{d\mathbf{t}_n}{dt} = \mathbf{\Omega}_n \times \mathbf{t}_n \tag{5.42}$$

$$\frac{d\mathbf{p}_n}{dt} = \mathbf{\Omega}_n \times \mathbf{p}_n \tag{5.43}$$

$$\frac{d\mathbf{q}_n}{dt} = \mathbf{\Omega}_n \times \mathbf{q}_n \tag{5.44}$$

for each bead n using an explicit, stiffly-stable-based first order scheme [62] which is necessary to address the numerically stiff problem introduced by elastic coupling. As the positions and orientations are updated, the inextensibility constraints for each link (5.7) are verified. As necessary, the values of $(\lambda_1, \lambda_2, \lambda_3)$ for a given link are adjusted by a penalty scheme to keep the deviation in length below the strict tolerance $2.5 \times 10^{-4} l$. With the penalty scheme, the forces are updated in an iterative fashion such that if the resulting motion of the beads does not comply with the set of constraints, that timestep is rejected and the elastic forces are modified in proportion to the deviation from the constraint. The motion is then recomputed with the new elastic forces, but for the same particle configuration. The process is repeated, if necessary, and the timestep is accepted only once the constraints are satisfied.

After a transient period, the viscous stresses and the elastic forces along the length of the filament balance and an equilibrium shape is achieved. The magnitude of the deformation A, the difference in the y-component between the middle bead and the end beads, and the net drag coefficient $\gamma^{\perp} = F_x L / V_s$ are then calculated over a range of the gravitational force $1 < B < 3000$.

As in [73], we find that depending upon the magnitude of B, the filament will deform into different (Figure 5.4). The values of A/L are shown as the black circles in Figure 5.5(a) and correspond well with those of [73]. The values of the effective drag coefficient relative to the rigid drag coefficient $\gamma_{\perp}/\gamma_{\perp}^{0}$ are determined by dividing the total force on the filament by the velocity of the center of mass achieved in its final equilibrium state. These values correspond to the black circles in Figure 5.5(b). As compared to [73], we find that the transition to a lower effective drag coefficient occurs at a higher value of B and that the ratio $\gamma^{\perp}/\gamma_{0}^{\perp}$ is higher in our case by approximately 10%.

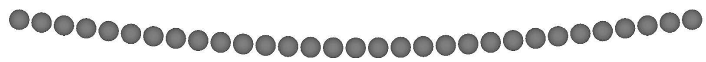

(a)

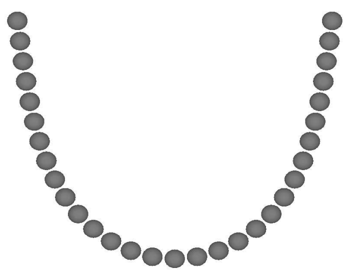

(b)

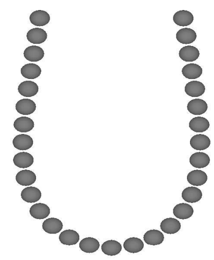

(c)

Figure 5.4: Equilibrium shapes of the filament for different values of B (a) $B = 45.6$ (b) $B = 455.9$ (c) $B = 3647.1$

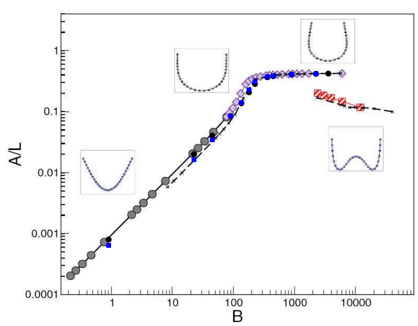

(a)

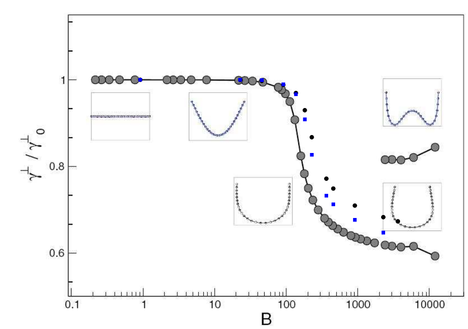

(b)

Figure 5.5: (a) Magnitude of the deformation relative to the length of the filament, A/L, versus B (b) Changes in the effective perpendicular drag coefficient $\gamma^{\perp}$ over a range of B. Data from [73] are the lines with the symbols while the FCM simulations presented here are the black circular markers and our Stokeslet simulation are the blue squares. The inset images of the filament equilibrium shapes are taken from [73].

To demonstrate the differences in the data is a result of the hydrodynamic modeling, we conducted a second set of simulations where we employ the Stokeslet-type hydrodynamic interactions (5.40) used in [73] with the bead friction coefficient given by $\gamma_0 = 6\pi\eta(1.055a)$. The results from these simulations are shown as the blue squares in Figures 5.5(a) and 5.5(b). In this case, a better agreement with the results of [73] is found. We note that the exact hydrodynamic model of [73] can not be reproduced since the value of γ_0 is not provided. Various values of γ_0 were tried and found to affect the filament drag coefficient primarily in the rigid limit.

5.4 Simulations of Planar Actuation of the Artificial Swimmer

To conduct simulations of the artificial micro-swimmer actuated by the planar field 5.1, we treat the magnetic swimmer as a series of $N+1$ rigid spheres where the first N beads are paramagnetic and comprise the filament tail. Bead $N+1$ is a large, non-paramagnetic sphere and provides a representation of the artificial swimmer's red blood cell cargo [33]. While the large sphere will not mimic exactly the response of the non-spherical, non-rigid red blood cell, the purpose is not to provide an exact description of this swimmer but rather yield a simulation that accurately describes this form of propulsion. Each bead $n = 1 \ldots N+1$ centered at $\mathbf{Y}_n$ has local body axes $(\mathbf{t}_n, \mathbf{p}_n, \mathbf{q}_n)$ and is of radius a_n, where $a_n = a$ for the paramagnetic spheres $n = 1 \ldots N$ and $a_{N+1} = R$ for the large sphere. In the experiments, the ratio $R/a \approx 6.0$ [33]. The unit vector $\mathbf{t}_n$ is defined such that the locations of points on the surface of sphere n where the two links are attached are $\mathbf{Y}_n \pm a_n \mathbf{t}_n$. Additionally, magnetic beads comprising the tail have magnetic permeability μ. The permeability of the surrounding medium is taken to be that of free space μ_0. The length of the linkages is $l = 0.2a$ and corresponds to the length of the DNA molecules binding adjacent beads in the experiments [33]. The total filament length is defined as $L = N(2a+l) - l = (2.2N - 0.2)a$. The magnitude of the magnetic field, H_0, and the frequency of the magnetic field, ω, are chosen to yield the desired values of the Mn and Sp.

The equations of motion for each bead are given by the force balance at each instant

$$\mathbf{F}^n_{hydro} + \mathbf{F}^n_{mag} + \mathbf{F}^n_{elas} = 0 \tag{5.45}$$

$$\boldsymbol{\tau}^n_{hydro} + \boldsymbol{\tau}^n_{elas} = 0 \tag{5.46}$$

for $n = 1 \ldots N$. The force and torque balance for $n = N + 1$ is the same except there are no magnetic forces to consider. The magnetic forces are given by the mutual dipole method, the elastic coupling is provided by the model described in this chapter. FCM is used to solve the mobility problem and the particle positions and orientations are updated using the numerical scheme and penalty method employed for the simulations of a falling filament.

We first consider the case where $Mn = 10$ and $h_0 = 1.0$ over a range of Sp are fixed. $N = 15$ beads comprise the each swimmer's filament tail giving a length $L = 32.8a$. The radius of the tethered sphere is $R = 6.0a$, and therefore $R/L = 0.183$.

In Figure 5.6, we show the scaled swimming speed of the device as a function of Sp. Just as in the experiments, we find that the scaled speed will initially grow with Sp to a peak value, after which the speed will monotonically decay with increasing Sp. To understand this behavior, we show time composite images of the swimmer over the course of one period for different values of Sp (Figure 5.7). At low Sp, the effects of the viscous stresses are minimal, and the resulting motion of the swimmer is nearly a rigid rotation (Figure 5.7(a)). Consequently, the translation of the swimmer is limited. As Sp increases, we see in Figure 5.7(b) the deformation of the filament becomes significant, and the swimming speed increases. If, however, Sp is too great, the viscous stresses become overwhelming and diminish the amplitude of the deformation and the swimming speed as in Figures 5.7(c) and 5.7(d).

5.4.1 Comparison with Experiments

The swimming speeds measured by [33] and computed by [44] are also shown in Figure 5.8. For the case considered, $M_n = 16$, $h_0 = 1.16$, and $R/L = 0.129$. The swimming speeds given by simulations and those observed in the experiments are comparable, especially at high Sp. The discrepancies between the simulation and experimental results at lower Sp are attributed to the presence of a nearby surface in the experiments and the deformability

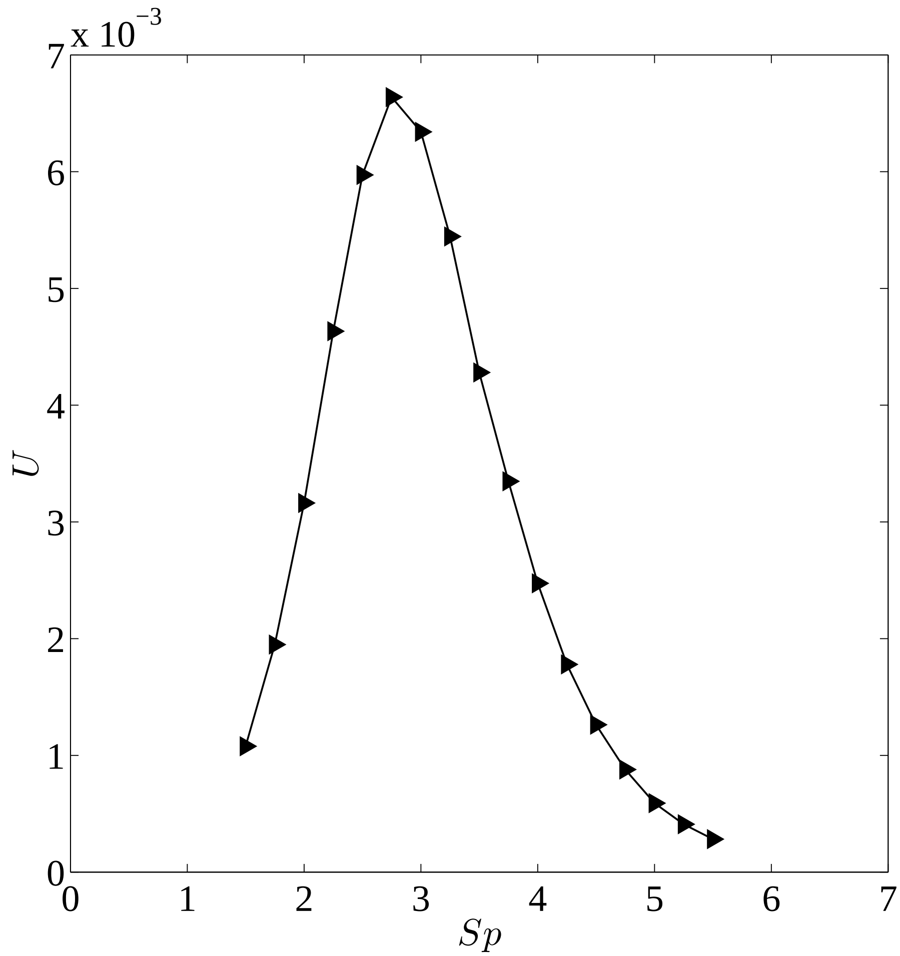

Figure 5.6: The scaled swimming speed U versus Sp for a planar swimmer with $Mn = 10$ and $h_0 = 1.0$.

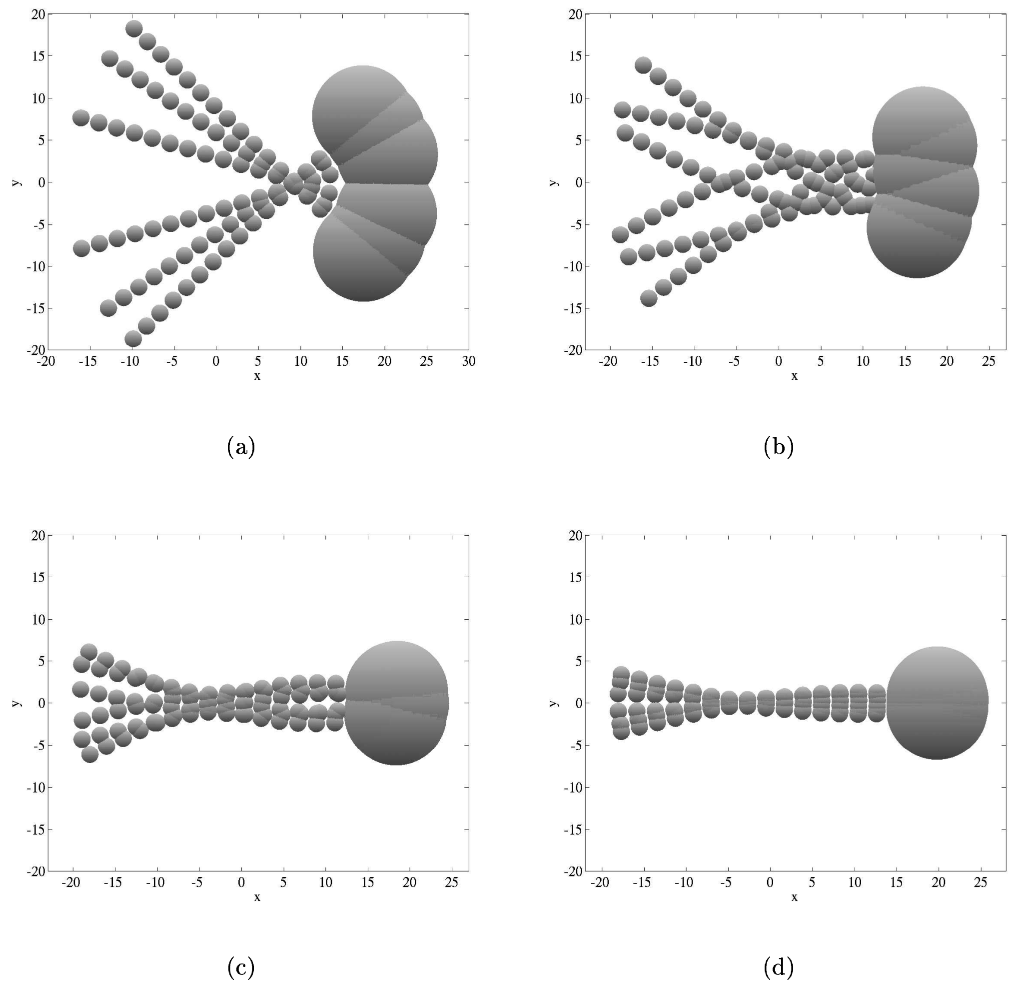

Figure 5.7: Time composite images of the motion of a planar swimmer over the course of one period with $Mn = 10$, $h_0 = 1.0$ and (a) $Sp = 1.5$ (b) $Sp = 3.0$ (c) $Sp = 4.5$ (d) $Sp = 5.5$

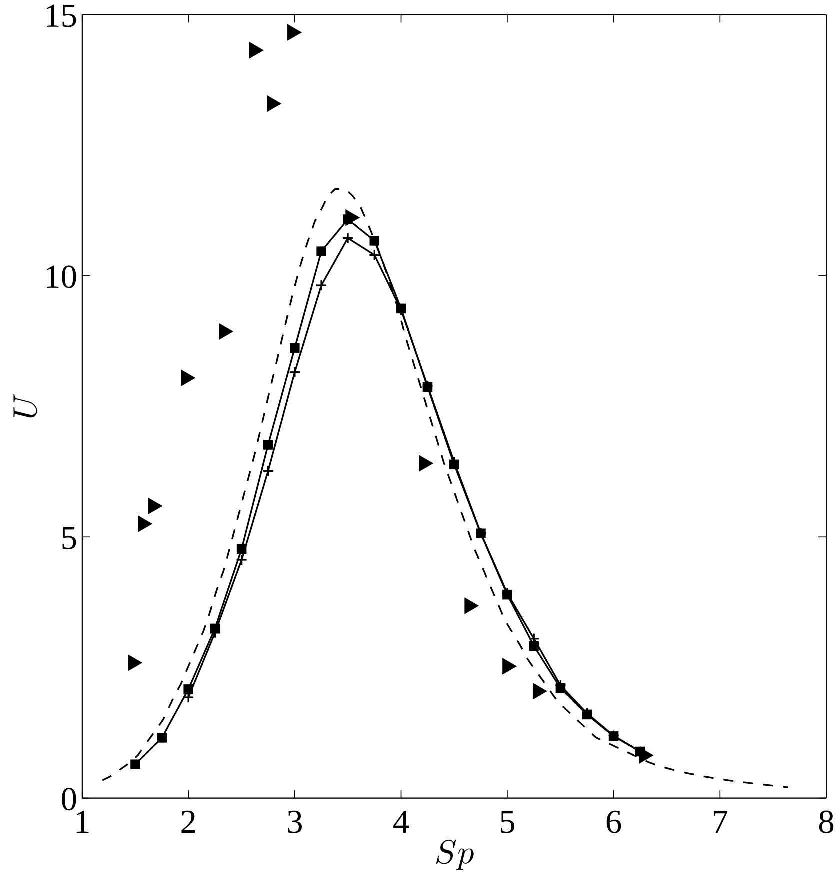

Figure 5.8: Scaled swimming speed U of a single swimmer as a function of sperm number S_p. The motion is generated by the magnetic field (5.1) with $Mn = 16$, $h_0 = 1.16$, and $R/L = 0.129$. The solid line with the square markers shows the scaled swimming speeds obtained using only FCM monopoles to resolve the hydrodynamics. The solid line with the crosses was obtained using the full hydrodynamic model. The triangle markers are the experimental results from [33] while the dashed line was obtained by [44].

and oblate shape of the red blood cell. Such conditions change the drag on the filament and the drag and viscous torque on the tethered body. As we will see in Chapter 6, the hydrodynamic forces and torques have been shown to greatly affect the initial growth of the swimming speed. The two simulation methods do produce consistent results although the results found here did not require rescaling as they did in [44]. A severe limitation of their model is the need to have large separation distances between the particles. This separation distance is on the order on one bead radius and is much larger than the links used in the experiments. This leads to an underestimation of the magnitude of the magnetic torque on the filament tail. By using our linking procedure, the beads are quite close the net magnetic torque is well resolved.

5.5 Conclusions

In this chapter, we developed a simulation technique to study the artificial micro-swimmer employing FCM, the mutual dipole model and an elastic coupling model presented in §5.3. This model treats each chemical link in the filament tail separately based on solution to linearized beam equations. To test this model, we considered the change in shape and drag of a microfilament falling under gravity. We then conducted simulations of the artificial swimmer actuated by a planar field and found agreement with the experiments at higher frequencies. With the simulation methods developed, we may now examine the behavior of the artificial when subject to alternative fields or situations where two swimmer are allowed to interact.

Chapter 6

The spiral swimming of an artificial micro-swimmer

6.1 Introduction

In this chapter, we demonstrate the artificial micro-swimmer can also be used to study corkscrew-type swimming. Using the particle-based simulation techniques described in the previous chapter, we find that when driven by the field

$$\mathbf{H} = -H_0\left(1, h_0 \sin \omega t, h_0 \cos \omega t\right). \tag{6.1}$$

the balance of the magnetic, viscous and elastic forces cause the swimmer to take on a spiral shape. Additionally, the swimmer will rotate at the same frequency as the applied field, and therefore, translate through the fluid. The results from these simulations are presented in §6.2 from which the kinematics of the swimmer's motion are deduced and analyzed. The variation of the swimming speed with the frequency of the applied field is examined.

Along with the particle-based description and simulations, we consider the alternative model where the magnetic filament tail is treated as a continuous elastica subject to magnetic torques and hydrodynamic drag. These simplifications yield a description that includes the features essential to the motion, but is still accessible to analysis. This allows us to explore further the parameters governing the swimming speed and make comparisons with the more realistic particle-based simulations. In §6.3, we extend the model of [107] used in their study of magnetically driven elastic filaments to include fully three-dimensional motion and a higher level representation of the magnetic interactions. An analysis of spiral swimming at low frequency is then given in §6.4.

6.2 Simulation Results

Using the particle-based simulation for the artificial swimmer described in the previous chapter, we perform simulations of a swimmer with $N = 15$ and $R = 6.0a$ driven by the magnetic field (6.1) to determine the scaled swimming speed, U, over the range $1 \leq Sp \leq 6$ for $Mn = 5$, 10 and 15. The remaining parameters are identical those used in the simulations of the planar actuated artificial swimmer described in the previous chapter.

Figures 6.1 and 6.2 show the kinematics of the motion over one period for various Sp with $Mn = 10$. The resulting scaled swimming speeds over this range of Sp are provided in Figure 6.3(a). In each case, the direction of swimming is such that the tethered end is at the rear of the swimmer as it swims 'tail first.' At low Sp, the filament tail remains aligned with the applied field, and together the tail and cell head rotate as a rigid body (Figures 6.1(a) and 6.1(b)). Such a motion is reciprocal, or time reversible, and accordingly, does not exhibit a net translation [103]. Also, at low frequencies, there is significant motion of the large sphere at the tethered end as the swimmer pivots about a point within the tail. As the driving frequency is increased, viscous stresses become significant causing the filament to deform into a spiral shape (Figures 6.1(c) and 6.1(d)). Over this range of frequencies we see the swimming speed increase as the subsequent rotation of the spiral shape allows for the swimmer's translation through the fluid. If Sp is increased beyond the value corresponding to the peak swimming speed, the swimming speed is reduced as the amplitude of the deformation is diminished by the overwhelming viscous stresses (Figures 6.2(c) and 6.2(d)). The variation of scaled swimming speed with Sp for planar actuation behaves in a similar manner [44].

In Figure 6.3(a) we see that increasing Mn leads to a greater peak swimming speeds. At low Sp, the rate at which the swimming speed grows decreases with increasing Mn. This is a result of the filament tail's ability to remain straight and aligned with the field at greater field strengths. Figure 6.3(b) compares the scaled swimming speeds achieved from the use of the oscillating field (5.1) to those produced by the rotating field with $Mn = 10$. The scaled swimming speeds resulting from planar actuation are computed using the present methods

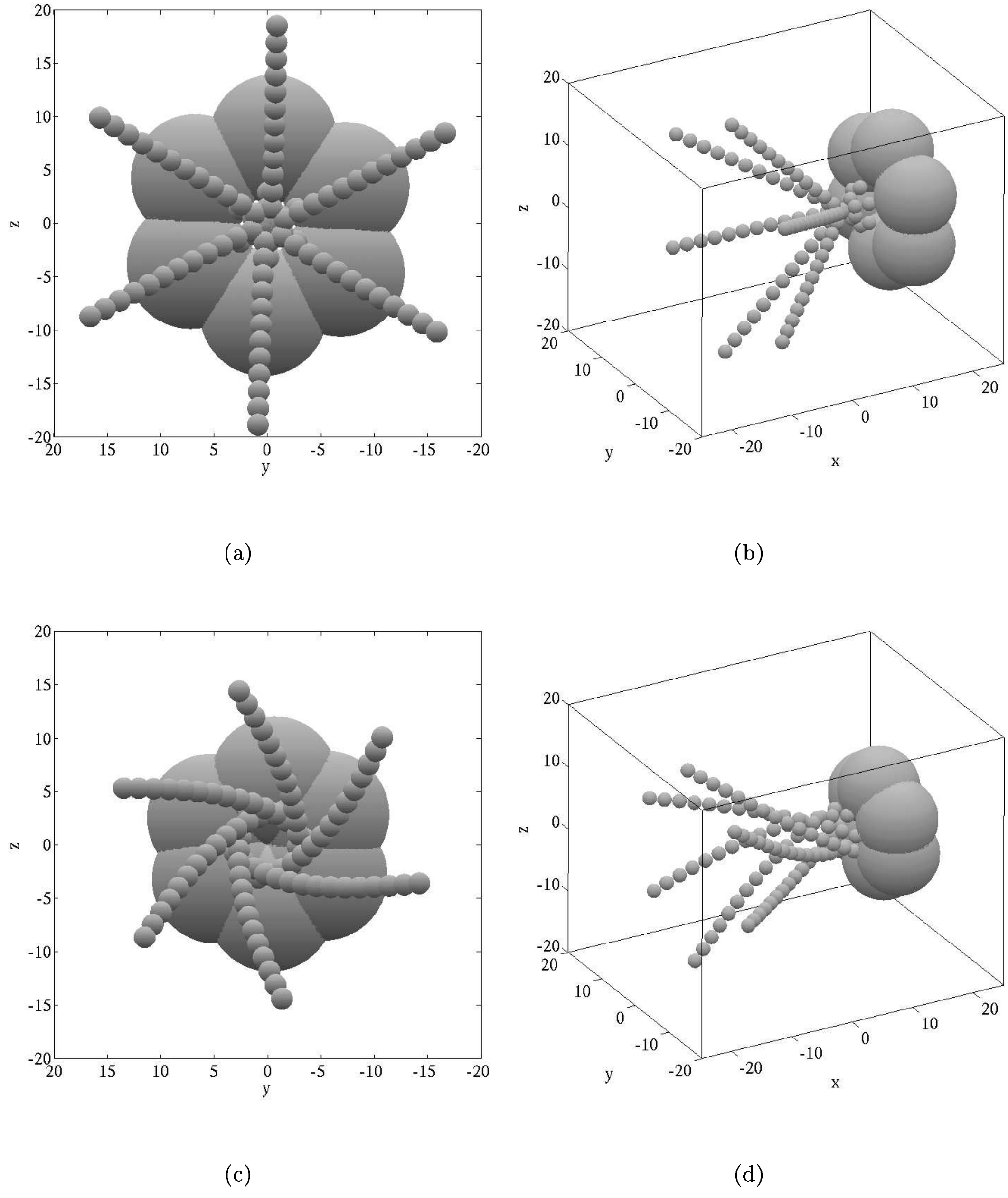

Figure 6.1: End on and oblique views of the time composite kinematics of the magnetic micro-swimmer over the course of one period with $R/L = 0.183$, $h_0 = 1.0$ and $Mn = 10$. (a) and (b) correspond to $Sp = 1.5$ and (c) and (d) to $Sp = 3.0$.

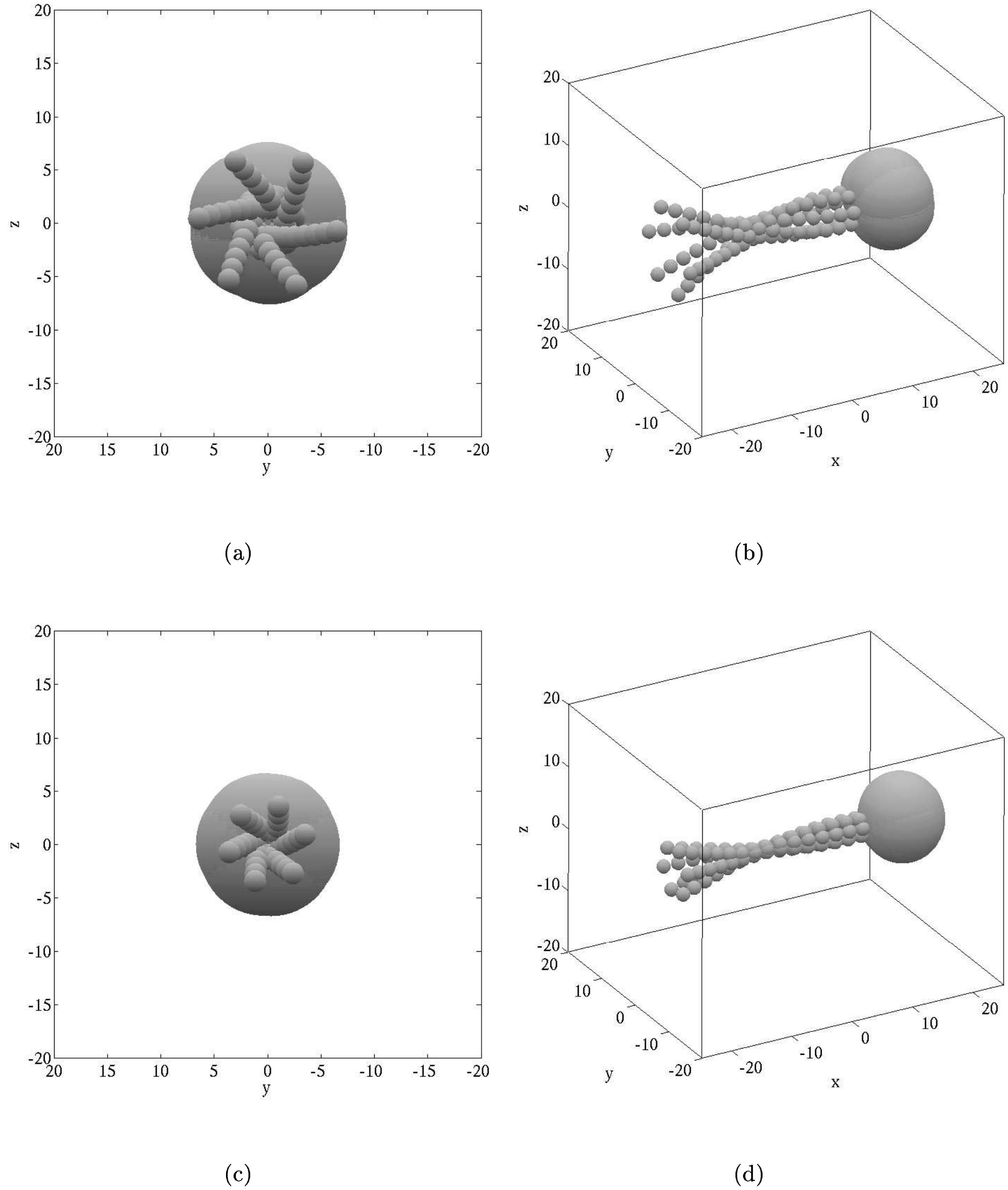

Figure 6.2: End on and oblique views of the time composite kinematics of the magnetic micro-swimmer over the course of one period with $R/L = 0.183$, $h_0 = 1.0$ and $Mn = 10$. (a) and (b) correspond to $Sp = 4.5$ and (c) and (d) to $Sp = 5.5$.

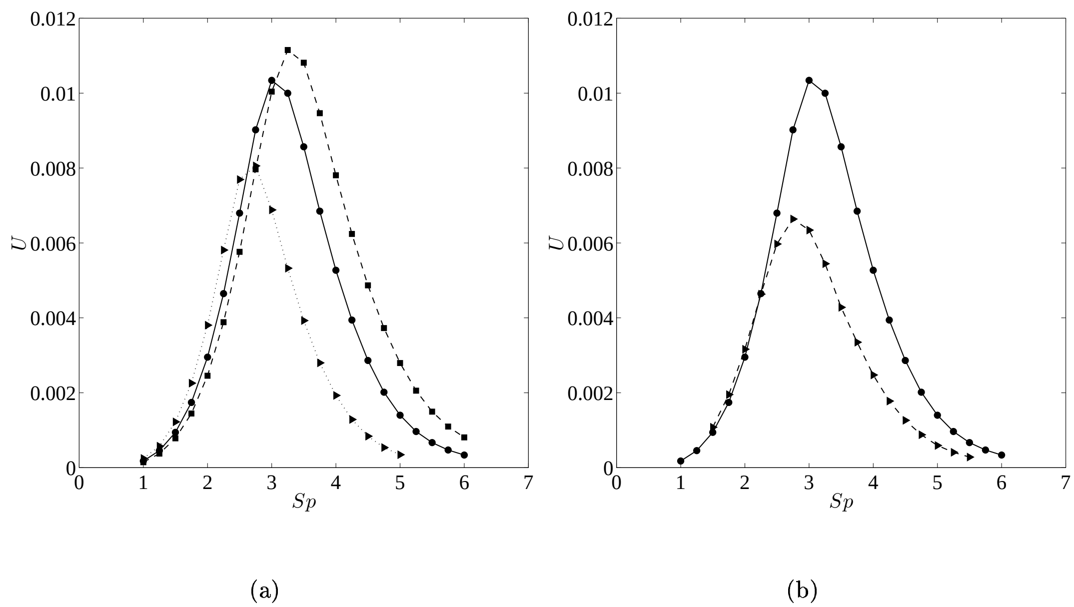

Figure 6.3: Scaled swimming speed U versus sperm number. (a) Scaled swimming speed computed using full hydrodynamic model. The dotted line with triangular markers correspond to $Mn = 5$, the solid line with the circular markers are the $Mn = 10$ data and the dashed line with the square markers is the $Mn = 15$ case. (b) Scaled swimming speed for $Mn = 10$ for different strategies. The solid line with circular markers corresponds to the rotary scheme (6.1) and the dashed line with square markers the planar strategy (5.1).

and are consistent with those of [33] and [44]. While the swimming speeds are comparable at lower Sp, the speed of the swimmer in the planar oscillating field reaches its maximum value while that of the spiral swimmer continues to grow. The maximum speed for the swimmer in the rotating magnetic field is 60% greater than that in the planar oscillating field. The magnitude of the rotating field (6.1) remains constant but the oscillating field (5.1) fluctuates in magnitude and on average is smaller.

From the simulations, it is observed that regardless of the value of Sp, the balance of the viscous, magnetic and elastic forces induces a corkscrew shape whose pitch and distance from the x-axis vary along the length of the filament (Figures 6.1 and 6.2). The resulting shape rotates about the x-axis with the same frequency as the applied field. Such a stationary shape is also exhibited by a non-magnetic elastic filament with a torque applied to one end [87]. Although for the cases considered here a time-independent shape was exhibited by the swimmer, above a critical frequency of the applied field, this may not be the case especially if $h_0 > 1$. In this regime, the phase shift will increase in time until, eventually, the applied torque will reverse its direction leading to a reversal in the rotation of the filament [21]. This behavior is related to that exhibited by a pair of non-magnetic particles in a ferrofluid subject to a rotating field [51].

The steady state position along the filament arclength s at time t may be described as

$$x(s,t) = \alpha(s) - Vt \tag{6.2}$$

$$y(s,t) = -b(s)\sin(\omega t + \phi(s)) \tag{6.3}$$

$$z(s,t) = -b(s)\cos(\omega t + \phi(s)) \tag{6.4}$$

where $\alpha(s)$ is the x-component at $t = 0$, $b(s)$ is the distance from the x-axis, and $\phi(s)$ is the phase shift [78]. The arclength is measured relative to the free end. Differentiating in time, the resulting velocity is

$$\mathbf{v} = (-V, 0, 0) + (-\omega, 0, 0) \times (x, y, z). \tag{6.5}$$

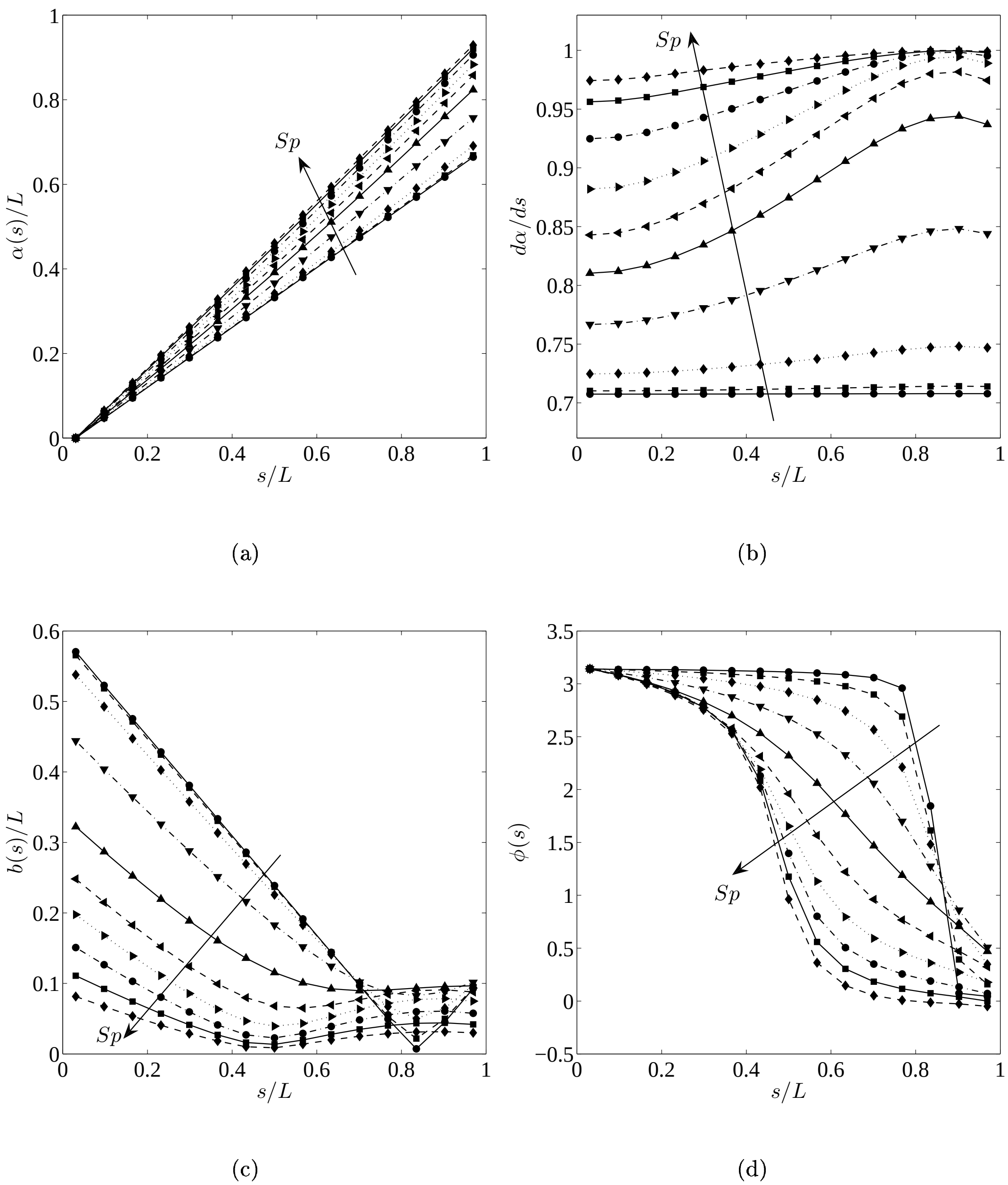

Figure 6.4: The variation of (a) $\alpha(s)$, (b) $d\alpha/ds(s)$, (c) $b(s)$, and (d) $\phi(s)$ with arclength s with $Mn = 10$. The values of $\alpha(s)$ and $\phi(s)$ are given relative to those of the bead at the free end for which $s = a$, $\alpha(a) = 0$, and $\phi(a) = \pi$. The curves in each plot are for different Sp which begin at $Sp = 1.5$ and increase by increments of 0.5 to $Sp = 6.0$.

Writing $\nu = \omega t + \phi(s)$, the vector tangent to the curve is given by

$$\begin{aligned} \mathbf{t} &= (\partial x/\partial s, \partial y/\partial s, \partial z/\partial s) \\ &= \left(\frac{d\alpha}{ds}, -\frac{db}{ds}\sin\nu - b\frac{d\phi}{ds}\cos\nu, -\frac{db}{ds}\cos\nu + b\frac{d\phi}{ds}\sin\nu\right) \end{aligned} \tag{6.6}$$

and inextensibility of the filament implies

$$\left(\frac{d\alpha}{ds}\right)^2 + \left(b\frac{d\phi}{ds}\right)^2 + \left(\frac{db}{ds}\right)^2 = 1. \tag{6.7}$$

Figure (6.4) shows the parameters as a function of arclength over a range of Sp. In these plots, a convention is adopted where $b(s) \geq 0$ and $\phi(a) = \pi$ and $\alpha(a) = 0$ where $s = a$ corresponds to the center of the bead at the free end. As Sp increases, the projection of the filament along the x-axis increases (Figure 6.4(a)). Figure 6.4(b) shows the x-component of $\mathbf{t}$, $d\alpha/ds$ as a function of the arclength. Since $h_0 = 1.0$, $d\alpha/ds$ at low Sp has a nearly constant value of $\cos(\pi/4)$ which corresponds to a rigid rotation aligned with the applied field. Increasing the frequency of the applied field induces a variation in $d\alpha/ds$ along the length of the filament, which in the limit of very large frequencies will remain aligned with the x-axis, $d\alpha/ds = 1$. Similarly, in Figure 6.4(c), we see the distance from the x-axis, b, decrease as the frequency is increased. Finally, in Figure 6.4(d), we see that as Sp increases, a variation in the phase shift ϕ arises, which leads to the inflection point appearing at $s/L \approx 0.83$ at low Sp moving to $s/L \approx 0.5$ at high Sp.

To tie this parameterization to the observed scaled swimming speeds and swimming directions, we employ the non-dimensional version of the resistive force model which is presented in the following section. With this model and the parameterization of the motion, an expression can be derived for the scaled swimming speed by integrating the force balance (6.29) in the x-direction and applying the boundary conditions (6.34) and (6.36). The resulting expression is

$$U = \frac{(1-\beta)\int_0^1 b^2 \frac{d\alpha}{ds}\frac{d\phi}{ds} ds}{\frac{6\pi\eta R}{\zeta_{||} L} + \beta + (1-\beta)\int_0^1 \left(\frac{d\alpha}{ds}\right)^2 ds} \tag{6.8}$$

where $\zeta_{||}$ and $\beta\zeta_{||}$ are the resistance coefficients respectively for motion tangent and normal to the tail. Immediately, it is clear that an anisotropic drag force ($\beta \neq 1$) is necessary to obtain a non-zero swimming speed [5, 76]. Other requirements include a non-zero x-component of $\mathbf{t}$, $d\alpha/ds \neq 0$, a non-zero distance from the x-axis, $b(s)$, and a variation in the phase shift, $\phi(s)$, along the length. Additionally, the dependence on b^2 of the scaled swimming speed is consistent with the results of the analysis found in [76]. From the inextensibility condition, the denominator of the above expression is positive

$$\frac{6\pi\eta R}{\zeta_{||}L} + 1 + (\beta - 1)\left(\int_0^1 \left(\frac{db}{ds}\right)^2 ds + \int_0^1 \left(b\frac{d\phi}{ds}\right)^2 ds\right) > 0 \tag{6.9}$$

as $\beta - 1 > 0$. Since $d\alpha/ds \geq 0$, $U \geq 0$ if $d\phi/ds \leq 0$ and by (6.2) the swimming velocity will be in the negative x-direction.

6.3 Resistive Force Model

Along with the particle based model, we adopt a version of the continuous elastica/resistive force model presented by [107] but extended here to allow for three dimensional deformations. The hydrodynamics are provided by simple, approximate drag laws based on slender body theory. With such a model, we are able to generate analytic results to complement and compare with our numerical results.

The entire magnetic filament tail is treated as a flexible, inextensible rod. Accordingly, the general force and moment balance equations (5.4) and (5.5) for a massless rod apply now with $0 \leq s \leq L$. External forces and torques on the filament arise due to the presence of the surrounding fluid and applied magnetic field. Specifically,

$$\frac{d\mathbf{N}}{ds} + \mathbf{K}_f = \mathbf{0} \tag{6.10}$$

$$\frac{d\mathbf{M}}{ds} + \mathbf{t} \times \mathbf{N} + \boldsymbol{\tau}_f + \boldsymbol{\tau}_m = \mathbf{0}. \tag{6.11}$$

where $\mathbf{K}_f$ is the translational drag force per unit length, $\boldsymbol{\tau}_f$ is the viscous torque per unit length and $\boldsymbol{\tau}_m$ is the magnetic torque per unit length on the filament.

6.3.1 Hydrodynamic Forces and Torques

As the filament moves through the fluid, it will experience a drag force resisting the motion. Using a resistive force theory to account for these forces gives

$$\mathbf{K}_f = -\boldsymbol{\zeta}\mathbf{v} \tag{6.12}$$

where $\mathbf{v}$ is the filament velocity and the tensor $\boldsymbol{\zeta}$ is given by

$$\boldsymbol{\zeta} = \zeta_{||} \left(\mathbf{tt} + \beta \left(\mathbf{I} - \mathbf{tt} \right) \right). \tag{6.13}$$

The drag coefficient along the tangential direction $\zeta_{||}$ and the drag anisotropy constant β are those for a line of Stokelets translating through fluid ([65])

$$\zeta_{||} = 2\pi\eta / \log(L/a) + O((\log(L/a))^{-2}) \tag{6.14}$$

$$\beta = 2. \tag{6.15}$$

where L is the length of the filament, and a is the radius of filament cross section which is equal to the radius of a paramagnetic bead. The errors introduced by resistive force theory arise since the model assumes $a \ll L$, but more importantly $|\partial \mathbf{t}/\partial s| \ll 1$.

Along with the translational drag, the fluid will resist rotations of the filament about $\mathbf{t}$ ([118])

$$\boldsymbol{\tau}_f = -\zeta_r \left(\boldsymbol{\Omega} \cdot \mathbf{t} \right) \mathbf{t} \tag{6.16}$$

with

$$\boldsymbol{\Omega} = \Omega_{||} \mathbf{t} + \mathbf{t} \times \frac{d\mathbf{t}}{dt} \tag{6.17}$$

being the angular velocity and $\zeta_r = 4\pi\eta a^2$ the coefficient for the viscous torque.

6.3.2 Magnetic Torque

In the particle based model, the magnetic interactions between the beads produced interparticle forces, but the magnetic torque on each particle was zero. As all the magnetic forces between the beads are equal and opposite, the total magnetic force on the filament is zero. The interparticle magnetic forces will, however, produce a net torque on each segment of the filament tail. Just as the drag per unit length is determined by considering a series of Stokeslets distributed along a line, we adopt a magnetic torque model where the torque per unit length

$$\boldsymbol{\tau} = \frac{\mu_0}{2d} \mathbf{m}(s) \times \mathbf{H}, \tag{6.18}$$

where $d = a + l/2$, corresponds to that on a line distribution of point dipoles. If the filament is straight, infinitely long and the beads comprising it are separated by $2a + l$, the dipole moment of each bead is

$$\mathbf{m} = \frac{4}{3}\pi a^3 \chi_{eff} \left[\mathbf{H} + 2\sum_{q=1}^{\infty} \frac{1}{4\pi} \left(\frac{3\mathbf{t}(\mathbf{t}\cdot\mathbf{m})}{8q^3d^3} - \frac{\mathbf{m}}{8q^3d^3} \right) \right]. \tag{6.19}$$

This differs from the expression derived by [107] in that the length of the link is included in the interparticle separation distance along with the magnetic interactions of all the particles and not just the adjacent pair. The inclusions of these details are important to make a quantitative comparison with the simulations. Due to the symmetry of the straight chain of beads and the linear relationship between the dipole moments and the applied field, we may decompose these quantities into their axial and transversal components

$$\mathbf{m} = (\mathbf{m}\cdot\mathbf{t})\,\mathbf{t} + (\mathbf{I} - \mathbf{tt})\,\mathbf{m} \tag{6.20}$$

$$\mathbf{H} = (\mathbf{H}\cdot\mathbf{t})\,\mathbf{t} + (\mathbf{I} - \mathbf{tt})\,\mathbf{H}. \tag{6.21}$$

Upon substitution into (6.19) the expression

$$\mathbf{m} = \frac{\frac{4}{3}\pi a^3 \chi_{eff}}{1 - \frac{\chi_{eff}}{6}\left(\frac{a}{d}\right)^3 \zeta(3)} \mathbf{t}(\mathbf{t}\cdot\mathbf{H}) + \frac{\frac{4}{3}\pi a^3 \chi_{eff}}{1 + \frac{\chi_{eff}}{12}\left(\frac{a}{d}\right)^3 \zeta(3)} (\mathbf{I} - \mathbf{tt})\,\mathbf{H}. \tag{6.22}$$

is obtained where the Riemann zeta function prefactor $\zeta(3) = \sum_{k=1}^{\infty} 1/k^3 \approx 1.2$. The resulting applied torque (6.18) is then

$$\boldsymbol{\tau}_m = \frac{\mu_0 \pi a^6 \chi_{eff}^2 \zeta(3)}{6d^4 \left(1 - (\chi_{eff}/6)\,(a/d)^3 \zeta(3)\right)\left(1 + (\chi_{eff}/12)\,(a/d)^3 \zeta(3)\right)} (\mathbf{t}\cdot\mathbf{H})\mathbf{t}\times\mathbf{H}. \tag{6.23}$$

The force and moment balance are then

$$\frac{\partial \mathbf{N}}{\partial s} = \boldsymbol{\zeta}\mathbf{v} \tag{6.24}$$

$$\boldsymbol{\tau}_m + \mathbf{t}\times\mathbf{N} + \frac{\partial \mathbf{M}}{\partial s} = \zeta_r a^2 (\boldsymbol{\Omega}\cdot\mathbf{t})\,\mathbf{t} \tag{6.25}$$

The constitutive law for the stress moment is

$$\mathbf{M} = K_b \mathbf{t} \times \frac{\partial \mathbf{t}}{\partial s} + K_t \frac{\partial \Psi}{\partial s}\mathbf{t} \tag{6.26}$$

where, as before, K_b is the effective bending modulus and K_t is the effective twist modulus of the filament.

6.3.3 Boundary Conditions

At the free end, $s = 0$, the forces and moments must vanish so $\mathbf{N} = \mathbf{0}$ and $\mathbf{M} = \mathbf{0}$. At the tethered end, $s = L$, the forces and moments are balanced by the translational and rotational drag of the sphere. Taking the filament as clamped to the sphere, the boundary conditions are

$$-\mathbf{N} - 6\pi\eta R\left(\mathbf{v} + \boldsymbol{\Omega} \times R\mathbf{t}\right) = \mathbf{0} \qquad (6.27)$$

$$-\mathbf{M} + R\mathbf{t} \times \mathbf{N} - 8\pi\eta R^3\boldsymbol{\Omega} = \mathbf{0}. \qquad (6.28)$$

6.3.4 Nondimensional Equations

The force and moment balance equations are nondimensionalized by introducing the barred variables such that $t = \bar{t}/\omega$, $s = L\bar{s}$, $\mathbf{H} = H_0\bar{\mathbf{H}}$, and $\mathbf{N} = K_b\bar{\mathbf{N}}/L^2$. On substituting these variables into the equations, and removing the bars, we obtain

$$\frac{\partial \mathbf{N}}{\partial s} = \Gamma\left[\mathbf{t}\mathbf{t} + \beta\left(\mathbf{I} - \mathbf{t}\mathbf{t}\right)\right]\mathbf{v} \qquad (6.29)$$

$$\left(\frac{\zeta_r a^2}{\zeta_{||}L^2}\right)\Gamma\Omega_{||}\mathbf{t} = Cm(\mathbf{t}\cdot\mathbf{H})\mathbf{t} \times \mathbf{H} + \mathbf{t} \times \frac{\partial^2 \mathbf{t}}{\partial s^2} + (K_t/K_b)\frac{\partial}{\partial s}\left(\frac{\partial \psi}{\partial s}\mathbf{t}\right) \qquad (6.30)$$

where

$$Cm = \frac{\mu_0 \pi a^6 \zeta(3)(\chi_{eff}H_0L)^2}{6d^4K_b\left(1 - (\chi_{eff}/6)\,(a/d)^3\,\zeta(3)\right)\left(1 + (\chi_{eff}/12)\,(a/d)^3\,\zeta(3)\right)} \qquad (6.31)$$

$$\Gamma = \zeta_{||}\omega L^4/K_b. \qquad (6.32)$$

These quantities are related to Sp and Mn introduced in the experimental studies ([33]) and described in the previous section. Specifically,

$$\Gamma = \frac{\zeta_{||}Sp^4}{4\pi\eta} \qquad (6.33)$$

and $Cm = 0.811Mn$. The difference between Cm and Mn is a result of the refinements in the magnetic torque model presented here.

The boundary conditions in terms of the dimensionless variables are

$$\mathbf{N}(0) = \mathbf{0} \tag{6.34}$$

$$\mathbf{M}(0) = \mathbf{0} \tag{6.35}$$

$$\mathbf{N}(1) = -Q_1\Gamma\left(\mathbf{v}(1) + \mathbf{\Omega} \times \frac{R}{L}\mathbf{t}(1)\right) \tag{6.36}$$

$$\mathbf{M}(1) - \frac{R}{L}\mathbf{t} \times \mathbf{N}(1) = -Q_2\Gamma\mathbf{\Omega}(1) \tag{6.37}$$

where

$$Q_1 = \frac{6\pi\eta R}{\zeta_{||}L} \tag{6.38}$$

$$Q_2 = \frac{8\pi\eta R^3}{\zeta_{||}L^3} \tag{6.39}$$

6.4 Swimming at Low Frequencies

With the force and moment balance equations from resistive force theory, we would like to understand how the swimming speed is affected by the values of relevant parameters. We are able to make some progress in this regard by considering the case where Γ is quite low. In this regime, the swimmer will remain closely aligned with the applied field and undergo nearly rigid rotation. Employing the resistive force hydrodynamic drag model to study this regime is appropriate since $|\partial\mathbf{t}/\partial s| \ll 1$. We wish to find a solution expanded, in powers of Γ, about the rigid body rotation [116, 117, 107]. From the simulations we expect the solution $\mathbf{t}$ to be of the form (6.6). Also, since the functions α, b and ϕ are time independent, it suffices to find the solution at one specific time [78]. Thus, at $t = 0$, the expansion is

$$\frac{d\alpha}{ds} = \frac{d\alpha_0}{ds} + \frac{d\alpha_1}{ds}\Gamma + O(\Gamma^2) = \frac{1}{(1+h_0^2)^{1/2}} + \frac{d\alpha_1}{ds}\Gamma + O(\Gamma^2) \tag{6.40}$$

$$\frac{db}{ds} = \frac{db_0}{ds} + \frac{db_1}{ds}\Gamma + O(\Gamma^2) = \frac{-h_0}{(1+h_0^2)^{1/2}} + \frac{db_1}{ds}\Gamma + O(\Gamma^2) \tag{6.41}$$

$$\frac{d\phi}{ds} = \frac{d\phi_1}{ds}\Gamma + O(\Gamma^2) \tag{6.42}$$

in addition to $d\Psi/ds = (d\Psi_1/ds)\,\Gamma + O(\Gamma^2)$. To avoid the discontinuity in db_0/ds, a convention where $b(s)$ is allowed to be both positive and negative is adopted. This also removes the jump in ϕ. The scaled swimming speed (6.8) is then

$$U = \frac{(1-\beta)\frac{1}{(1+h_0^2)^{1/2}}\int_0^1 b_0^2 \frac{d\phi_1}{ds} ds}{Q_1 + \beta + \frac{1-\beta}{1+h_0^2}}\Gamma + O(\Gamma^2) = \bar{U}\Gamma + O(\Gamma^2). \tag{6.43}$$

From this expression, one not only sees that on deviation from a rigid body motion the swimming speed is $O(\Gamma)$, but also it is the result of the $O(\Gamma)$ variation in the phase shift over the length of the filament. The inextensibility condition (6.7) at $O(\Gamma)$ implies

$$\frac{d\alpha_1}{ds} = h_0 \frac{db_1}{ds}. \tag{6.44}$$

Defining $b_0 = -\frac{h_0}{(1+h_0^2)^{1/2}}s + C_1$ and noting that at $t = 0$, $\sin\nu = \phi_1\Gamma + O(\Gamma^2)$ and $\cos\nu = 1 + O(\Gamma^2)$, the expansions for the scaled filament velocity and the tangent vector are

$$\begin{aligned}
\mathbf{v} &= \mathbf{v}_0 + \mathbf{v}_1\Gamma + O(\Gamma^2) && (6.45)\\
&= (0, -b_0, 0) + \left(-\bar{U}, 0, b_0\phi_1\right)\Gamma + O(\Gamma^2) && (6.46)\\
\mathbf{t} &= \mathbf{t}_0 + \mathbf{t}_1\Gamma + O(\Gamma^2) && (6.47)\\
&= \left(1/(1+h_0^2)^{1/2}, 0, -h_0/(1+h_0)^{1/2}\right)\\
&\quad + \left(h_0\frac{db_1}{ds}, -\frac{d(b_0\phi_1)}{ds}, \frac{db_1}{ds}\right)\Gamma + O(\Gamma^2). && (6.48)
\end{aligned}$$

Since $O(1)$ rotations about $\mathbf{t}$ are not expected, the appropriate expansion for the dimensionless angular velocity (6.17) is

$$\begin{aligned}
\boldsymbol{\Omega} &= \boldsymbol{\Omega}_0 + \boldsymbol{\Omega}_1\Gamma + O(\Gamma^2) && (6.49)\\
&= \left(-\frac{h_0^2}{1+h_0^2}, 0, \frac{h_0}{1+h_0^2}\right) + \left(0, -\frac{1}{(1+h_0^2)^{1/2}}\frac{d(b_0\phi_1)}{ds}, 0\right)\Gamma\\
&\quad + \Omega_{||,1}\mathbf{t}_0\Gamma + O(\Gamma^2). && (6.50)
\end{aligned}$$

The force balance (6.29) indicates that the resultant internal stress $\mathbf{N}$ is $O(\Gamma)$ to first approximation. Writing $\mathbf{N} = \mathbf{N}_1\Gamma + \mathbf{N}_2\Gamma^2 + O(\Gamma^3)$, the force balance at $O(\Gamma)$ is

$$\frac{dN_1}{ds} = -\beta b_0 \tag{6.51}$$

where $\mathbf{N}_1 = (0, N_1, 0)$. The general solution is

$$N_1 = \frac{\beta h_0 s^2}{2(1+h_0^2)^{1/2}} - \beta C_1 s + C_2. \tag{6.52}$$

The free end condition (6.34) requires $C_2 = 0$ whereas the tethered end condition (6.36) dictates that

$$C_1 = \frac{Q_1(1+R/L)+\beta/2}{Q_1+\beta}\frac{h_0}{(1+h_0)^{1/2}} = K\frac{h_0}{(1+h_0)^{1/2}}. \tag{6.53}$$

The moment balance (6.30) at $O(\Gamma)$ is

$$Cm\,(\mathbf{t}_0\cdot\mathbf{H})\,\mathbf{t}_1\times\mathbf{H} + \mathbf{t_0}\times\mathbf{N}_1 + \mathbf{t}_0\times\frac{d^2\mathbf{t}_1}{ds^2} + (K_t/K_b)\mathbf{t}_0\frac{d^2\Psi_1}{ds^2} = \mathbf{0}. \tag{6.54}$$

This expression yields the three independent equations

$$\begin{aligned} \frac{d^3 b_1}{ds^3} - \sigma^2\frac{db_1}{ds} &= 0 && (6.55)\\ \frac{d^3(b_0\phi_1)}{ds^3} - \sigma^2\frac{d(b_0\phi_1)}{ds} &= N_1 && (6.56)\\ \frac{d^2\Psi_1}{ds^2} &= 0 && (6.57) \end{aligned}$$

where $\sigma^2 = (1+h_0^2)Cm$. The third equation and the free end moment boundary condition (6.35) imply that there is no $O(\Gamma)$ twisting, or $d\Psi_1/ds = 0$. The general solutions to the remaining two equations are

$$\begin{aligned} \frac{db_1}{ds} &= A_1\cosh\sigma s + B_1\sinh\sigma s && (6.58)\\ \frac{d(b_0\phi_1)}{ds} &= A_2\cosh\sigma s + B_2\sinh\sigma s - \frac{N_1}{\sigma^2} - \frac{\beta h_0}{\sigma^4(1+h_0^2)^{1/2}}. && (6.59) \end{aligned}$$

The $O(\Gamma)$ boundary conditions at the free end $s = 0$ are

$$\begin{aligned} \frac{d^2 b_1}{ds^2} &= 0 && (6.60)\\ \frac{d^2(b_0\phi_1)}{ds^2} &= 0. && (6.61) \end{aligned}$$

while at the tethered end $s = 1$ they are

$$\frac{d^2 b_1}{ds^2} = 0 \tag{6.62}$$

$$\frac{d^2(b_0\phi_1)}{ds^2} + \frac{R}{L}N_1 = Q_2\frac{h_0}{(1+h_0^2)^{1/2}}. \tag{6.63}$$

Therefore, one deduces that $A_1 = B_1 = 0$, and $db_1/ds = 0$. We also have

$$B_2 = -\frac{\beta}{\sigma^3}\frac{h_0}{(1+h_0^2)^{1/2}}K \tag{6.64}$$

$$A_2 = \frac{\beta}{\sinh\sigma}\frac{h_0}{(1+h_0^2)^{1/2}}\left[K\left(\frac{\cosh\sigma}{\sigma^2} - \frac{1}{\sigma^2} + \frac{R}{L}\right) + \frac{1}{\sigma^2} - \frac{1}{2}\frac{R}{L} + \frac{Q_2}{\beta}\right] \tag{6.65}$$

Before proceeding we introduce

$$F(s) = \frac{d(b_0\phi_1)}{ds} \tag{6.66}$$

$$G(s) = \int_s F(s')ds' \tag{6.67}$$

$$H(s) = \int_s G(s')ds' \tag{6.68}$$

so $b_0\phi_1 = G(s) + C_3$. Specifically, these functions are

$$F(s) = A_2\cosh\sigma s + B_2\sinh\sigma s - \frac{N_1}{\sigma^2} - \frac{\beta h_0}{\sigma^4(1+h_0^2)^{1/2}} \tag{6.69}$$

$$\begin{aligned} G(s) = {} & \frac{A_2}{\sigma}\sinh\sigma s + \frac{B_2}{\sigma}\cosh\sigma s - \frac{1}{\sigma^2}\left(\frac{\beta h_0 s^3}{6\left(1+h_0^2\right)^{1/2}} - K\frac{\beta h_0 s^2}{2(1+h_0^2)^{1/2}}\right) \\ & -\frac{1}{\sigma^4}\left(\frac{\beta h_0 s}{(1+h_0^2)^{1/2}}\right) \end{aligned} \tag{6.70}$$

$$\begin{aligned} H(s) = {} & \frac{A_2}{\sigma^2}\cosh\sigma s + \frac{B_2}{\sigma^2}\sinh\sigma s - \frac{1}{\sigma^2}\left(\frac{\beta h_0 s^4}{24\left(1+h_0^2\right)^{1/2}} - K\frac{\beta h_0 s^3}{6(1+h_0^2)^{1/2}}\right) \\ & -\frac{1}{\sigma^4}\left(\frac{\beta h_0 s^2}{2(1+h_0^2)^{1/2}}\right). \end{aligned} \tag{6.71}$$

The force balance at $O(\Gamma^2)$ is

$$\frac{d\mathbf{N}_2}{ds} = (1-\beta)\mathbf{t}_0\left(\mathbf{t}_1\cdot\mathbf{v}_0 + \mathbf{t}_0\cdot\mathbf{v}_1\right) + \beta\mathbf{v}_1 \tag{6.72}$$

which may be written as

$$\frac{d\mathbf{N}_2}{ds} = (1-\beta)\mathbf{t}_0\left(\frac{d(b_0(G(s)+C_3))}{ds} + 2\frac{h_0}{(1+h_0^2)^{1/2}}(G(s)+C_3) - \frac{1}{(1+h_0)^{1/2}}\bar{U}\right) + \beta\mathbf{v}_1. \tag{6.73}$$

The following expressions for $\mathbf{N}_2 = (N_{2x}, 0, N_{2z})$ are obtained by integrating the above equation and applying the free end boundary conditions $N_{2x} = N_{2z} = 0$. We have

$$\begin{aligned} N_{2x} &= -\bar{U}s\left(\beta + \frac{1-\beta}{1+h_0^2}\right) + C_3\frac{h_0(1-\beta)s}{1+h_0^2} \\ &\quad + \frac{1-\beta}{(1+h_0^2)^{1/2}}\left(b_0(s)G(s) - b(0)G(0) + 2\frac{h_0}{(1+h_0^2)^{1/2}}(H(s)-H(0))\right) & (6.74) \\ N_{2z} &= -\bar{U}s\frac{(1-\beta)h_0}{1+h_0^2} + C_3\left(\frac{h_0^2(1-\beta)s}{1+h_0^2} + \beta s\right) + \beta(H(s)-H(0)) \\ &\quad + \frac{h_0(1-\beta)}{(1+h_0^2)^{1/2}}\left(b_0(s)G(s) - b(0)G(0) + 2\frac{h_0}{(1+h_0^2)^{1/2}}(H(s)-H(0))\right). & (6.75) \end{aligned}$$

To determine C_3 and $\bar{U}$, we apply the boundary conditions at the tethered end

$$\begin{aligned} N_{2x}(1) &= Q_1\bar{U} & (6.76) \\ N_{2z}(1) &= -Q_1\left(G(1) + C_3 + F(1)\frac{R}{L}\right). & (6.77) \end{aligned}$$

We then arrive at the expression for the scaled swimming speed

$$\begin{aligned} U &= \bar{U}\Gamma + O(\Gamma^2) = \frac{h_0(\beta-1)}{(Q_1+1)(Q_1+n)(1+h_0^2)}\Big(Q_1\frac{R}{L}(F(1) - (G(1)-G(0)) \\ &\quad + (2Q_1+\beta)(\frac{1}{2}(G(1)+G(0)) - (H(1)-H(0)))\Big)\Gamma + O(\Gamma^2). & (6.78) \end{aligned}$$

In Figure 6.5, the swimming speed given by (6.78) along with the corresponding swimming speeds obtained from the simulations are plotted. In the plots, we include simulation results where the hydrodynamic interactions were truncated after the force monopole term (FCM-M) along with those including both monopoles and dipoles (FCM-MD). In both the asymptotic results and the simulations we observe that at low Sp the scaled swimming speed U varies as Sp^4. The asymptotic prediction corresponds with the FCM-M results. This observation is attributed to the resistive force approximation being the drag associated with a line of Stokeslets. The differences in the simulation data for FCM-M and FCM-MD show the corrections from the higher-order hydrodynamic effects. In addition, the agreement between the simulations and the asymptotic solution improve as Mn increases as the asymptotic analysis assumes that $\Gamma/Cm << 1$.

With the expression (6.78), we may examine how the parameters governing the magnetic forces Cm, h_0 and the geometric parameter R/L affect low Sp swimming.

6.4.1 Magnetic forces

Figure 6.6(a) shows the coefficient in (6.78) for the scaled swimming speed, $\bar{U}$, as a function of the parameter Cm governing the relative strength of the magnetic forces. The relative amplitude of the transverse magnetic field, h_0, is set equal to 1.0. The swimming speed monotonically decreases with Cm. When $Cm = 0$, which corresponds to the absence of an applied magnetic field, the swimming speed is finite and has the value

$$\begin{aligned}\bar{U} &= \frac{\beta(\beta-1)h_0^2}{(Q_1+1)(Q_1+\beta)^2(1+h_0^2)^{3/2}}\Big[\left(Q_1+\frac{\beta}{2}\right)\frac{Q_1}{120}+\frac{R}{L}\frac{Q_1}{36}\left(\frac{28}{10}Q_1+\beta\right) \\ &\quad +\left(\frac{R}{L}\right)^2\frac{Q_1}{24}(7Q_1+\beta)+\left(\frac{R}{L}\right)^3\frac{Q_1^2}{3} \\ &\quad +\frac{Q_2}{\beta}(Q_1+\beta)\left(\frac{Q_1}{12}+\frac{Q_1}{3}\frac{R}{L}+\frac{\beta}{24}\right)\Big]. \end{aligned} \tag{6.79}$$

This result may seem alarming, but in expanding the solution it was assumed that $\Gamma/Cm << 1$, and therefore as $Cm \to 0$ the range of Γ over which (6.78) is valid becomes vanishingly small ([107]).

As Cm increases, the swimming speed decreases as a result of the increased magnetic torque keeping the filament aligned with the field's direction. In the limit $Cm \to \infty$,

$$\begin{aligned}\bar{U} &\to \frac{\beta(\beta-1)h_0^2}{Cm^{1/2}(Q_1+1)(Q_1+\beta)^2(1+h_0^2)^2}Q_1\frac{R}{L}\Big[Q_1\frac{R}{L}\left(\frac{1}{2}+\frac{R}{L}\right) \\ &\quad +\frac{Q_2}{\beta}(Q_1+\beta)\Big] \end{aligned} \tag{6.80}$$

so, $U \sim Mn^{-1/2}$. In Figure 6.6(b) the value of $\bar{U}$ is plotted as a function of Cm as given by (6.78) along with the value at $Cm = 0$ and the asymptotic value $Cm \to \infty$.

As the relative amplitude of the transverse magnetic field, h_0, increases, the swimming speed will increase to a peak value that occurs at $h_0 \approx 1$ and subsequently decays as $h_0 \to \infty$ (Figure 6.7(a)). The limit $h_0 \to 0$ corresponds to the magnitude of the transverse field approaching zero. In this limit the swimmer will remain aligned with the x-axis, so

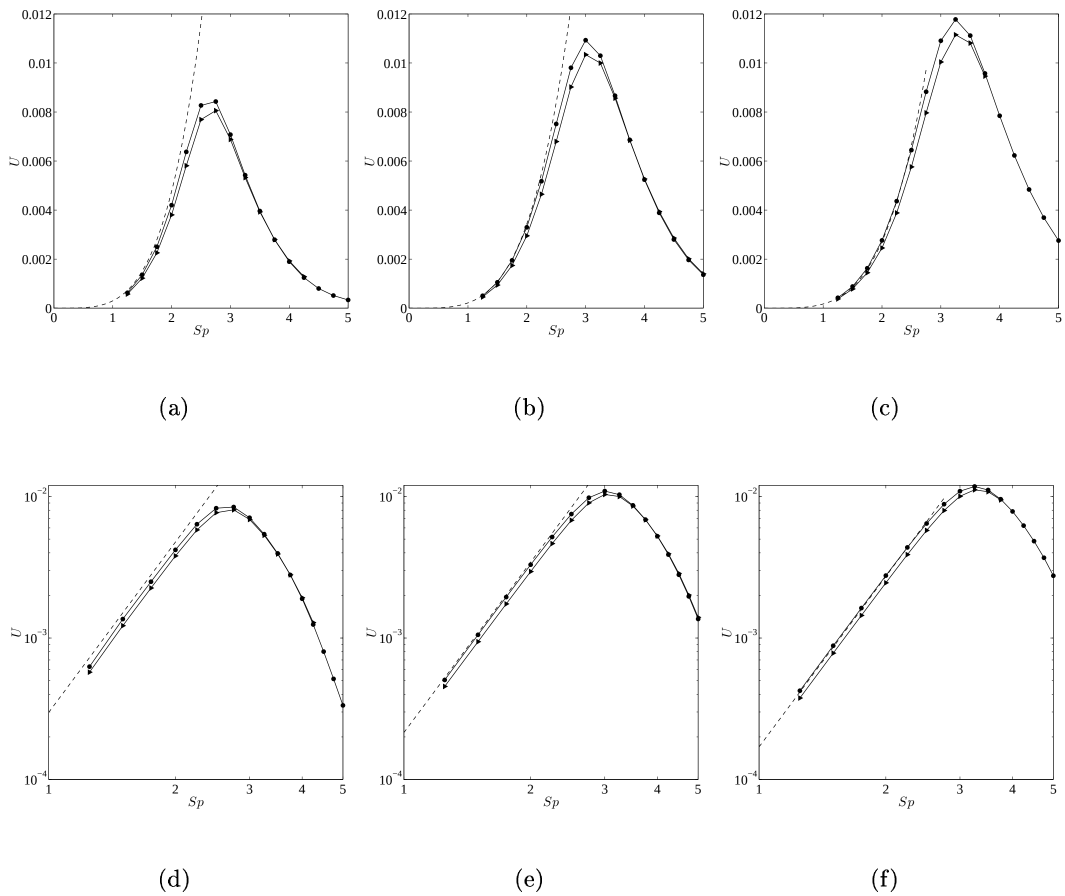

Figure 6.5: Scaled swimming speeds at low Sp for various Mn. The data are plotted in both linear-linear and log-log scales. The solid lines with the circular markers correspond to the FCM-M simulations FCM-monopole and the solid lines with the triangular markers are the FCM-MD simulations. The dashed line is the scaled swimming speed given by (6.78). In (a) and (d) $Mn = 5$ ($Cm = 4.057$) (b) and (e) $Mn = 10$ ($Cm = 8.115$), and (c) and (f) $Mn = 15$ ($Cm = 12.172$).

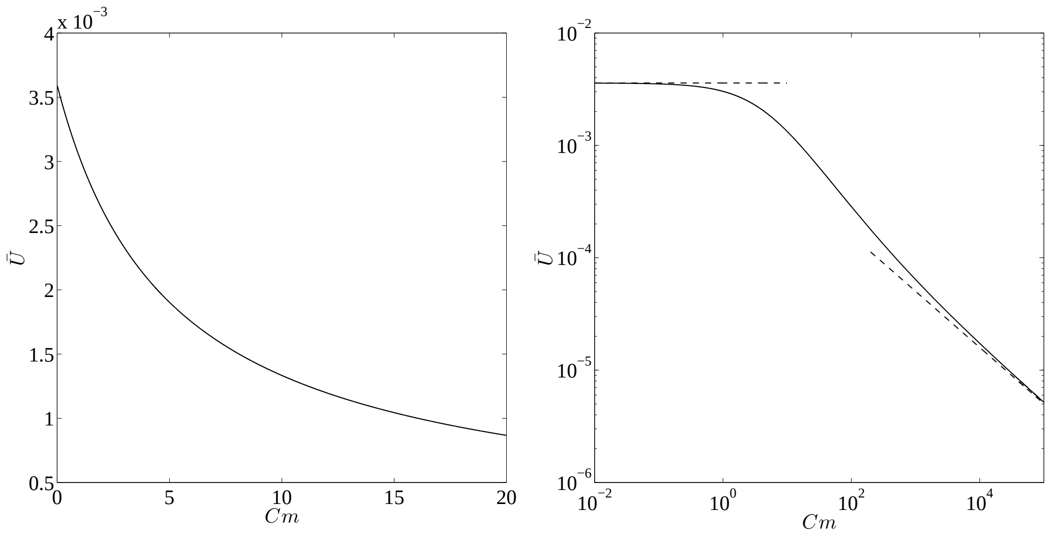

(a) (b)

Figure 6.6: (a) $\bar{U}$ as a function of Cm given by (6.78) (b) Log-log plot of $\bar{U}$ vs. Cm (solid line) including the value at $Cm = 0$ (6.79) and the asymptotic values as $Cm \to \infty$ (6.80) (dashed lines). In (a) and (b) $R/L = 0.183$ and $h_0 = 1.0$.

$b(s)$, and consequently U will vanish. Since $\sigma \to \sqrt{Cm}$, the values of the functions listed in Appendix 6.5 all scale linearly in h_0. Therefore, from (6.78), we have $\bar{U} \sim h_0^2$.

At the other extreme, when $h_0 \to \infty$, the transverse field is much greater in magnitude than the constant field. In fact, the magnitude of the total field becomes unbounded. Therefore, in this limit, the swimmer will remain closely aligned with the applied field and rotate as a rigid body. Also, since the applied field is essentially localized to the yz-plane, $d\alpha/ds$ will be zero. For these reasons, a significant swimming speed in not expected at this limit either. To obtain the asymptotic expression, we recognize $\sigma \to h_0\sqrt{Cm}$ and as a result

$$\bar{U} \to \frac{\beta(\beta-1))}{(Q_1+1)(Q_1+n)h_0^2\sqrt{Cm}} Q_1 \frac{R}{L}\left(K\frac{R}{L} - \frac{1}{2}\frac{R}{L}\frac{Q_2}{\beta}\right) \tag{6.81}$$

This leading order term is from $F(1)$ in (6.78), which is associated with the force balance boundary condition term $\mathbf{\Omega} \times R\mathbf{t}$ in (6.10). In Figure 6.7(b) we plot $\bar{U}$ as a function of h_0 along with the asymptotic values. The $h_0 \to 0$ asymptotic value was calculated by using $\sigma = \sqrt{Cm}$.

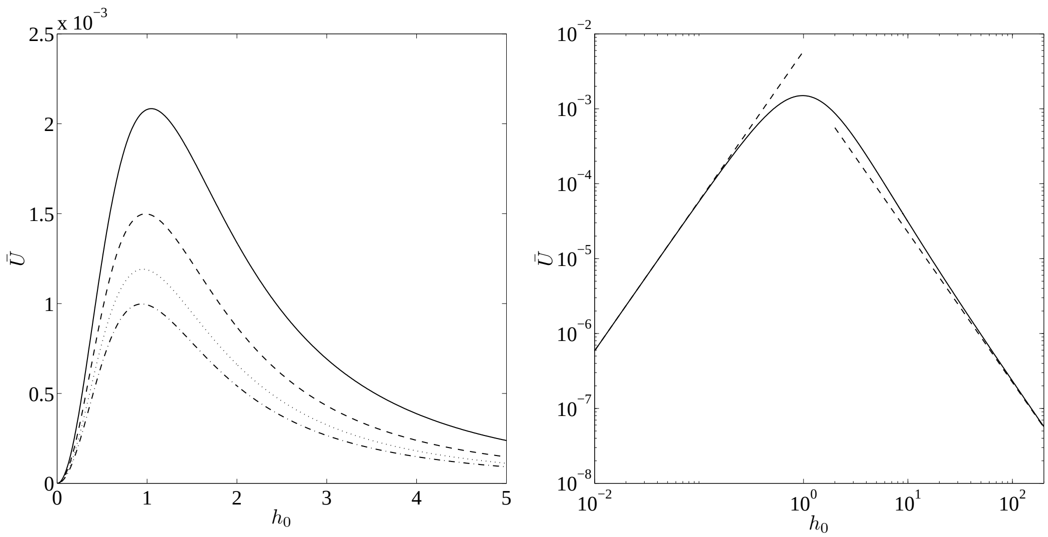

(a) (b)

Figure 6.7: (a) $\bar{U}$ as a function of h_0 for $Mn = 5$ ($Cm = 4.057$) (solid line), $Mn = 10$ ($Cm = 8.115$) (dashed line), $Mn = 15$ ($Cm = 12.172$) (dotted line), and $Mn = 20$ ($Cm = 16.23$) (dash-dotted line) with $R/L = 0.183$. (b) Log-log plot of $\bar{U}$ (solid line) and the asymptotic values for $h_0 \to 0$ and $h_0 \to \infty$ (6.81) (dashed lines) with $Mn = 10$ and $R/L = 0.183$

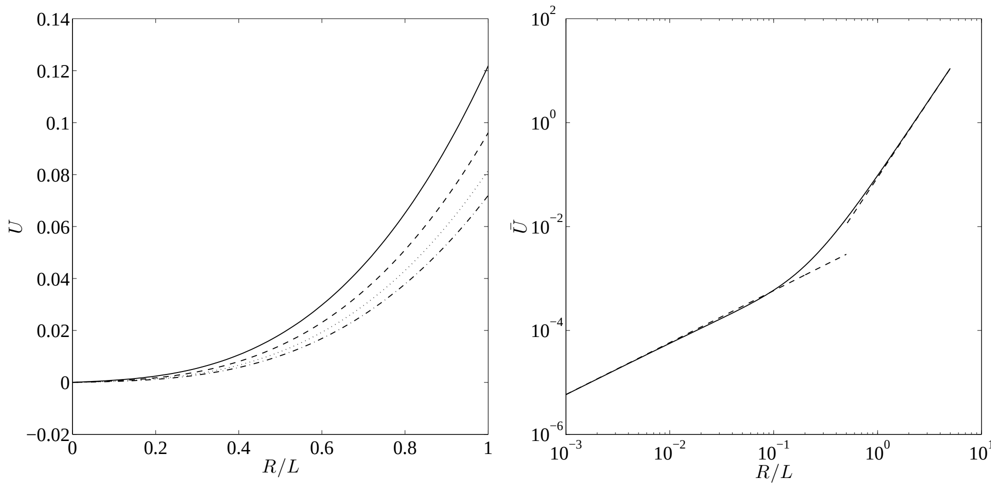

(a) (b)

Figure 6.8: (a) $\bar{U}$ as a function of R/L for $Mn = 5$ (solid line), $Mn = 10$ (dashed line), $Mn = 15$ (dotted line), and $Mn = 20$ (dash-dotted line) with $h_0 = 1.0$. (b)Log-log plot of $\bar{U}$ (solid line) and the asymptotic values for $R/L \to 0$ (6.83) and $R/L \to \infty$ (6.85) (dashed lines) with $Mn = 10$ and $h_0 = 1$.

6.4.2 Swimmer geometry

The low Sp swimming speed increases monotonically with R/L. In this case, the validity of the calculation is limited to situations where R/L does not exceed $R/L \sim O(1)$. Within this range, the calculation indicates that the larger cargo size increases the deformation of the filament which, in turn, produces higher swimming speeds. At large R/L however, the drag becomes excessive and should cause the swimming speed to decrease. This effect is not captured by this calculation. When $R/L = 0$ swimming is not expected since, in the absence of the sphere, the magnetic filament considered here is a symmetric body. This is recovered by the asymptotic solution. In a more general setting, however, variations in the magnetic susceptibility, χ, or in the elastic properties of the links ([107]) along the filament can produce the asymmetry in the bending wave necessary to generate a net translation in the absence of any cargo.

In the limit of $R/L \to 0$,

$$K \to \frac{1}{2} + \frac{Q_1}{2\beta} \tag{6.82}$$

and the coefficient $\bar{U}$ for the swimming speed takes the limit

$$\bar{U} \to \frac{(\beta-1))h_0^2}{(1+h_0)^{3/2}} \frac{Q_1}{2} \left(\frac{1}{12\sigma^2} - \frac{1}{\sigma^4} + \frac{2}{\sigma^5} \frac{\cosh\sigma - 1}{\sinh\sigma} \right). \tag{6.83}$$

Therefore, $\bar{U} \sim R/L$. On the other hand, as $R/L \to \infty$,

$$K \to \frac{R}{L}. \tag{6.84}$$

With this value for K the limiting value for $\bar{U}$ is

$$\bar{U} \to \frac{(\beta-1)h_0^2}{(1+h_0)^{3/2}} \frac{Q_2(R/L)}{Q_1} \left(\frac{\cosh\sigma}{\sigma\sinh\sigma} - \frac{1}{\sigma^2} \right), \tag{6.85}$$

and thus $\bar{U} \sim (R/L)^3$.

Figure 6.8(b) shows $\bar{U}$ as a function of R/L along with the asymptotic values presented above. We see that at $R/L \approx 0.1$, the dependence begins to transition from linear to cubic. When R/L is small, the sphere's translational drag is greater than its rotational drag. Therefore, the deformation of the filament that leads to swimming is a result of the asymmetry caused by the translation of the sphere. However, once R/L becomes large enough, the rotational drag will be larger than the translational drag, and, accordingly, the dependence of deformation associated with swimming will be $\sim (R/L)^3$.

6.5 Expression in the Swimming Speed

In the expression derived for the $O(\Gamma)$ swimming speed appear the values of the functions $F(s)$, $G(s)$, and, $H(s)$ at the free and tethered ends. The values of these functions are

$$\begin{aligned}
F(1) &= \frac{\beta h_0}{(1+h_0^2)^{1/2}}\Big[\frac{1-\cosh\sigma}{\sigma^3\sinh\sigma}K + \frac{\cosh\sigma}{\sigma\sinh\sigma}\left(K\frac{R}{L} - \frac{1}{2}\frac{R}{L} + \frac{Q_2}{\beta}\right) \\
&\quad -\frac{1}{\sigma^2}\left(\frac{1}{2} - K\right) + \frac{1}{\sigma^2}\left(\frac{\cosh\sigma}{\sigma\sinh\sigma} - \frac{1}{\sigma^2}\right)\Big] \qquad (6.86)\\
H(1) - H(0) &= \frac{\beta h_0}{(1+h_0^2)^{1/2}}\Big[\frac{\cosh\sigma - 1}{\sigma^3\sinh\sigma}\left(K\frac{R}{L} - 2\frac{K}{\sigma^2} + \frac{1}{\sigma^2} - \frac{1}{2}\frac{R}{L} + \frac{Q_2}{\beta}\right) \\
&\quad -\frac{1}{\sigma^2}\left(\frac{1}{24} - \frac{K}{6}\right) - \frac{1}{2\sigma^4}\Big] \qquad (6.87)\\
G(1) &= \frac{\beta h_0}{\sigma^2(1+h_0^2)^{1/2}}\left[K\left(\frac{R}{L} - \frac{1}{\sigma^2} + \frac{1}{2}\right) - \frac{1}{2}\frac{R}{L} - \frac{1}{6} + \frac{Q_2}{\beta}\right] \qquad (6.88)\\
G(0) &= -\frac{\beta h_0}{\sigma^4(1+h_0^2)^{1/2}}K. \qquad (6.89)
\end{aligned}$$

6.6 Summary and Conclusions

A fully three-dimensional simulation scheme has been presented that describes the dynamics of a chain of discrete paramagnetic beads bonded together by short flexible links to form a tail attached to a larger spherical particle or head. The scheme captures in detail the effects of magnetic, fluid and elastic forces within the filament. It has been demonstrated that the magnetic micro-swimmer introduced by [33] with planar actuation can be used as a model to study a corkscrew form of swimming, driven by a rotating magnetic field. In a rotating field, the swimmer will deform into a spiral shape that rotates about an axis in the direction of swimming. The kinematics of the motion were extracted and parameterized by time independent functions describing the pitch, the distance from the axis of symmetry and the phase shift along the length of the tail. Further, the correspondence between this parameterization and the observed swimming velocity was established.

An approximate description of the motion was provided by a resistive force model in which the filament tail is treated as a continuous elastica subject to a distributed magnetic torque per unit length. An asymptotic analysis for low frequency rotations predicted that the swimming speed grows initially as $U \sim Sp^4$. The refinements to the resistive force model described in §6.3 were essential in order to match the simulation results. Once this was done, there was a good correspondence between the two for the swimming at low frequency. The asymptotic analysis further identified broadly the effects of varying the other parameters governing the magnetic field and the geometry.

At this time of writing, there has been no experimental demonstration of spiral swimming of an artificial micro-swimmer. The present results though indicate that such a motion is possible, and effective. Additionally, it opens the question as to what other applied fields might be devised to generate more complex dynamics exhibited by microorganisms. For example, as the artificial swimmer will move in the direction of the constant component of the applied field, the direction of this field can be changed over time to yield a helical swimming path similar to that of sea urchin sperm during chemotaxis [40]. The manipulation and propulsion of artificial micro-swimmers with unsteady magnetic fields provides insights into the more general questions regarding swimming micro-organisms. Naturally occurring spiral swimmers such as bacteria are both force-free and torque-free, with the torque exerted by a rotating flagellum counter-balanced by the viscous torque of the counter-rotating head. The magnetic swimmer is force-free but subject to a net torque from the external field. The magnetic tail though deforms in response to elastic and fluid forces and thus demonstrates the response that may be characteristic of more general systems. In particular, artificial swimmers may be used to explore the complexities of swimmer-swimmer interactions and of swimming organisms near a bounding surface or in the presence of an ambient shear flow. The discrete particle description of the simulations lends itself to these situations where resistive force models may be inaccurate or too complex to analyze.

Chapter 7

The interactions between co-moving magnetic micro-swimmers

7.1 Introduction

From self-organized vortices of 2D-confined sea urchin sperm [106] to millimeter long trains of wood mouse sperm [96] to turbulence-like structures formed by swarming bacteria [30], the interactions between swimming micro-organisms have been observed to lead to a rich variety of collective behaviors. Recent coarse-grained hydrodynamics studies [112] and simulations of rigidly connected point sources [54] and self-locomoting rods [110] lend insight into the instabilities observed in [30]. Additionally, these studies along with [57] established the differences between suspensions of 'pusher'-type swimmers where the thrust is generated behind the passive element of the swimmer and 'puller'-type swimmers where the thrust is in front of the passive component. As two swimmers approach each other, details concerning the swimmers' kinematics and the near-field hydrodynamic interactions become important [56] and need to be accounted for. Quantifying experimentally the relationship between these dynamics and suspension properties is, in general, quite difficult. The artificial micro-swimmer [33] offers a controllable model system that may be used in place of microorganisms to provide insight into this relationship. In this case, the differences need to be quantified between this externally driven system and the self-driven swimmer which it mimics.

In this chapter, we now use the particle based representation to examine the interactions between two micro-swimmers in co-moving configurations. Studying the interactions of artificial micro-swimmers theoretically provides an example of swimmer-swimmer interactions where the details concerning the driving forces and constitutive laws are well described and differs from studies where the kinematics, rather than the driving forces, of the swimmers are prescribed [113, 104, 36]. Additionally, the results presented here allow for the evaluation of the accuracy of theoretical models where the details concerning swimmer propulsion are ignored [57, 112, 54, 110]. Interactions of swimmers executing both flagellum beating and rotating corkscrew strategies are considered. The details concerning the nature of the interactions, including the role of the inter-swimmer magnetic and far-field hydrodynamic forces, are provided. From these may results and comparisons with the recent boundary element simulations of a pair of interacting bacteria [56], we may quantify the effectiveness of an externally driven system as a model for an internally driven swimming microorganism.

7.2 Swimmer-swimmer interactions

The interactions between two co-moving artificial micro-swimmers are examined. We consider four cases where the swimmers are driven by both fields, (5.1) and (6.1), and in two different configurations. For each configuration, the swimming speed is computed over a range of separations. In the cases considered, $M_n = 10$, $S_p = 3.0$ and $h_0 = 1.0$ are fixed and swimming is in the negative x-direction. $N = 15$ beads comprise the each swimmer's filament tail giving a length $L = 32.8a$. The radius of the tethered sphere is $R = 6.0a$, and therefore $R/L = 0.183$. The remaining parameters are identical to those employed in the single swimmer studies presented in the previous two chapters.

7.2.1 Side-by-side configuration

In the first case the separation vector is $\mathbf{r} = (0, 0, h)$ and the motion is driven by the planar applied field (5.1). Here the axis of separation and direction of applied magnetic torque are aligned. The motion of the swimmer's tails are synchronized by the applied field. Both swimmers have the same scaled swimming speed which is at most 3% less than the single swimmer scaled speed, $U_\infty = 0.006355$. In addition to the motion in the swimming direction, the swimmers move apart from each other along the axis of separation

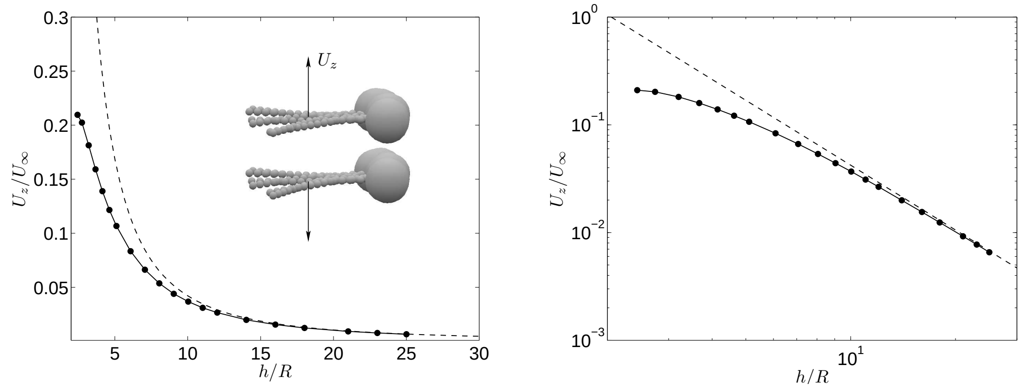

(a) (b)

Figure 7.1: (a) Swimming speed as a function of separation distance for stacked swimmers driven by the applied field (5.1). (b) The repulsion velocity with the dashed line provided by (7.1). The inset shows the motion of the two swimmers over one period of the applied field. (b) Log-log plot of the repulsion velocity over a range of separation distances. The dashed lines is provided by (7.1) and decays as h^{-2}.

(Figures 7.1(a) and 7.1(b)). The scaled repulsion speed, U_z attains a maximum value of $U_z \approx 0.21 U_\infty$ near-contact, and decays with separation. The motions of the swimmers' tails are synchronized by the applied field and are nearly identical to the beat patterns of tails of two consecutive planar swimmers considered later on in more detail (Figure 7.5).

To analyze the far-field interactions attained when the separation distance is much greater than the length of the swimmer, $h \gg 2R+L+l$, we consider the flow field generated by a low order expansion of the body force distribution associated with an isolated swimmer about the position of the tethered sphere, $\mathbf{Y}_{N+1}$ (See Appendix A). As all the interbead forces are equal and opposite, the total force $\sum_{n=1}^{N+1}(\mathbf{F}^n_{mag}+\mathbf{F}^n_{elas})=0$, but the symmetric, $G^S_{ij}(t)$, and antisymmetric, $G^A_{ij}(t)$, parts of the force dipole $G^T_{ij}(t)$ take non-zero values. Taking $\mathbf{x}-\mathbf{Y}_{N+1}=(0,0,h)$, the resulting time averaged out of plane flow according to (7.8) is

$$v_z(h) = -\frac{3\left\langle G^S_{33}\right\rangle}{8\pi\eta h^2} \tag{7.1}$$

where $\left\langle G^S_{33}\right\rangle$ is the non-zero time average value of G^S_{33}. The dashed lines in Figures 7.1(a) and 7.1(b) are provided by (7.1). At separations $h \geq 1.5(2R+L+l)$, the repulsion speed produced by the simulations does indeed correspond to the far-field disturbance flow pro-

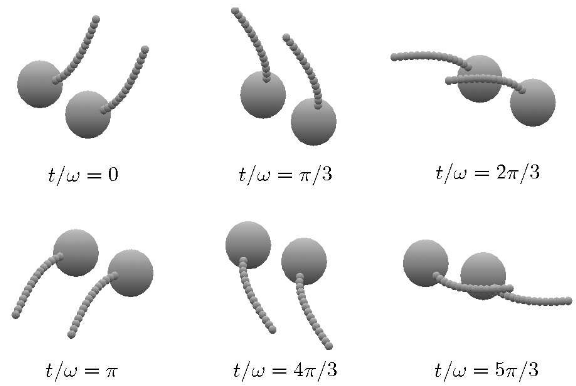

Figure 7.2: An end-on view of the motion of two side-by-side spiraling swimmers over one period of the applied field. The motion of the tails are coupled by the applied field that is rotating counter clockwise.

duced by the force dipole associated with a single swimmer. This repulsion is a result of the incompressibility of the fluid. Over the course of one period, the motion of the swimmer in the xy-plane entrains fluid along the x- and y-axes which is then forced out along the z-axis. The reduction in swimming speed cannot be explained by this analysis as $v_x = 0$ since $G^A_{13} = 0$ and $x_1 - Y_{N+1,1} = 0$.

Along with planar swimmers, the interactions of two swimmers driven by the field (6.1) are considered. The motion of the swimmers over the course of one period is shown in Figure 7.2. As before, the separation vector is $\mathbf{r} = (0, 0, h)$ but this vector is now perpendicular to the direction of applied torque. Figure 7.3(a) shows the resulting scaled swimming speed for the spiral swimmers in this configuration. The values are normalized by the isolated value of $U_\infty = 0.01033$. Again, the two swimmers exhibit the same speed, which is, at any separation, less that the value of an isolated swimmer. As the swimmers come into contact there is an appreciable decrease in the swimming speed with a near contact value of $0.8U_\infty$. The swimmers additionally move apart with scaled repulsion speed $U_{||}$ and precess around each other with precession speed $U_\perp$ (Figure 7.3(b)). This data is shown again in Figure 7.4 in log-log scale.

We compare the present results to those of Ishikawa *et al.* [56] where the trajectories are determined using boundary element simulations for two model bacteria in the same

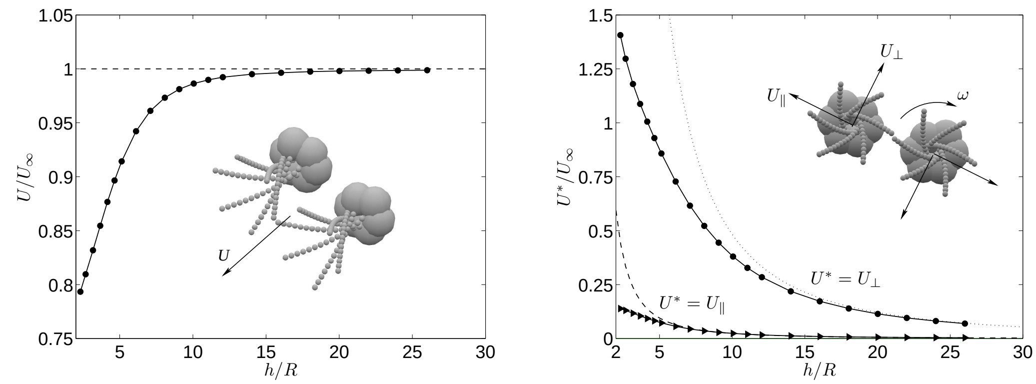

(a) (b)

Figure 7.3: (a) Swimming speed as a function of separation distance for side-by-side swimmers driven by the applied field (6.1). (b) Precession velocity, $U_{\perp}$, and repulsion velocity, $U_{||}$, versus separation distance. The dashed and dotted lines are provided by equations (7.2) and (7.3) respectively. The insets in the two figures show the motion of the two swimmers over one period of the applied field.

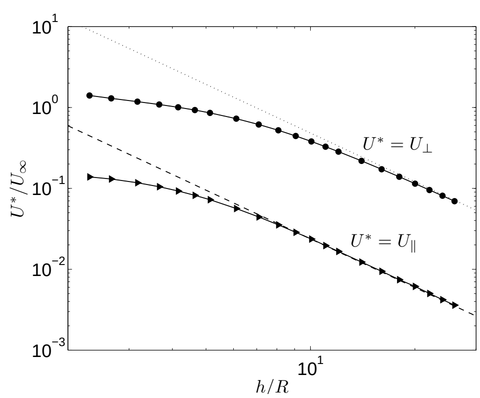

Figure 7.4: Log-log plot of the precession and repulsion velocities over a range of separation distances. The dashed is given by (7.2) and the dotted line by (7.2). Both decay like h^{-2}.

configuration considered here. Initially, as the bacteria swim they precess about each other and the inter-swimmer separation distance decreases. Over time, however, the bacteria change their swimming directions and swim away from each other. Here, we find that the spiraling artificial micro-swimmers exhibit precession but move apart as they swim. This difference in dynamics arises from the model bacteria being 'pushers' and the artificial swimmers being 'pullers.' The component of the stresslet related to the repulsion in the artificial swimmer case is the opposite sign of that in the bacterial case. Also unlike the bacteria, the artificial swimmers will not change their swimming direction since such a reorientation is not be permitted by the applied field.

As before, we may compute the effective force dipole G^T_{ij} for the spiral swimmer and analyze the far-field interactions. With these values of the components of the effective force dipole and (7.8) with $\mathbf{x} - \mathbf{Y}_{N+1} = (0, 0, h)$, the far-field flow can be determined. The disturbance flow related to the repulsion velocity is

$$v_{||}(h) = -\frac{3\left\langle G^S_{33}\right\rangle}{8\pi\eta h^2} \tag{7.2}$$

while the precession velocity is given by

$$v_{\perp}(h) = -\frac{2G^A_{23}}{8\pi\eta h^2}. \tag{7.3}$$

The values provided by these equations are shown as dashed and dotted lines in Figures 7.3(b) and 7.4 and match the simulation values at large separations. As with the planar swimmer, the far-field repulsion is produced the zz component of the stresslet. The precession is related to the flow generated by the constant external magnetic torque on each swimmer.

7.2.2 Consecutive configuration

The resulting swimming speeds for a configuration where the separation vector is $\mathbf{r} = (d, 0, 0)$ are presented. In this configuration, the swimmers are placed one behind the other. The motion over one period for planar swimmers in this configuration is shown in Figure 7.5. For both the planar (Figure 7.6(a)) and spiral swimmers, the speed of rear swimmer is greater than the isolated value, while the speed of the front swimmer is less. This effect is limited in the case of spiral actuation where the enhancement in speed of the rear swimmer

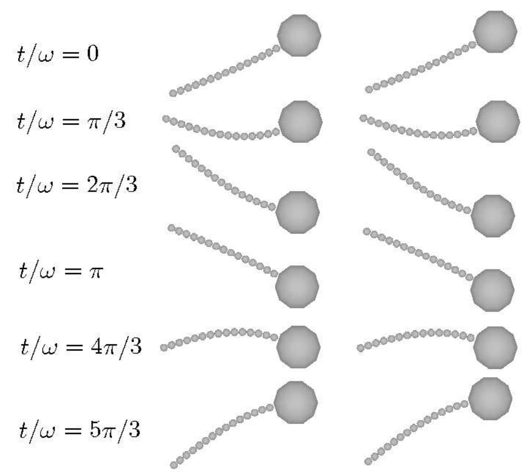

Figure 7.5: A top-view of the motion of two consecutive planar swimmers over one period of the applied field.

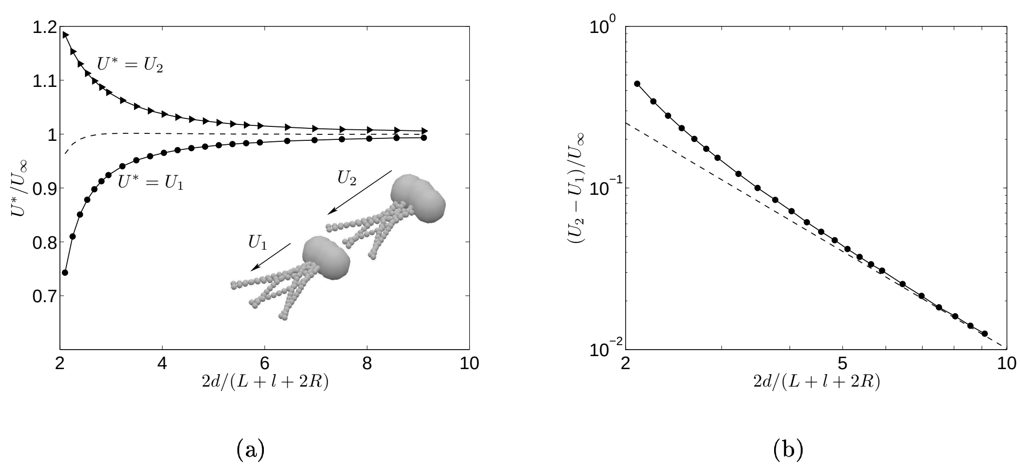

Figure 7.6: (a) Swimming speeds for two swimmers arranged consecutively and driven by applied field (5.1). (b) Log-log plot of the difference in swimming speeds with the dashed line being from 7.4 with the value of $\langle G_{11}^S \rangle$ for the planar swimmer.

and the reduction in speed of the front swimmer are at most 5% of the isolated value. For both types of swimmers, the average value of the two speeds for nearly all separations is the value in the isolated case. Figures 7.6(b) shows the difference in the swimming speeds as a function of separation distance for planar swimmers. From (7.8) and the components of G^T_{ij}, the far-field disturbance flow corresponding this interaction is

$$v(d) = -\frac{3\left\langle G^S_{11}\right\rangle}{8\pi\eta h^2}. \tag{7.4}$$

The differences in speeds are provided by twice the absolute value of (7.4) and are shown as the dashed lines in Figures 7.6(b). The far-field values are attained at separations of approximately two and a half swimmer lengths. Also, the symmetry of the interaction is evident as the far-field interaction illustrates $U_1(d) = U_\infty - |v(d)|/(L\omega)$ and $U_2(d) = U_\infty + |v(d)|/(L\omega)$.

7.2.3 Inter-Swimmer Magnetic Interactions

Along with the hydrodynamic interactions already discussed, inter-swimmer magnetic forces are present and affect the resulting dynamics. The magnetic interactions are akin to those that arise between self-assembled chains in suspensions of paramagnetic beads [42]. To quantify their effect, we conduct simulations where the inter-swimmer magnetic interactions are ignored. As the resulting motions are modified by hydrodynamic interactions alone, when compared to the motions from the full simulations the importance of the magnetic interactions can be ascertained. This comparison is done for planar swimmers in the stacked and consecutive configurations.

Figures 7.7(a) shows the repulsion velocity for the stacked configuration. The near-contact repulsion velocity, however, is clearly dependent upon the lateral magnetic interactions. As the separation increases, the magnetic interactions decay rapidly and the far-field hydrodynamics dominate the dynamics. The slight decrease in swimming speed found for planar swimmers in this configuration was not affected by the removal of the magnetic interactions. For swimmers in the consecutive configuration, the magnetic attraction between the filaments does enhance the speed of the rear swimmer while hindering that of the front swimmer. This enhancement, however, is modest, and the hydrodynamics appear to dominate, even at small separations.

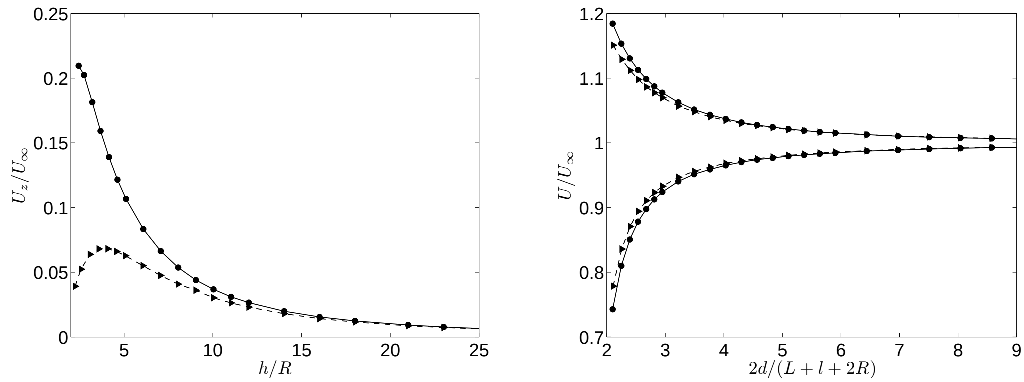

(a) (b)

Figure 7.7: (a) The repulsion velocity as a function of separation. (b) The two swimming speeds for consecutive planar swimmers. The solid line with the circular markers are from simulations where the magnetic interactions are included while the dashed line with the triangular markers corresponds to the simulations where the magnetic interactions are ignored.

7.3 Dipole Decomposition

To analyze the far-field interactions attained when the separation distance is much greater than the length of the swimmer, $h \gg 2R + L + l$, we consider the flow field generated by a low order expansion of the body force distribution associated with an isolated swimmer about the position of the tethered sphere, $\mathbf{Y}_{N+1}$,

$$\begin{aligned}\sum_{n=1}^{N+1} F_i^n \delta(\mathbf{x} - \mathbf{Y}_n) \\ + \sum_{n=1}^{N+1} G_{ij}^n \frac{\partial \delta(\mathbf{x}-\mathbf{Y}_n)}{\partial x_j} \quad &\approx \quad \left(\sum_{n=1}^{N+1} F_i^n\right) \delta(\mathbf{x} - \mathbf{Y}_{N+1}) \\ &+ \left(\sum_{n=1}^{N+1} G_{ij}^n + F_i^n (\mathbf{Y}_{N+1} - \mathbf{Y}_n)_j\right) \frac{\partial \delta(\mathbf{x}-\mathbf{Y}_{N+1})}{\partial x_j}. \end{aligned} \tag{7.5}$$

Since both the interbead magnetic and elastic forces are equal and opposite, the total force acting on the swimmer at any instant in time is zero, $\sum_{n=1}^{N+1} \mathbf{F}^n = \mathbf{0}$. The moments of the forces and the force dipoles, however, are non-zero, and provide the leading order contribution to the flow. Defining $G_{ij}^T = \sum_{n=1}^{N+1} G_{ij}^n + F_i^n(\mathbf{Y}_{N+1} - \mathbf{Y}_n)_j$, and decomposing

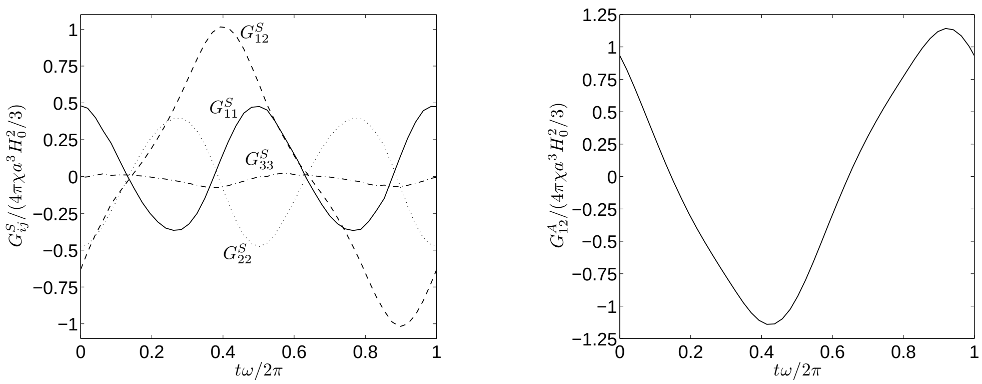

(a) (b)

Figure 7.8: Components of the force dipole of the planar swimmer: (a) The non-zero components of the traceless stresslet G^S_{ij} over the course of one period on the applied field. (b) The non-zero component of the anti-symmetric part of the force dipole, G^A_{12}.

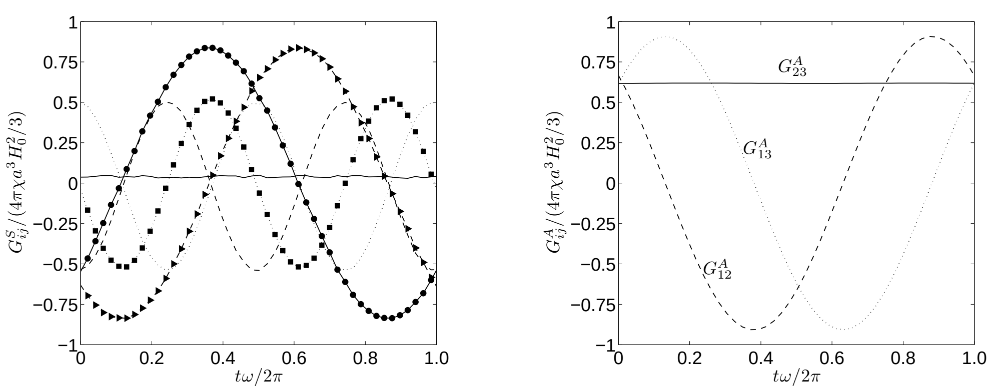

(a) (b)

Figure 7.9: Components of the force dipole of the spiral swimmer: (a) The non-zero components of the traceless stresslet G^S_{ij} over the course of one period on the applied field. The lines without the markers show to diagonal components with the solid line being G^S_{11}, the dashed line G^S_{22} and the dotted line G^S_{33}. The lines with the markers are the off diagonal components where the solid line with circular markers is G^S_{12}, the dashed line with triangular markers is G^S_{13} and the dotted line with the square markers is G^S_{23}. (b) The non-zero component of the anti-symmetric part of the force dipole, G^A_{12}, G^A_{13}, and G^A_{23}.

this tensor into its traceless, symmetric part (the stresslet)

$$G^S_{ij} = \frac{1}{2}(G^T_{ij} + G^T_{ji}) - \frac{1}{3}G^T_{kk}\delta_{ij} \tag{7.6}$$

and its antisymmetric part

$$G^A_{ij} = \frac{1}{2}(G^T_{ij} - G^T_{ji}), \tag{7.7}$$

the leading order flow field is, in index notation, given by

$$\begin{aligned} v_i(\mathbf{x} - \mathbf{Y}_{N+1}) \quad = \quad & \frac{1}{8\pi\eta}\Big(-2\frac{(\mathbf{x} - \mathbf{Y}_{N+1})_j}{r^3}G^A_{ij} \\ & -\frac{3(\mathbf{x} - \mathbf{Y}_{N+1})_i(\mathbf{x} - \mathbf{Y}_{N+1})_j(\mathbf{x} - \mathbf{Y}_{N+1})_k}{r^5}G^S_{jk}\Big) \end{aligned} \tag{7.8}$$

where $r = \sqrt{(\mathbf{x} - \mathbf{Y}_{N+1}) \cdot (\mathbf{x} - \mathbf{Y}_{N+1})}$. For the planar swimmer, the four non-zero components of the symmetric part over one period are shown in Figure 7.8(a) and the non-zero component of the antisymmetric part is presented in Figure 7.8(a). Figure 7.9(a) shows the components of G^S_{ij} and Figure 7.9(b) shows the components of G^A_{ij} for the spiral case. Here, the constant value G^A_{23} indicates the time-independent torque on the swimmer produced by the applied field.

7.4 Summary and Conclusions

In this study, a particle based method was used to conduct simulations of the artificial micro-swimmer. This particle based method treated the magnetic swimmer as a series of rigid spheres connected by inextensible flexible rods. The magnetic forces were treated using a point dipole approach, and the interbead hydrodynamic interactions were provided by FCM. First, simulations of a single swimmer were conducted. The resulting swimming speeds were consistent with previous simulations and compared favorably with the experiments at high S_p. The effects of a nearby surface need to be included in order to match the low S_p experimental results. Simulations of two co-moving artificial swimmers are performed. Cases are considered where the swimmers are driven by both planar and rotary fields in two different configurations. For the values of M_n, S_p and h_0 used in these simulations, the resulting scaled swimming speed for a single swimmer was $U = 0.006355$ for planar actuation and $U = 0.01033$ for spiral actuation. These values fall within the range of scaled swimming speeds of micro-organisms which, for example, are $U = 0.0033$ for *E. Coli* bacteria [22], $U = 0.012$ for bull sperm and $U = 0.0253$ for sea urchin sperm [17]. For the side-by-side, or stacked configurations, the swimming speed is the same for each swimmer and less than the value for an isolated swimmer. The reduction in speed is greater for the spiral type swimmers. In addition to motion in the swimming direction, the swimmers move apart from each other and the spiral swimmers also precess around each other. At large separations, the interactions decay like h^{-2} according to the far-field disturbance flow produced by a swimmer. Consecutive swimmers move only in the swimming direction, but the rear swimmer moves faster, while the front swimmer is slower. Again the interaction at large separations is provided by the force dipole associated with the swimmers. To understand the role of the magnetic interactions, simulations were conducted where the inter-swimmer magnetic forces were not included. By comparing these results to those from the full simulations, it is found that only the near-field repulsion for stacked swimmers is significantly effected by the magnetic forces.

Although the dynamics and interactions of this novel device are of interest in their own right, the results indicate that the interactions between the externally driven artificial micro-swimmer resemble the interactions between swimming microorgansims. For example, since the magnetic field exerts no net force on a swimmer the far-field hydrodynamic interactions decay as h^{-2} which is what one expects between two force-free and torque-free self-driven swimmers. Based on the results presented here, it is therefore reasonable to assume that at greater than separations of around two swimmer lengths, the far-field hydrodynamics will also provide a good approximation of the hydrodynamic interactions between microorganisms. Additionally, these results encourages understanding of how the artificial swimmer behaves near rigid surface and relates to the motion of microorganisms near surfaces [77]. By comparing with simulations of model bacteria [56], we see that suspensions of artificial micro-swimmers will not exhibit reorientation or dramatic changes in wave motion as a result of the hydrodynamic interactions. These limitations restrict the possibility of studying more generally phenomena such as the bacterial turbulence [30], or the formation of sperm vortices [106] with artificial swimmers.

Chapter 8

The behavior of an artificial swimmer near a rigid surface

8.1 Introduction

The presence of a surface will both increase the hydrodynamic drag experienced by a nearby particle and couple the particle's translational and rotational motions [50, 65]. These changes in the hydrodynamic response affect the behavior of swimming micro-organisms and modify both swimming speed and direction. For example, *E. Coli* bacteria that propel themselves by rotating their corkscrew-shaped flagellar bundles will adopt a circular swimming path as they approach a surface [77, 7] and as a result, the axial diffusion of *E. Coli* in circular pipes is found not to grow monotonically with the tube diameter [8]. Sea urchin spermatozoa are found to be attracted to a surface through hydrodynamic interactions [36, 119, 26] that will also alter their beat pattern leading to swimming in a circular path and the formation of self-organized sperm vortices [106]. The swimming speed of the singly flagellated bacteria *Vibrio alginolyticus* was found, on average, to increase with the proximity of the surface [86]. Boundary element simulations of these bacteria [47] suggest that the increase in swimming speed is a result of swimming at an angle to the surface. In another study, Taylor's theoretical analysis of a swimming sheet [113] was extended [64] to include the effects of two nearby surfaces and the swimming speed was found to increase with the confinement.

In this chapter, we present results from particle based simulations of the artificial swimmer near a rigid surface. To capture the hydrodynamic effects of the surface, we introduce a new model that employs FCM in conjunction with the image systems of fundamental singularities of the Stokes equations together with lubrication force effects. We simulate the behavior of both planar and spiral actuated swimmers swimming parallel to the surface. We focus our discussion on the changes in swimming speed, the repulsion from the surface exhibited by the planar swimmer, and the rolling motion of a spiral swimmer near a surface.

8.2 Incorporating the hydrodynamic effects of the wall

Previously, to incorporate the hydrodynamic effects of a rigid surface into FCM, the Stokes equations with the appropriate finite force multipole expansion

$$\begin{aligned} \boldsymbol{\nabla} p - \eta \nabla^2 \mathbf{u} &= \sum_{n=1}^{N} \mathbf{F}^n_{ext} \Delta_n(\mathbf{x} - \mathbf{Y}_n) + \sum_{n=1}^{N} \mathbf{G}^n \cdot \boldsymbol{\nabla} \Xi_n(\mathbf{x} - \mathbf{Y}_n) \quad (8.1) \\ \boldsymbol{\nabla} \cdot \mathbf{u} &= 0 \quad (8.2) \end{aligned}$$

for an ensemble of N particles has been solved numerically [81, 28] with the no-slip condition

$$\mathbf{u}(0, y, z) = \mathbf{0} \quad (8.3)$$

at the surface $x = 0$. After determining the flow field, the motion of the particle phase can be determined through the usual FCM volume average integration. While this approach satisfies the no-slip condition exactly, it introduces need for a fixed computational grid. Such a computation will need additional bounding surfaces and/or periodic boundary conditions and may not be the most effective manner in which to simulate a small ensemble of particles. We, therefore, develop an alternative approach. Exploiting the linearity of the Stokes equations, we may write $\mathbf{u}$ as the sum of two separate flows

$$\mathbf{u} = \mathbf{u}_\infty + \mathbf{u}_{wall}. \quad (8.4)$$

In (8.4), $\mathbf{u}_\infty$ is the flow produced by the FCM force distribution (8.1) in an unbounded fluid. This is determined from the analytic solutions to the Stokes equations [91, 81]. To determine the flow field $\mathbf{u}_{wall}$ introduced to represent the effects of the rigid surface, we employ an image method and image solutions derived by Blake [12] for the fundamental singularities to the Stokes equations. This method provides a solution to the Stokes equations without the FCM force distribution

$$\nabla p - \eta \nabla^2 \mathbf{u} = \mathbf{0} \tag{8.5}$$

$$\nabla \cdot \mathbf{u} = 0 \tag{8.6}$$

that approximately satisfies the condition

$$\mathbf{u}_{wall}(0, y, z) \approx -\mathbf{u}_\infty(0, y, z) \tag{8.7}$$

at the rigid surface ($x = 0$). The image system for a point force (Stokeslet) of magnitude and direction F_i located at $\mathbf{Y} = (h, 0, 0)$ is [12, 101]

$$u_i^S = -\frac{F_j}{8\pi\eta}\left[\left(\frac{\delta_{ij}}{R} + \frac{X_i X_j}{R^3} +\right) + 2h(\delta_{j\alpha}\delta\alpha k - \delta_{j3}\delta_{3k})\frac{\partial}{\partial R_k}\left(h\frac{X_i}{R^3} - \left(\frac{\delta_{i3}}{R} + \frac{X_i X_3}{R^3}\right)\right)\right] \tag{8.8}$$

while the image system for the rotlet of magnitude τ_i [12]

$$u_i^R = -\frac{\tau_j}{8\pi\eta}\left[-\frac{\epsilon_{ijk}X_k}{R^3} + 2h\epsilon_{kj3}\left(\frac{\delta_{ik}}{R^3} - \frac{3X_i X_k}{R^5}\right) + 6\epsilon_{kj3}\frac{X_i X_k X_3}{R^5}\right] \tag{8.9}$$

where $\mathbf{X} = \mathbf{x} - \mathbf{x}_{im}$, $\mathbf{x}_{im} = \mathbf{Y} - 2h\hat{\mathbf{x}}$ and $R = |\mathbf{X}|$. For each particle in the simulation, we include both these flow fields in addition to the image flow field for a potential dipole as given in [12]. The strength of the image potential dipole is $\sigma_{n,\Delta}^2 \mathbf{F}_n/2$ to balance the corresponding term resulting from the monopole distribution. The sum of these $3N$ flows constitutes $\mathbf{u}_{wall}$. The motion of the particle phase is then determined from

$$\mathbf{V}_n = \int_{x>0} (\mathbf{u}_\infty + \mathbf{u}_{wall})\Delta_n(\mathbf{x} - \mathbf{Y}_n) d^3\mathbf{x} \tag{8.10}$$

$$\mathbf{\Omega}_n = \frac{1}{2}\int_{x>0} (\boldsymbol{\omega}_\infty + \boldsymbol{\omega}_{wall})\Xi_n(\mathbf{x} - \mathbf{Y}_n) d^3\mathbf{x}. \tag{8.11}$$

where the integration is performed over the half-space occupied by the fluid ($x > 0$).

The flow fields of these three image singularities provide the Faxén corrections in the far-field [65, 45]

$$\frac{F_1}{6\pi a\eta V_1} = \left[1 - \frac{9}{8}\frac{a}{h} + \frac{1}{2}\left(\frac{a}{h}\right)^3\right]^{-1} \tag{8.12}$$

$$\frac{F_2}{6\pi a\eta V_2} = \left[1 - \frac{9}{16}\frac{a}{h} + \frac{1}{8}\left(\frac{a}{h}\right)^3\right]^{-1} \tag{8.13}$$

$$\frac{\tau_3}{8\pi a^3\eta\Omega_3} = 1 + \frac{5}{16}\left(\frac{a}{h}\right)^3 \tag{8.14}$$

$$\frac{8\pi a^2\eta\Omega_3}{F_2} = \frac{1}{8}\left(\frac{a}{h}\right)^4 \tag{8.15}$$

for the particle motion when incorporated into FCM. In Figure 8.1, we compare the results from the FCM–image simulation of a single sphere with the values given by equations (8.12)–(8.15). In each case, the Faxén corrections are recovered in the far-field where they yield a reasonable estimate of the particle mobility.

Since FCM relies on force distributions and volume averages of the flow, the near contact particle-particle and particle-surface hydrodynamic effects will not be resolved. Lubrication forces can be introduced as an "external" force in the FCM calculation to represent the "unresolved" flow due to close contact [28]. Determining the local lubrication forces requires first computing the motion of the particles in the usual way. If a particle is sufficiently close to the wall, the additional lubrication force needs to be added to the monopole term to correct its motion. This force is estimated from a lubrication model for a sphere very close to a surface. The original FCM formulation of this calculation assumed that there were no external torques on the particles [28]. With the artificial swimmer, the elastic links exert torques on the particles and these must be accounted for in the lubrication correction.

Consider a single sphere of radius a located at $\mathbf{Y} = (h, 0, 0)$ and a rigid planar surface at $x = 0$. We define the normalized gap between the surface of the particle and the wall as $\epsilon = (h - a)/a$. A lubrication theory calculation yields the components of the mobility

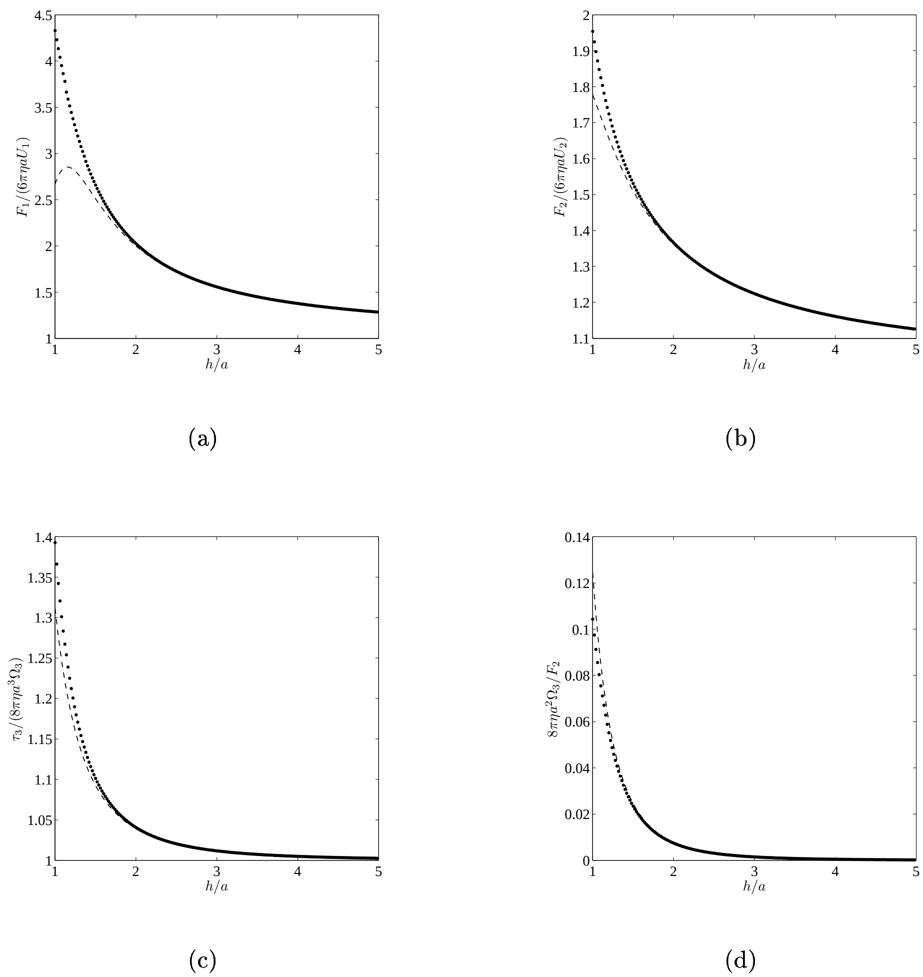

Figure 8.1: The motion of a single sphere near a rigid plane given by the FCM/image system (circular markers) and the Faxén corrections (dashed lines). (a) Perpendicular motion (8.12) (b) Parallel motion (8.13) (c) Rotational motion (8.14) (d) Rotation-Translation coupling (8.15)

Resistance Coefficient	C_0	C_1	C_2	C_3	C_4
A_{11}^{FCM-M}	0.5409	-2.4413	4.6702	-5.0119	4.2675
A_{22}^{FCM-M}	0.5304	-1.5859	2.0023	-1.5511	1.9724
B_{23}^{FCM-M}	-0.3336	0.9372	-1.0538	0.6156	-0.1774
C_{32}^{FCM-M}	-0.5686	1.5669	-1.6588	0.8521	-0.2016
D_{33}^{FCM-M}	0.5098	-1.4696	1.7244	-1.0891	1.3674
A_{11}^{FCM-MD}	0.8876	-3.4216	5.6918	-5.4808	4.3490
A_{22}^{FCM-MD}	0.6246	-1.8334	2.2377	-1.6475	1.9869
B_{23}^{FCM-MD}	-0.5424	1.5205	-1.6569	0.8934	-0.2271
C_{32}^{FCM-MD}	-0.6500	1.7761	-1.8518	0.9275	-0.2122
D_{33}^{FCM-MD}	0.7381	-2.0980	2.3569	-1.3665	1.4128

Table 8.1: Values of for the polynomial FCM resistance matrix $C_0\epsilon^4+C_1\epsilon^3+C_2\epsilon^2+C_4\epsilon+C_5$ determined from fits to simulation data.

matrix in the limit $\epsilon \ll 1$ [28]

$$A_{11} = -\frac{1}{\epsilon}+\frac{1}{5}\log\epsilon+\frac{1}{21}\epsilon\log\epsilon+O(1)+O(\epsilon) \quad (8.16)$$
$$A_{22} = \frac{8}{15}\log\epsilon+\frac{64}{375}\epsilon\log\epsilon+O(1)+O(\epsilon) \quad (8.17)$$
$$B_{23} = -\frac{2}{15}\log\epsilon-\frac{86}{375}\epsilon\log\epsilon+O(1)+O(\epsilon) \quad (8.18)$$
$$C_{32} = \frac{3}{4}B_{23} \quad (8.19)$$
$$D_{11} = \frac{1}{2}\epsilon\log\epsilon+O(1)+O(\epsilon) \quad (8.20)$$
$$D_{33} = \frac{2}{5}\log\epsilon+\frac{66}{125}\epsilon\log\epsilon+O(1)+O(\epsilon) \quad (8.21)$$

where

$$F_1 = 6\pi\eta a A_{11}V_1 \quad (8.22)$$
$$F_2 = 6\pi\eta a A_{22}V_2+6\pi\eta a^2 B_{23}\Omega_3 \quad (8.23)$$
$$F_3 = 6\pi\eta a A_{22}V_3-6\pi\eta a^2 B_{23}\Omega_2 \quad (8.24)$$
$$\tau_1 = 8\pi\eta a^3 D_{11}\Omega_1 \quad (8.25)$$
$$\tau_2 = -8\pi\eta a^2 C_{32}V_3+8\pi\eta a^3 D_{33}\Omega_2 \quad (8.26)$$
$$\tau_3 = 8\pi\eta a^3 C_{32}V_2+8\pi\eta a^3 D_{33}\Omega_3. \quad (8.27)$$

A similar set of height dependent coefficients can be found for FCM-image approach.

Resistance Coefficient	ϵ_{cut}	$O(\epsilon)$	$O(1)$
A_{11}^{FCM-M}	0.9	-0.5388ϵ	-0.4932
A_{22}^{FCM-M}	0.7	-0.5203ϵ	-0.8541
B_{23}^{FCM-M}	0.7	0.2777ϵ	-0.2776
C_{32}^{FCM-M}	0.7	0.2006ϵ	-0.2020
D_{33}^{FCM-M}	0.7	-0.7752ϵ	-0.2777
A_{11}^{FCM-MD}	0.9	-0.5374ϵ	-0.4942
A_{22}^{FCM-MD}	0.7	-0.5187ϵ	-0.8557
B_{23}^{FCM-MD}	0.7	0.2733ϵ	-0.2738
C_{32}^{FCM-MD}	0.7	0.1995ϵ	-0.2011
D_{33}^{FCM-MD}	0.7	-0.7727ϵ	-0.2534

Table 8.2: Values of the normalized cut-off distance for the lubrication barrier and the $O(\epsilon)$ and $O(1)$ corrections to the lubrication resistance matrix based on these cut-off values.

The results from single particle simulations performed at different heights are fitted with fourth order polynomials $C_0\epsilon^4 + C_1\epsilon^3 + C_2\epsilon^2 + C_4\epsilon + C_5$ using the polyfit function in MATLAB. These coefficients are provided in Table 8.1. With the FCM-image values of the resistance matrix the $O(1)$ and $O(\epsilon)$ terms in (8.16)–(8.21) are determined by matching each entry of the resistance matrix and its derivative at the normalized distance from the wall ϵ_{cut} where the lubrication correction first needs to be applied. With these values determined, the lubrication correction may be performed in the following manner:

1. After determining the velocities $\mathbf{V}_n$ and angular velocities $\mathbf{\Omega}_n$ for each particle n using the FCM-image approach, determine if there are particles less than the normalized lubrication cut-off distance ϵ_{cut} from the wall.

2. For those particles that are sufficiently close to the surface, we must determine the unknown hydrodynamic forces $\mathbf{H}_n$ and torques $\mathbf{L}_n$ on particle n due to the presence of the other particles [28]

$$\begin{bmatrix} \mathbf{H}_n \\ \mathbf{L}_n \end{bmatrix} = \mathcal{R}_{FCM} \begin{bmatrix} \mathbf{V}_n \\ \mathbf{\Omega}_n \end{bmatrix} - \begin{bmatrix} \mathbf{F}_n \\ \boldsymbol{\tau}_n \end{bmatrix} \tag{8.28}$$

   where $\mathcal{R}_{FCM}$ is the FCM-image resistance matrix determined from the fitted polynomials.

3. With the values of $\mathbf{H}_n$ and $\mathbf{L}_n$, the desired particle velocity $\mathbf{V}_{lub,n}$ and angular velocity

$\boldsymbol{\Omega}_{lub,n}$ for particle n are found from

$$\begin{bmatrix} \mathbf{V}_{lub,n} \\ \boldsymbol{\Omega}_{lub,n} \end{bmatrix} = \mathcal{M}_{lub} \begin{bmatrix} \mathbf{F}_n + \mathbf{H}_n \\ \boldsymbol{\tau}_n + \mathbf{L}_n \end{bmatrix}. \tag{8.29}$$

where $\mathcal{M}_{lub} = \mathcal{R}_{lub}^{-1}$ and $\mathcal{R}_{lub}$ is the lubrication resistance matrix (8.16)–(8.27).

4. Once the desired velocities are known, the barrier force $\mathbf{F}_{lub,n}$ and torque $\boldsymbol{\tau}_{lub,n}$ serve as an additional input to the FCM calculation and are found

$$\begin{bmatrix} \mathbf{F}_{lub,n} \\ \boldsymbol{\tau}_{lub,n} \end{bmatrix} = \mathcal{R}_{FCM} \begin{bmatrix} \mathbf{V}_{lub,n} \\ \boldsymbol{\Omega}_{lub,n} \end{bmatrix} - \begin{bmatrix} \mathbf{F}_n + \mathbf{H}_n \\ \boldsymbol{\tau}_n + \mathbf{L}_n \end{bmatrix}. \tag{8.30}$$

5. Finally, the velocities and angular velocities are again computed using the FCM-image approach with the input force and torque on particle n now given by $\mathbf{F}_n + \mathbf{F}_{lub,n}$ and $\boldsymbol{\tau}_n + \boldsymbol{\tau}_{lub,n}$ respectively.

In the lubrication correction, we did not account for near field changes in D_{11} since this term is not singular. Also, in the correction scheme, we employed different values of ϵ_{cut} for the motions perpendicular and parallel to the surface. This was possible since the two motions are independent.

In Figure 8.2, we compare results from the FCM-image approach with and without the lubrication correction to exact results [45, 18]. The addition of the lubrication clearly provides better estimation of the particle mobility near the surface. The largest difference between the exact results and the corrected simulations come in the overlap region. This is especially evident in Figure 8.2(d). The correspondence between the two in this region may be improved by including an additional image system for the stresslet. This will provide the far-field solution with a better estimate in the over-lap region, necessary to properly match with the inner lubrication solution.

8.3 Simulations of the artificial swimmer near a surface

We incorporate the model described in the previous section to account for the hydrodynamic effects of the surface into the artificial swimmer model described in Chapter 5. We use this to conduct simulations of the swimmer near a rigid surface. We examine the behavior of

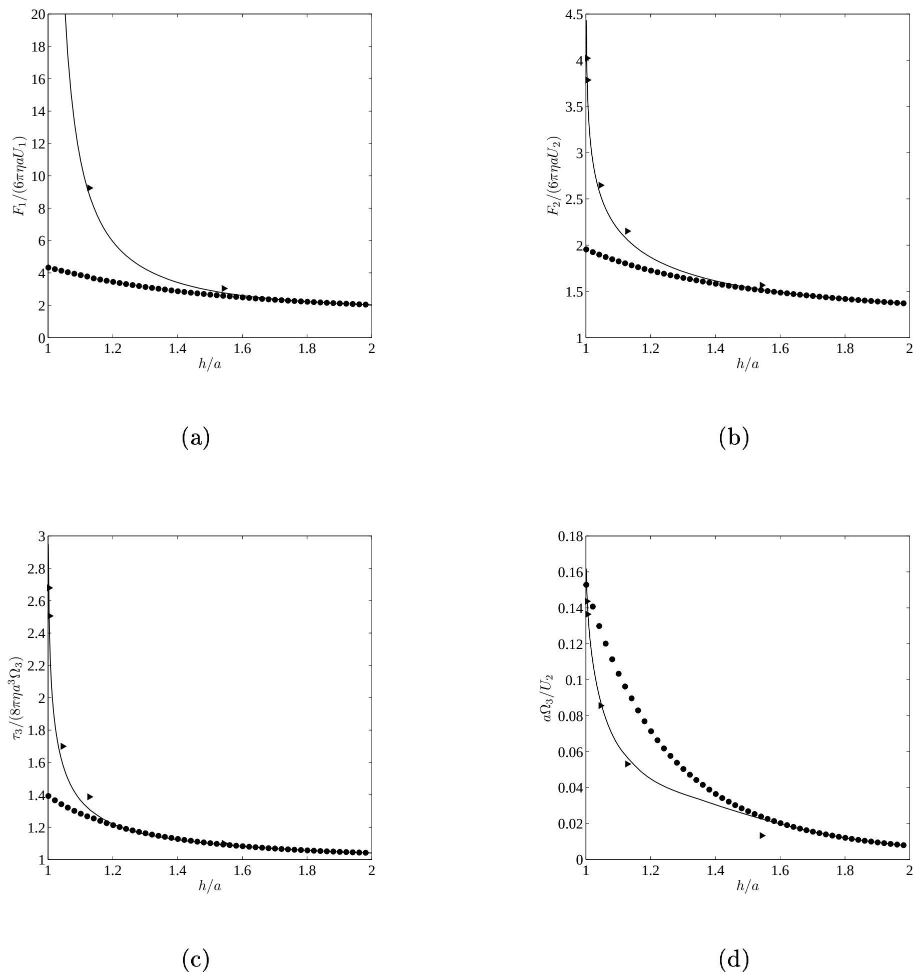

Figure 8.2: The motion of a single sphere near a rigid plane. The solid circular markers indicate the FCM-image approach, the triangular markers are the exact solutions to the Stokes equations provided by [45] and [18] and the solid lines show the FCM-image with the lubrication correction. (a) Perpendicular motion (b) Parallel motion (c) Rotational motion (d) Rotation-Translation coupling

swimmer driven by both the planar and spiral actuation schemes to examine the planar swimmer's changes in swimming speed, repulsion due to the wall and the 'rolling' motion of the spiral swimmer.

8.3.1 Changes in the Swimming Speed of a Planar Swimmer

We first examine the changes in swimming speed of the artificial swimmer driven by the planar field 5.1 swimming parallel to the surface. The swimmer is located at a height h from the surface and the transverse to constant field ratio is $h_0 = 1.0$. The length of swimmer's tail is $L = 32.8a$ and is comprised of $N = 15$ beads. The radius of the tethered sphere is $R = 6a$ giving the geometric ratio $R/L = 0.183$. For the cases considered the magnetoelastic number is fixed $Mn = 10$ and the scaled swimming speed U is determined for a given h over a range of Sp. The resulting swimming speeds are shown in Figure 8.3(a). We observe that for the heights considered here at low frequencies of the applied field (low Sp) the swimming speed will increase as the distance from the wall decreases. The opposite occurs at higher frequencies (high Sp).

The increase in swimming speed at low frequencies is surprising since one expects that as the the swimmer approaches the wall, the increase in drag will cause the speed to decrease. This will be the cases as long as the propulsive force remains constant. This may not occur with since the wave motion generated in the tail is coupled to the drag on the object. To account for the changes in drag on the filament tail, we modify the definition of Sp to include the effects of a height dependent drag coefficient to give

$$Sp^* = \left(\frac{\zeta_{||} \omega L^4}{K_b} \right). \tag{8.31}$$

The values of $\zeta_{||}$, the drag per unit length parallel to the filament's axis, are determined from FCM simulations, see Figure 8.4.

In figure 8.3(b) the swimming speed is plotted as a function of Sp^*. We see that the data collapses to a single curve in the low frequency limit while a non-monotonic dependence on the height is observed for higher values of Sp^*. The collapse of the data in the low frequency limit indicates that the increase in drag along the length of the tail is responsible for the increase in swimming speed. This suggests that the propulsive force increases with the increase in drag along the filament.

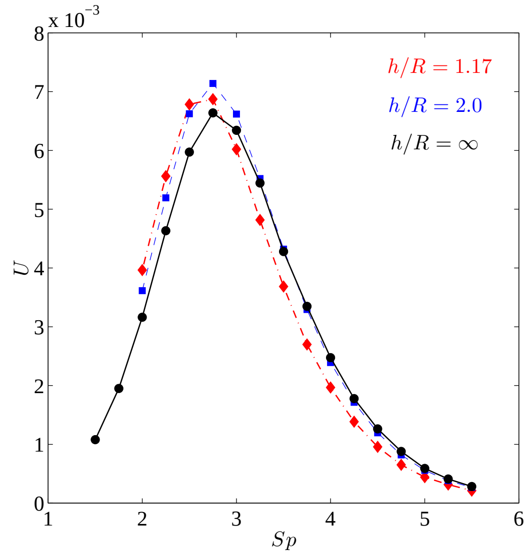

(a)

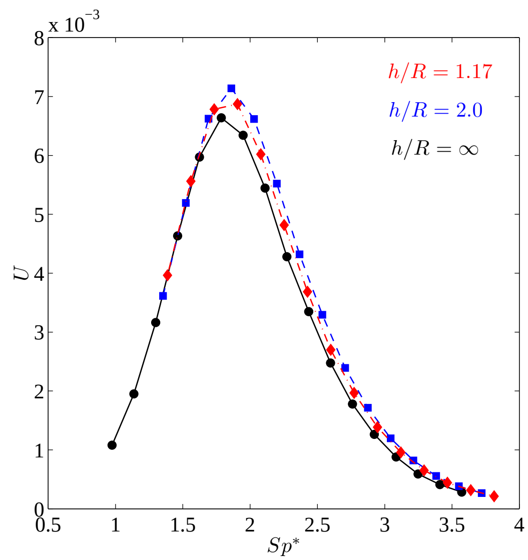

(b)

Figure 8.3: (a) Scaled swimming speed versus Sp for several heights. (b) Scaled swimming speed versus the rescaled sperm number Sp^*.

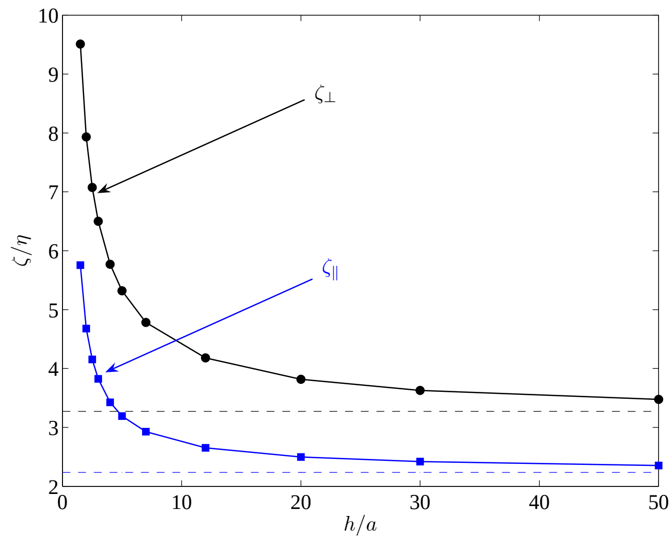

Figure 8.4: Changes in the drag per unit length on a filament consisting of $N = 15$ beads. The solid blue line with the square markers indicates the coefficient for motion parallel to the axis of the filament and the solid black line indicates the drag perpendicular to the axis. The dashed lines are the values of these coefficients in unbounded fluid.

Thus far, only the drag on the tail was considered, but the drag on the tethered sphere will also change as the swimmer approaches the surface. For the range of heights considered here, the drag on the tethered sphere would, if isolated, double. As this effect is not accounted for in Sp^* and the data lie on the same curve, the propulsive force appears to increase in proportion to the change in drag on the tethered sphere in the low frequency limit.

8.3.2 Repulsion from the Wall

In addition to changing the swimming speed, hydrodynamic interactions will cause the planar swimmer to move away from the surface. This repulsion is not caused by a reorientation of the swimming direction since the magnetic field keeps the beating and swimming parallel to the surface. The repulsion is a result of the artificial swimmer being a 'puller', that is, the filament tail leads in the swimming and pulls along the passive cargo. This generates a flow that is directed toward the swimmer along swimming axis and ejected along perpendicular directions to satisfy incompressibility. The outward flow must satisfy the no-slip condition at the stationary surface. This produces an additional flow that pushes the swimmer away from the surface. As the distance h from the surface increases, the repulsion velocity will

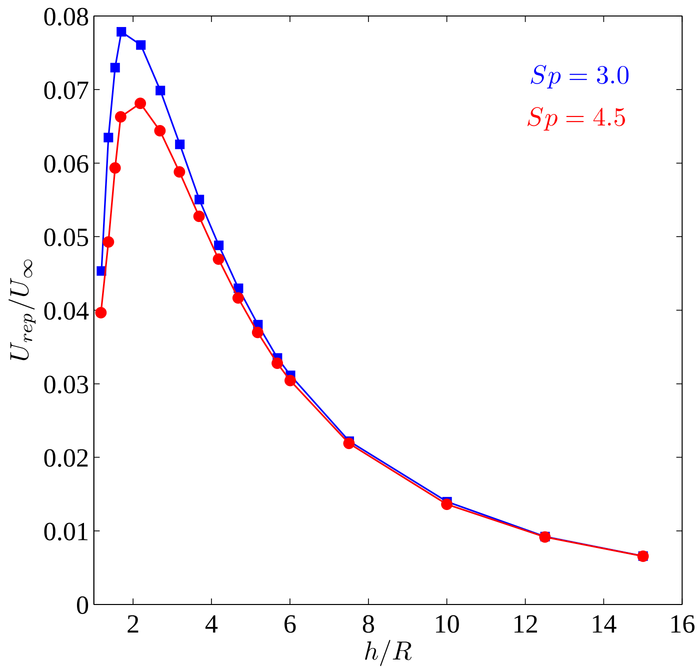

Figure 8.5: Repulsion speed of the planar swimmer for $Sp = 3.0$ and $Sp = 4.5$ as a function of the height h from the surface.

decay like h^{-2} which corresponds the to flow field generated by the image stresslet [85].

8.3.3 Rolling motion of a spiraling swimmer

In the resistance matrices presented above (8.16)–(8.21), we saw that in addition to changing the magnitude of the drag coefficients, the wall coupled the sphere's rotational and translational motion ($B_{23} \neq 0$). The spiraling swimmer which rotates about the swimming direction will, like the sphere, exhibit a rolling motion. This results in a translational motion that is perpendicular to its swimming direction causing the spiraling swimmer to travel in a straight line at an angle to its swimming direction in unbounded fluid. Figure 8.6 show the scaled swimming speed as a function of height for the two cases where $Sp = 3.0$ and $Sp = 4.5$. The scaled swimming speed is normalized by the free swimming value. It is evident that the rotation/translation coupling is quite strong in that the rolling speed becomes comparable to the swimming speed near contact. Additionally, the rolling velocity was found to decay like h^{-2} in the far field. This decay rate is much slower than the h^{-4} decay in the velocity of rotating sphere [65]. To understand this behavior consider the situation where a rigid sphere of radius a is driven by the force $\mathbf{F} = F\cos\omega t\hat{\mathbf{y}} + F\sin\omega t\hat{\mathbf{x}}$.

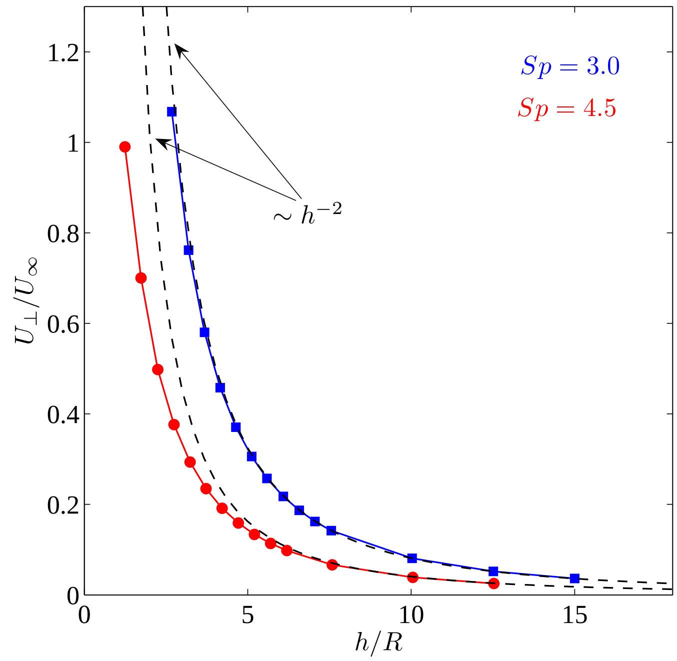

Figure 8.6: Rolling speed for $Sp = 3.0$ and $Sp = 4.5$ as a function of the height h from the surface.

Assuming the sphere is sufficiently far away from the surface at $x = 0$, $a/h \ll 1$, the instantaneous velocity of the sphere is given by [65]

$$V_{||} = \frac{1}{6\pi\eta a}\left[1 - \frac{9}{16}\frac{a}{h}\right] F\cos\omega t + O\left(\left(\frac{a}{h}\right)^3\right) \tag{8.32}$$

$$V_{\perp} = \frac{1}{6\pi\eta a}\left[1 - \frac{9}{8}\frac{a}{h}\right] F\sin\omega t + O\left(\left(\frac{a}{h}\right)^3\right) \tag{8.33}$$

where the height from the surface h is given by

$$h(t) = H + \int_0^t V_\perp(s)ds. \tag{8.34}$$

and $H = h(0)$. To obtain an expression for the time averaged velocity parallel to the surface

$$\langle V_{||}\rangle = \frac{\omega}{2\pi}\int_0^{2\pi/\omega} V_{||}(t)dt, \tag{8.35}$$

we first need to determine the height h as a function of time. Rewriting (8.33) as

$$V_{\perp} = \frac{1}{6\pi\eta a}\left[1 - \frac{9}{8}\frac{a}{H}\frac{1}{1+\int_0^t V_{\perp}(s)ds/H}\right] F\sin\omega t, \tag{8.36}$$

and assuming $\int_0^t V_{\perp}(s)ds/H \ll 1$ for all t, we find an integral equation for $V_{\perp}$

$$V_{\perp} \approx \frac{1}{6\pi\eta a}\left[1 - \frac{9}{8}\frac{a}{H}\left(1 + \frac{\int_0^t V_{\perp}(s)ds}{H}\right)\right] F\sin\omega t. \tag{8.37}$$

Rather than solving this directly, we invoke the assumption that $\int_0^t V_{\perp}(s)ds/H \ll 1$ and ignore the integral term on the right hand side and arrive at

$$V_{\perp} \approx \frac{1}{6\pi\eta a}\left[1 - \frac{9}{8}\frac{a}{H}\right] F\sin\omega t \tag{8.38}$$

which gives h as a function of time

$$h(t) = H + \frac{1}{6\pi\eta a}\left[1 - \frac{9}{8}\frac{a}{H}\right]\frac{F}{\omega}\left(1 - \cos\omega t\right). \tag{8.39}$$

We introduce the length scale b

$$b = \frac{1}{6\pi\eta a}\left[1 - \frac{9}{8}\frac{a}{H}\right]\frac{F}{\omega}. \tag{8.40}$$

and write the velocity parallel to the surface as

$$V_{||} = \frac{1}{6\pi\eta a}\left[1 - \frac{9}{16}\frac{a}{H}\frac{1}{1+b(1-\cos\omega t)/H}\right] F\cos\omega t \tag{8.41}$$

Again, assuming $\int_0^t V_{\perp}(s)ds/H \ll 1$, we may write $1/(1+b(1-\cos\omega t)/H)$ as a power series to obtain

$$V_{||} \approx \frac{1}{6\pi\eta a}\left[1 - \frac{9}{16}\frac{a}{H}\left(1 + \frac{b}{H}(1-\cos\omega t)\right)\right] F\cos\omega t. \tag{8.42}$$

Integrating to get the time averaged velocity component parallel to the surface, we find the only term the contributes is

$$\langle V_{||}\rangle = -\frac{\omega}{2\pi}\int_0^{2\pi/\omega} \frac{1}{6\pi\eta a}\frac{9}{16}\frac{a}{H}\frac{b}{H} F\cos^2\omega t dt, \tag{8.43}$$

which when evaluated is

$$\langle V_{||} \rangle = -\frac{1}{6\pi\eta}\frac{9}{32}\frac{Fb}{H^2}. \tag{8.44}$$

In this expression, we see that the time average parallel velocity decays in the far-field like H^{-2}. This is a consequence of the particle moving in a path of finite radius rather than simply rotating. Therefore, when considering the swimmer near a surface, a point torque representation is not sufficient to provide the correct scaling.

8.4 Conclusions

In this chapter, we analyzed the behavior of the artificial swimmer near a rigid surface. To do so, we incorporated an image system based hydrodynamic model for the planar surface into FCM and when necessary corrected the motion using lubrication forces. This method is an effective approach to introducing the effects of a single wall when only a few particles need to be considered and no other boundary conditions are introduced. We then performed simulations of both planar and spiral actuated swimmers near the surface and presented results concerning the change in the swimming speed. We also evaluated the slow drift away from the surface for the planar swimmer and the rolling motion exhibited by the spiral swimmer. We related the change in the swimming speed in the low frequency limit to the changes in the propulsive force due to the change in drag on the tail. The repulsion in the far-field decays like h^{-2} and can be related to the flow field of the image system for a symmetric point dipole. In the case of the rolling motion, we found that the coupling is quite strong in that it is comparable to the swimming speed and decays like h^{-2} which is slower than expected. The slow decay rate is supposed to be related to the components of the swimmer moving along an circular path. Unlike the case of repulsion, the rolling speed can not be related to the image system of a singularity.

We can identify certain behaviors demonstrated by the artificial swimmer that one might expect to be relevant in the cases of natural organisms. For example, the repulsion from the wall may be exhibited by a 'puller'-type microorganism that is generating a similar stresslet to propel itself. There are some difference too. The spiraling swimmer will roll as it swims causing the swimmer to move in a straight line at an angle to its swimming direction in unbounded fluid. A bacterium, however, will swim in a circular path parallel to the surface [77] due to the counter rotating cell head and flagellar bundle. Despite this, we might expect the same h^{-2} decay in the instantaneous velocity perpendicular to the swimming direction.

Chapter 9

Adaptation of the squirmer model to FCM

9.1 Introduction

The time-scale associated with the motion of the propulsive mechanism of a microorganism ($\approx 0.01s$) is typically much shorter than a time-scale given by the swimming speed, $U_s/L \approx 1s$. To provide a simulation capable of handling many interacting organisms over long times, one can utilize a model that does not consider the motion of the swimmers' propulsive elements but provides the time average of the leading order flow generated by each swimmer. For example, the phantom flagellum dumbbell model [54] accomplishes this by considering two point sources acting in opposite directions separated by a distance equal to the length of the swimmer while the self-locomoting rod model [110] utilizes stresses produced at several points along a section of an elongated object. The squirmer model for a swimming microorganism, as introduced by Ishikawa *et al.* [57], is a self-locomoting sphere that swims in response to a tangential velocity generated at its surface. Such an model is appropriate for organisms that employ cilia to generate surface waves as a means of propulsion (*Paramecia, Volvox, Opalina*, etc).

In this chapter, we demonstrate the broader impact of the methods developed and employed in this thesis by adapting the squirmer model to the FCM formulation. After outlining the squirmer model within the FCM framework, we conduct simulations of two interacting squirmers and a homogeneous suspension of $N = 2000$ squirmers. To examine the accuracy of the new formulation, we compare the trajectories of the two interacting squirmers and the self-diffusion coefficient of the squirmer suspension determined by the FCM-squirmer model with those given by the original simulations [57, 55].

9.2 A Single Squirmer

For a spherical body, tangential surface waves can be expanded in terms of an infinite series of the spherical harmonics for the Stokes equations, see Appendix A in [57]. The squirmer model retains only the first two terms of this series. The first term is a degenerate quadrapole whose strength is related to the velocity of the squirmer and is determined by the force-free condition. The second term provides a stresslet and corresponds to driving mechanism of the swimmer. These expressions can be rewritten in term of singularities of the Stokes equations

$$\frac{\partial p}{\partial x_i} - \eta\nabla^2 u_i = G^{sq}_{ij}\frac{\partial}{\partial x_j}\left(\delta(\mathbf{x}) + \frac{a^2}{6}\frac{\partial^2\delta(x)}{\partial x_k^2}\right) + H^{sq}_i\frac{\partial^2\delta(x)}{\partial x_k^2} \tag{9.1}$$

$$\frac{\partial u_j}{\partial x_j} = 0, \tag{9.2}$$

where

$$G^{sq}_{ij} = \frac{4}{3}\pi\eta a^2\left(3q_iq_j - \delta_{ij}\right)B_2 \tag{9.3}$$

$$H^{sq}_i = -\frac{4}{3}\pi\eta a^3 B_1 q_i, \tag{9.4}$$

and where q_i is the swimming direction and a is the radius of a squirmer. The parameter B_1 is related to the swimming speed U_s through $U_s = 2B_1/3$. The parameter B_2 is measured with respect to B_1 through the parameter $\beta = B_2/B_1$. If $\beta > 0$, the squirmer behaves as a 'puller' whereas if $\beta < 0$, the squirmer operates as a 'pusher'.

We recognize that these singularities can be adapted to the FCM framework. The stresslet term in (9.1) is just the flow singularity system of a single sphere under a net force, differentiated with respect to x_j. In FCM, this corresponds to a monopole Gaussian term, $\Delta(\mathbf{x})$, differentiated with respect to x_j. Unlike the stresslet term, there is not a natural choice of FCM Gaussian for the degenerate quadrapole. The length scale of the degenerate quadrapole Gaussian can then be chosen to provide an efficient simulation with a sufficiently accurate representation of the flow. We employ the FCM force dipole distribution $\Xi(\mathbf{x})$ for this term since it is shortest length scale in standard FCM. Therefore, for a single squirmer, the Stokes equations with the FCM squirmer force distribution are given by

$$\begin{aligned} \frac{\partial p}{\partial x_i} - \eta\nabla^2 u_i &= G_{ij}^{sq}\frac{\partial \Delta(\mathbf{x})}{\partial x_j} + H_i^{sq}\frac{\partial^2 \Xi(\mathbf{x})}{\partial x_k^2} && (9.5)\\ \frac{\partial u_j}{\partial x_j} &= 0. && (9.6) \end{aligned}$$

9.3 Squirmer-Squirmer Interactions

We are interested in using the squirmer model to simulate suspensions of thousands of interacting swimming organisms. The existing FCM machinery makes this task relatively simple. The linearity of the Stokes equations allows the squirming and hydrodynamic interactions to be, in some sense, treated separately. We, therefore, consider both the usual FCM sources associated with rigid spheres along with the squirming force distributions in the Stokes equations

$$\begin{aligned} \frac{\partial p}{\partial x_i} - \eta\nabla^2 u_i &= \sum_n \Big[F_i^n \Delta(\mathbf{x}-\mathbf{Y}_n) + G_{ij}^n \frac{\partial \Xi(\mathbf{x}-\mathbf{Y}_n)}{\partial x_j} \\ &\quad + G_{ij}^{n,sq}\frac{\partial \Delta(\mathbf{x}-\mathbf{Y}_n)}{\partial x_j} + H_i^{n,sq}\frac{\partial^2 \Xi(\mathbf{x}-\mathbf{Y}_n)}{\partial x_k^2}\Big] && (9.7)\\ \frac{\partial u_j}{\partial x_j} &= 0. && (9.8) \end{aligned}$$

By taking volume averages of the resulting flow field, we may determine the change in squirmer's motion as a result of the hydrodynamic interactions with the other particles. When performing this calculation, one must make sure that flows generated by each particle's own squirming modes do not yield any self-induced effects. We recognize that the integrals

$$\int P_{ij} H_j^{sq} \Delta(\mathbf{x}) d^3\mathbf{x} \qquad (9.9)$$

and

$$\int \frac{1}{2}\left(\frac{\partial R_{ijk} G_{jk}^{sq}}{\partial x_l} + \frac{\partial R_{ljk} G_{jk}^{sq}}{\partial x_i}\right) \Xi(\mathbf{x}) d^3\mathbf{x} \qquad (9.10)$$

will be non-zero and will artificially contribute to a particle's velocity and local rate of strain respectively. In (9.9), the tensor P_{ij} is given by [91]

$$
\begin{aligned}
P_{ij}(\mathbf{x}) &= \frac{1}{4\pi\eta r^3}\left[\delta_{ij} - \frac{3x_ix_j}{r^2}\right]\operatorname{erf}\left(\frac{r}{\sigma_\Xi\sqrt(2)}\right) && (9.11)\\
&-\frac{1}{\eta}\left[\left(\delta_{ij} - \frac{x_ix_j}{r^2}\right) + \left(\delta_{ij} - \frac{3x_ix_j}{r^2}\right)\left(\frac{\sigma_\Xi}{r}\right)^2\right]\Xi(\mathbf{x}) && (9.12)
\end{aligned}
$$

and the expression for R_{ijk} is given in Lomholt and Maxey [81]. R_{ijk} relates the squirming stresslet to its flow field

$$u_i^{sq} = R_{ijk}G_{jk}^{sq}. \tag{9.13}$$

For simulations where the interactions are determined pairwise using analytic expressions for the flow fields [91, 81] and local particle-fixed meshes, simply ignoring these terms will remove the self-induced motion. When working with a fixed numerical grid, however, the self-induced effects need to be subtracted from the total volume averages. The motion of a squirmer n is then given by

$$
\begin{aligned}
V_i^n &= U_sq_i + \int u_i\Delta(\mathbf{x}-\mathbf{Y}_n)d^3\mathbf{x} - \int P_{ij}H_j^{n,sq}\Delta(\mathbf{x})d^3\mathbf{x} && (9.14)\\
\Omega_i^n &= \frac{1}{2}\int \epsilon_{ijk}\frac{\partial u_k}{\partial x_j}\Xi(\mathbf{x}-\mathbf{Y}_n)d^3\mathbf{x} && (9.15)\\
E_{ij}^n &= \int \frac{1}{2}\left(\frac{\partial u_i}{\partial x_j} + \frac{\partial u_j}{\partial x_i}\right)\Xi(\mathbf{x}-\mathbf{Y}_n)d^3\mathbf{x} \\
&- \int \frac{1}{2}\left(\frac{\partial R_{ilk}G_{lk}^{n,sq}}{\partial x_j} + \frac{\partial R_{jlk}G_{lk}^{n,sq}}{\partial x_i}\right)\Xi(\mathbf{x})d^3\mathbf{x} && (9.16)
\end{aligned}
$$

9.4 Results

With the FCM squirmer model, we perform simulations to determine the motion of a sphere in the presence of a squirmer's flow field, the trajectories of a pair of squirmers, and the self-diffusion coefficient in a homogeneous suspension of squirmers. These cases were previously considered in [57] and [55] using boundary element and Stokesian dynamics simulations. By comparing with their results that also include effect of near-field hydrodynamic interactions, we may assess the accuracy of the FCM-squirmer formulation.

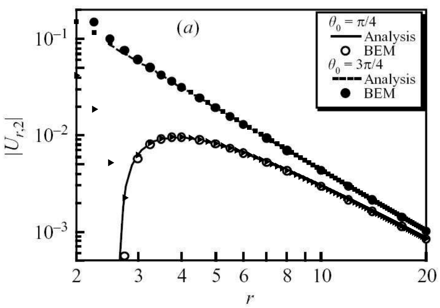

(a)

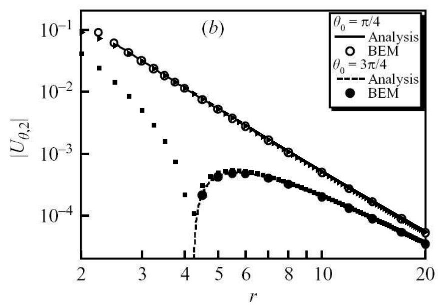

(b)

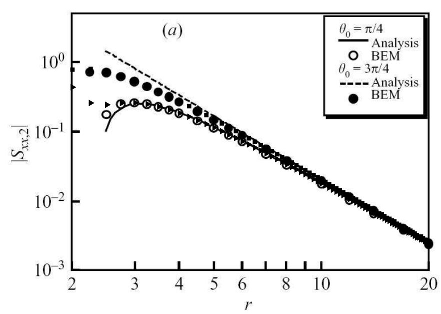

(c)

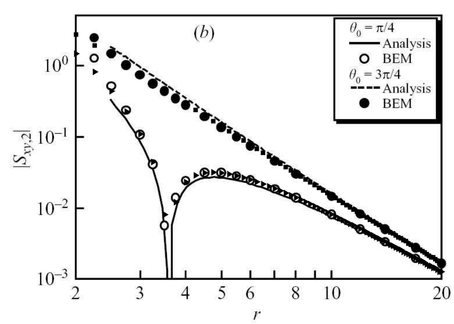

(d)

Figure 9.1: (a) $|U_r|$, (b) $|U_\theta|$, (c) $|S_{xx}|$, and (d) $|S_{xy}|$ of an inert sphere as a function of distance from a squirmer. The lines show the far-field analysis and the circular symbols the BEM simulation results [57]. The squares and triangles are the values determined using the FCM formulation.

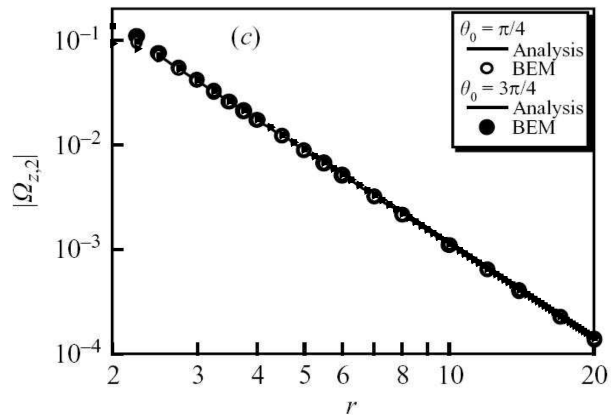

Figure 9.2: $|\Omega_z|$ of an inert sphere as a function of distance from a squirmer. The lines show the far-field analysis and the circular symbols the BEM simulation results [57]. The squares and triangles are the values determined using the FCM formulation.

9.4.1 Interactions between a squirmer and a sphere

We first consider the hydrodynamic effects of a squirmer on a nearby sphere. The squirming parameters are set to $\beta = 1$ and $B_1 = 3/2$. The particle configurations considered here are described in Figure 5 of [57]. The squirmer is located at the origin and oriented such that $\hat{\mathbf{q}} = \hat{\mathbf{x}}$. The sphere is located in the xy-plane at a distance r from the squirmer at an angle θ measured in a right-handed sense from the x-axis. The values of the sphere's velocity, $|U_r|$ and $|U_\theta|$, angular velocity, $|\Omega_z|$, and stresslet, $|S_{xx}|$ and $|S_{xy}|$, are determined of a range of r with $\theta_0 = \pi/4$ and $\theta_0 = 3\pi/4$ fixed. The resulting values are shown in Figures 9.1 and 9.2.

We see that FCM yields the correct values over a large range of separations. The FCM representation does begin to break down near contact when lubrication forces become important, especially in the case of the radial velocity $|U_r|$. Some improvements could be made by allowing the length scale of the degenerate force quadrapole Gaussian to be smaller, but this would require a more refined mesh resulting in a more computationally intensive simulation.

9.4.2 Trajectories of two interacting squirmers

We compute the trajectories of two squirmers and compare them with those determined using a database of pairwise forces and torques calculated from boundary element simula-

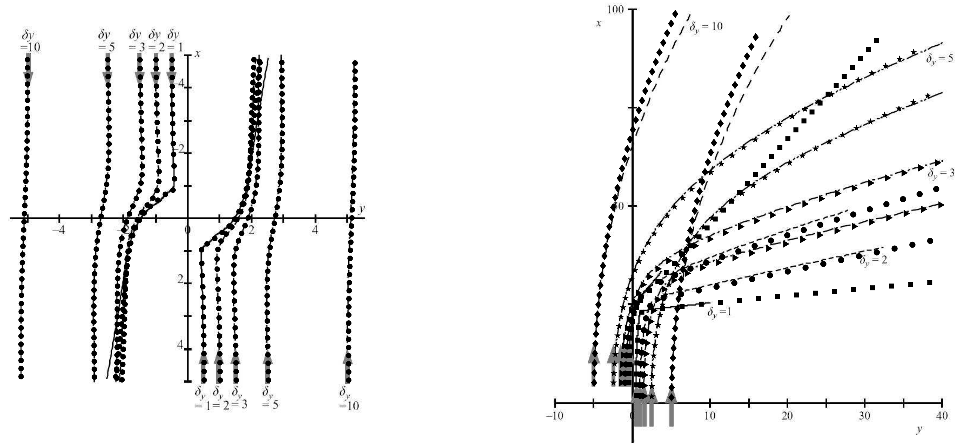

(a) (b)

Figure 9.3: Trajectories of two squirmers with ($\beta = 5$) moving in (a) opposite and (b) the same directions. In each plot, the symbols are provided by the FCM simulations while the lines are the results of [57].

tions [57]. In the cases considered, the squirmers may collide and we therefore include a collision barrier (2.38) to prevent the squirmers from overlapping. The first case considered is two squirmers ($\beta = 5$) one moving in the positive x-direction and the other in the negative x-direction. They are initially $10a$ apart in the x-direction, and the y separations considered are $1a$, $2a$, $5a$ and $10a$. The FCM results and those from [57] compare well as shown in Figure 9.3(a), except in the situation where a collision occurs. As squirmer reorientation is the key factor in determining the final trajectory, the collision dynamics need to be exactly the same in order for the resulting trajectories to be similar. We also compare the case where the two squirmers swim in the positive x-direction (Figure 9.3(b)). Once again the FCM results compare well with those of Ishikawa *et al.* in all but the case of largest separation. The origin of the discrepancy is unknown since the interactions are well resolved by FCM at this distance, see Figures 9.1 and 9.2.

9.4.3 Self-diffusion of a squirmer

We conduct simulations of a homogeneous suspension of squirmers using a Fourier collocation algorithm to solve (9.7) in a periodic domain and obtain the flow $\mathbf{u}(x, y, z)$ on 192^3 grid

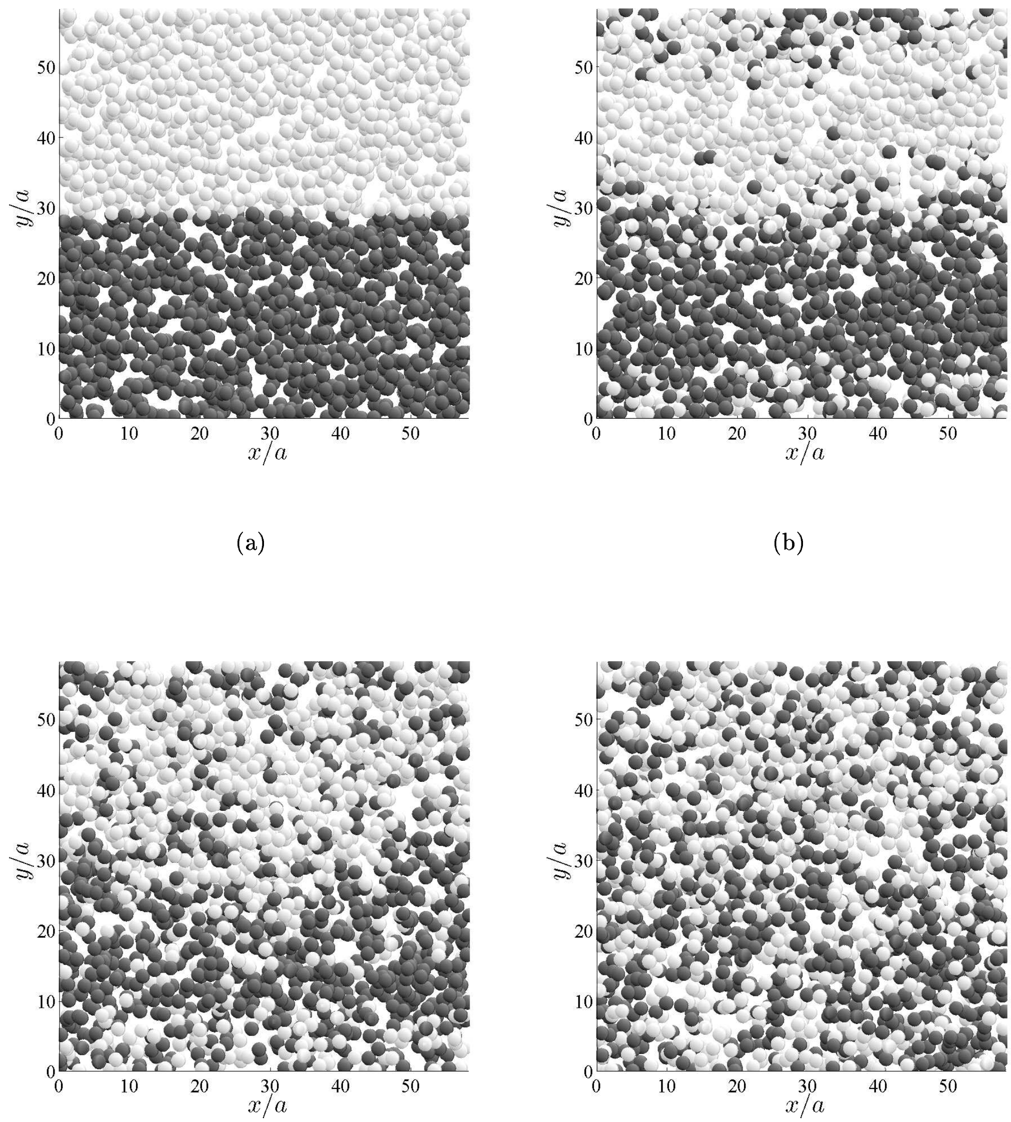

(a) (b) (c) (d)

Figure 9.4: Evolution of a suspension of $N = 2000$ squirmers initially swimming in the positive x-direction. (a) $t = 0a/U_s$ (b) $t = 13.9a/U_s$ (c) $t = 27.8a/U_s$ (d) $t = 41.7a/U_s$

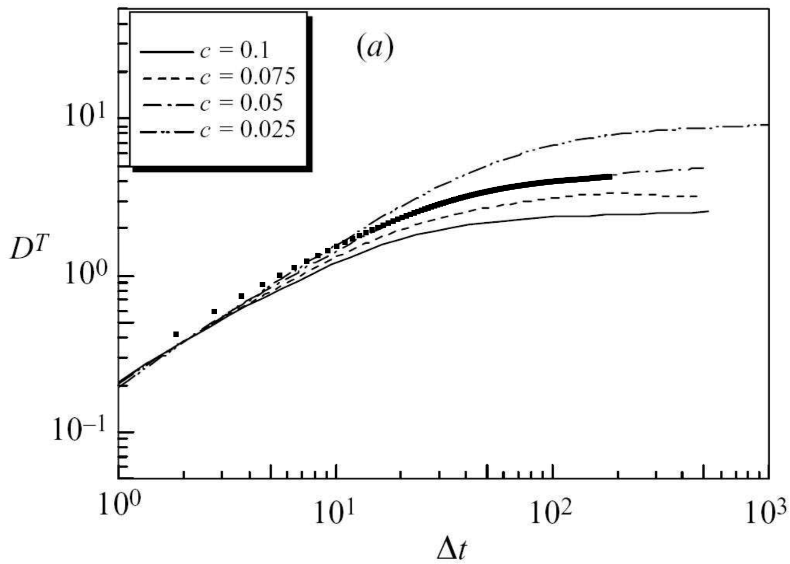

Figure 9.5: Translational self-diffusion coefficient of a squirmer ($\beta = 5$) as a function of Δt. A constant value indicates a diffusive mode. The FCM results are shown as black squares and correspond to a simulation of $N = 2000$ and volume fraction $c = 0.042$. The lines for $c = 0.025 - -0.1$ are from [55].

points. The computations are performed on eight Intel Xeon 2.80GHz processors. In the simulation, we consider $N = 2000$ independent squirmers which corresponds to a volume fraction of $c = 0.042$. The squirming parameter for each squirmer is set to $\beta = 5$. To begin the simulation, the squirmers are distributed uniformly in the box, but they are all oriented in the same direction with $\hat{\mathbf{q}}_n = \hat{\mathbf{x}}$ for $n = 1, \ldots, N$. The evolution of the suspension over time is shown in Figure 9.4 where the squirmers initially in the lower half of the box are shaded gray while those in the upper half are white. We see that the initial configuration of all squirmers swimming in the same direction is unstable [112, 110, 54] and over time mixing of the two halves occurs.

The mixing seen Figure 9.4 is related to the effective diffusion of the squirmers that occurs as a result of hydrodynamic interactions with neighboring particles. The self-diffusion coefficient over time can be determined from

$$D_{ii}(\Delta t) = \left\langle \frac{(Y_i(t + \Delta t) - Y_i(t))^2}{6\Delta t} \right\rangle \tag{9.17}$$

where the sum over i is implied. The value of the squirmer self-diffusion coefficient from our simulations along with those provided by [55] are plotted in Figure 9.5. Despite ignoring the near-field lubrication forces and employing the collision barrier, the self-diffusion coefficients are remarkably similar when we compare our results for $c = 0.042$ for those at $c = 0.05$ from [55]. In addition, we see that with the FCM-squirmer model we can handle a simulation with nearly two orders of magnitude more squirmers than the $N = 27$ considered in [55].

9.5 Conclusions

In this chapter, we presented an FCM formulation of the squirmer model for a microorganism. By comparing with results from boundary element [57] and Stokesian dynamics simulations [55], we found that the FCM formulations reproduces quite well the squirmer-squirmer interactions and provides an accurate estimate of squirmer suspension properties. In addition, the FCM formulation of the squirmer model is capable of simulating many more squirmers than the Stokesian dynamics approach.

Chapter 10

Concluding Remarks

10.1 Summary of Results

Over the course of this thesis, we developed new techniques to model efficiently the forces experienced by paramagnetic particles (Chapter 2) and employed these models in simulations for the physics of suspensions of paramagnetic particles and the dynamics of artificial micro-swimmers. The first of the models is provided in Chapter 3 and concerns the magnetic interactions between the beads. We introduced a finite-dipole model to resolve the far-field magnetic interactions where the magnetization of each particle is represented using a Gaussian distribution of current density in the equations for the magnetic field. Unlike point-dipole approaches where the computational work increases with the number of particles squared, the computational work associated with the finite-dipole model scales linearly with the number of particles. Along with this model, we provided a higher multipole inclusion method based of the exact solution to the two-body problem to resolve the near-field interactions. The inclusion procedure is general and may be used in conjunction with either the finite-dipole model or any point dipole representation. Through a series of multi-body problems, we found that a dipole model enhanced by the inclusion procedure yields an accurate estimate of the interparticle magnetic force, especially in axisymmetric configurations.

In Chapter 4, we presented results from simulations employing the new magnetic interaction model coupled with FCM to provide the solution to the low Reynolds number mobility problem. The surface forces and solid body contact are introduced through a generic short-range barrier force (§2.4). The effects of this force on the oscillations exhibited by a pair of paramagnetic beads in a rotating field was considered in §4.2 and comparisons with experiment indicate the presence of a similar repulsive force between the particles. We provided simulations of chains subject to rotating fields and shear flows and in each case calculate the lowest value of the Mason number, Ma_{rot} or Ma_{shear}, at which a chain of N beads will first break. By comparing these results with those determined using a hydrodynamic drag and point dipole based chain model [88], [94] we demonstrated the importance of the hydrodynamic interactions along the length of the chain. When we modified the chain model to include these effects, the simulation results are well reproduced. Additionally in Chapter 4, we considered an initially homogeneous suspension subject to a rotating applied field. As in the experiments [93], we found that below a critical value of Ma_{rot}, the beads aggregated to form chains that rotated with the applied field, while above Ma^{crit}_{rot}, small planar clusters were observed. The number of particles that are members of clusters and the shape of these clusters can be related to the results from dichroism experiments.

Along with the simulations of ensembles of paramagnetic particles, we conducted simulations of the artificial micro-swimmer [33]. This device is constructed from a chain of chemically linked paramagnetic particles connected to a red blood cell. To facilitate simulations of this device, we introduced an elastic coupling model described in Chapter 5 where each individual chemical link is treated as an inextensible flexible rod. This model is verified by considering the equilibrium shape and effective drag coefficient of a filament settling in a viscous fluid. With the elastic coupling procedure, the mutual dipole model and FCM, we performed simulations of the artificial micro-swimmer driven by the originally proposed oscillating magnetic field 5.1 and found the scaled swimming speeds are comparable to those experimentally measured, especially at high Sp. In Chapter 6, we demonstrated that the micro-swimmer may be propelled using an alternative applied field strategy. Specifically, we showed that using rotating fields the swimmer will deform into a corkscrew shape that rotates with the same frequency as the applied field and spirals its way through the fluid. From the simulations, we extracted a parameterization of the swimmer kinematics under this mode of operation, and using a continuous elastica/resistive force description of the filament tail, we examined the relation between the swimming speed and the magnetic forces and swimmer geometry in the low frequency limit. In Chapter 7, we used the simulation technique to quantify the interactions between two comoving artificial swimmers. Using a low order force multipole expansion for the force distribution the swimmer exerts on the fluid, we demonstrated the hydrodynamic interactions decay as h^{-2} where h is the separation distance. In a similar study, we quantified the behavior of the swimmer near a rigid surface using an image/lubrication barrier method described in Chapter 8. We first addressed the changes in swimming speed of a planar swimmer swimming parallel to the surface. At low frequencies, the scaled swimming speed increased as the distance from the surface decreased. In this limit we saw that for the range of heights considered, that rescaling Sp to include the changes in drag on the filament tail collapsed the data onto a single curve. Additionally, the planar swimmer was repelled from the surface since it generates a 'puller'-type stresslet. We also saw that with a spiral swimmer, the device will roll as it swims moving in a straight line at an angle to its natural swimming direction. The rolling speed decayed as h^{-2} rather than h^{-4}. This difference was explained by considering an analogous problem of a sphere forced to move in a circle near a surface.

While the methods developed in this thesis were originally intended for describing the motion of paramagnetic particle in suspension, they can be extended and adapted to address other problems in suspension physics. As an example, in Chapter 9, we adapt the squirmer model for a swimming microorganism [57] into the FCM formulation. While this approach does not resolve the short-range lubrication interactions accounted for in the original studies, it reproduces interacting squirmer trajectories and the self-diffusion coefficient for a squirmer in a suspension.

10.2 Future Directions

In this thesis, we established simulation techniques to handle the many-body magnetic interactions between paramagnetic beads MR fluids and with FCM, were able to conduct simulations of ensembles thousands of particles. While we focused our studies on initially homogeneous particles subject to a rotating applied field, using the same methods, one can conduct simulations of MR fluids in wall bounded channel flows or in uniform shear flows. Such simulations of thousands of particles at this level of detail have not been performed and would provide information valuable to microfluidic design and MR fluid rheology. In the case of the later, new lubrication barriers providing stresslet information [120] could be included to allow for studies of very high volume fraction suspensions. There has also been a great deal of experimental data measuring the growth rates of chains in suspensions immersed in a uniform applied field. A large scale simulation of this process that includes the hydrodynamic interactions between particles has yet to be performed, and could be done using these methods. For a proper comparison, however, the Brownian forces will need to be taken into consideration. In an initial study, Brownian motion can be included using the approach adopted by Climent *et al.* [25] where the statistics regarding the random forcing ignore the hydrodynamic interactions

$$\langle \mathbf{F}_{rand}(t) \rangle = \mathbf{0} \tag{10.1}$$

$$\left\langle \mathbf{F}_{rand}(t)\mathbf{F}_{rand}(t') \right\rangle = 12\pi\eta a k_B T \mathcal{I}_{ij}\delta(t-t'). \tag{10.2}$$

With these statistics, the resulting diffusion tensor is

$$\mathcal{D}_{ij} = 6\pi a\eta k_B T \mathcal{M}_{ik}(t)\mathcal{M}_{jk}(t) \tag{10.3}$$

rather than $\mathcal{D}_{ij} = k_B T \mathcal{M}_{ij}$. To obtain a more accurate value of $\mathcal{D}_{ij}$ requires the determination of $\sqrt{\mathcal{R}_{ij}}$. Accelerated Stokesian dynamics [2] and particle mesh Ewald methods [53] employ a method introduced by Fixman [38] to address this issue. An alternative approach might be that used by Sharma and Patankar *et al.* [111] and Ladd [71] where a random, fluctuating stress is introduced in the fluid phase [75]. Fox and Uhlenbeck [39] showed that the correct particle diffusion is recovered if the no-slip boundary condition is satisfied exactly. This approach could readily be adapted to FCM, however, care must be taken since the no-slip boundary condition is not satisfied exactly and the fluctuating stresses are independent of particle configuration.

We also presented a model that is effective in simulating the behavior of magnetic filaments constructed from chemically linked paramagnetic particles. This method can be used to provide simulations of newly realized biomimetic devices utilizing these filaments. By attaching one end of the filament to a channel wall, experimentalists have been able to create arrays of artificial cilia [37] that can be used to pump or mix fluid in the channel. Simulations of these artificial cilia can be conducted using the methods described in this thesis to reveal optimal applied field strategies or array patterns.

Finally, we demonstrated the impact of the methods beyond suspensions of paramagnetic particles and artificial micro-swimmers by adapting the squirmer model to FCM enabling large scale simulations of suspensions of microorganisms. This model can be further enhanced to include the effects of chemical gradients to explore chemotactic behavior or modified to consider ellipsoidal squirmers [79]. The filament model can be employed in a variety of scenarios. For example, by including the effects of Brownian motion the behavior of suspensions of biofilaments can be examined. In our simulations, the placement of the links on the surface of the beads was always such that in the absence of any applied forces, the filament would relax to a linear configuration. The attachment points of the links can be distributed in other ways giving the filament a predefined curvature. For example, beads can be joined together along a helical path to provide a corkscrew-shaped flagellum tail of a model bacteria.

Bibliography

[1] M.P. Allen and D.J. Tildesley. *Computer Simulation of Liquids*. Clarendon Press, 1994.

[2] A.J. Banchio and J.F. Brady. Accelerated stokesian dynamics: Brownian motion. *J. Chem. Phys.*, 118(22):10323–10332, 2003.

[3] G.K. Batchelor. *An Introduction to Fluid Dynamics*. Cambridge University Press, 1967.

[4] G.K. Batchelor. Brownian diffusion of particles with hydrodynamic interaction. *J. Fluid Mech.*, 74:1–29, 1976.

[5] L.E. Becker, S.A. Koehler, and H.A. Stone. On self-propulsion of micro-machines at low Reynolds number: Purcell's three-link swimmer. *J. Fluid Mech.*, 490:15–35, 2003.

[6] L.E. Becker and M.J. Shelley. Instability of elastic filaments in shear flow yields first-normal-stress differences. *Phys. Rev. Lett.*, 87:198301, 2001.

[7] H.C. Berg. How to track bacteria. *Rev. Sci. Instrum.*, 42:868–871, 1971.

[8] H.C. Berg and L. Turner. Chemotaxis of bacteria in glass capillary arrays. *Biophys. J.*, 58:919–930, 1990.

[9] S.L. Biswal and A.P. Gast. Mechanics of semiflexible chains formed by poly(ethylene glycol)-linked paramagnetic particles. *Phys. Rev. E*, 68:021402, 2003.

[10] S.L. Biswal and A.P. Gast. Micromixing with linked chains of paramagnetic particles. *Anal. Chem.*, 76:6448–6455, 2004.

[11] S.L. Biswal and A.P. Gast. Rotational dynamics of semiflexible paramagnetic particle chains. *Phys. Rev. E*, 69(041406), 2004.

[12] J.R. Blake and A.T. Chwang. Fundamental singularities of viscous flow. *J. Eng. Math.*, 8(1):23–29, 1974.

[13] S. Bleil, D.W.M. Marr, and C. Bechinger. Microscopic artificial swimmers. *Nature*, 437:862–865, 2005.

[14] R.T. Bonnecaze and J.F. Brady. A method for determining the effective conductivity of dispersions of particles. *Proc. R. Soc. Lond. A*, 430:285–313, 1990.

[15] R.T. Bonnecaze and J.F. Brady. The effective conductivity of random suspensions of spherical particles. *Proc. R. Soc. Lond. A*, 432:445–465, 1991.

[16] R.T. Bonnecaze and J.F. Brady. Dynamic simulation of an electrorheological fluid. *J. Chem. Phys.*, 96(3):2183–2202, 1992.

[17] C. Brennen and H. Winet. Fluid mechanics of propulsion by cilia and flagella. *Ann. Rev. Fluid Mech.*, 9:339–398, 1977.

[18] H. Brenner. The slow motion of a sphere through a viscous fluid towards a plane surface. *Chem. Engng Sci.*, 16:242–251, 1961.

[19] A. Cebers. Flexible magnetic filaments in a shear flow. *J. Magn. Magn. Mater.*, 300:67–70, 2006.

[20] A. Cebers and I. Javaitis. Bending of flexible magnetic rods. *Phys. Rev. E*, 70:021404, 2004.

[21] A. Cebers and I. Javaitis. Dynamics of a flexible magnetic chain in a rotating magnetic field. *Phys. Rev. E*, 69:021404, 2004.

[22] S. Chattopadhyay, R. Moldovan, C. Yeung, and X.L. Yu. Swimming efficiency of bacterium *Escherichia Coli*. *PNAS*, 103(37):13712–13717, 2006.

[23] H.J.H. Clercx and G. Bossis. Many-body electrostatic interactions in electrorheological fluids. *Phys. Rev. E*, 48(4):2721–2738, 1993.

[24] E. Climent and M.R. Maxey. Numerical simulation of random suspensions at finite reynolds numbers. *Int. J. Multiphase Flow*, 29:579–601, 2003.

[25] E. Climent, M.R. Maxey, and G.E. Karniadakis. Dynamics of self-assembled chaining in magnetorheological fluids. *Langmuir*, 20(2):507–513, 2004.

[26] J. Cosson, P. Huitorel, and C. Gagnon. How spermatozoa come to be confined to surfaces. *Cell Motility and the Cytoskeleton*, 54:56–63, 2003.

[27] S.L. Dance, E. Climent, and M.R. Maxey. Collision barrier effects on the bulk flow in a random suspension. *Phys. Fluids*, 16:828–831, 2004.

[28] S.L. Dance and M.R. Maxey. Incorporation of lubrication effects into the force-coupling method for particulate two-phase flow. *J. Comp. Phys.*, 189:212–238, 2003.

[29] T. Darden, D. York, and L. Pederson. Particle mesh ewald - an nlog(n) method for ewald sums in large systems. *J. Chem. Phys.*, 98(12):10089–10092, 1993.

[30] C. Dombrowski, L. Cisneros, S. Chatkaew, R.E. Goldstein, and J.O. Kessler. Self-concentration and large-scale coherence in bacterial dynamics. *Phys. Rev. Lett.*, 93(9):098103, 2004.

[31] P. Domínguez-García, S. Melle, J.M. Pastor, and M.A. Rubio. Scaling in the aggregation dynamics of a magnetorheological fluid. *Phys. Rev. E*, 76:051403, 2007.

[32] P.S. Doyle, J. Bibette, A. Bancaud, and J.-L. Viovy. Self-assembled magnetic matrices for DNA separation chips. *Science*, 295:2237, 2002.

[33] R. Dreyfus, J. Baudry, M. L. Roper, M. Fermigier, H.A. Stone, and J. Bibette. Microscopic artificial swimmers. *Nature*, 437:862–865, 2005.

[34] A. Einstein. *Investigations on the Theory of the Brownian Movement.* Dover Publications, Inc., 1956.

[35] Z.H. Fan and R. Kumar. Biological applications of paramagnetic particles in chips. In J. Chang and L. Kricka, editors, *Biochip Technology*, pages 291–307. Hardwood Academic Publishers, 2001.

[36] L.J. Fauci and A. McDonald. Sperm motility in the presence of boundaries. *Bull. Math. Biol.*, 57:679–699, 1995.

[37] M. Fermigier. Personal communication. 2007.

[38] M. Fixman. Construction of langevin forces in the simulation of hydrodynamic interaction. *Macromolecules*, 19:1204–1207, 1986.

[39] R.F. Fox and G.E. Uhlenbeck. Contributions to non-equilibrium thermodynamics. i. theory of hydrodynamical fluctuations. *Phys. Fluids*, 13(8):1893–1902, 1970.

[40] B.M. Friedrich and F. Jülicher. Chemotaxis of sperm cells. *Proc. Natl. Acad. Sci. USA*, 104:13256–13261, 2007.

[41] E.M. Furst and A.P. Gast. Micromechanics of dipolar chains using optical tweezers. *Phys. Rev. Lett.*, 82(20):4130–4133, 1999.

[42] E.M. Furst and A.P. Gast. Dynamics and lateral interactions of dipolar chains. *Phys. Rev. E*, 62(5):6916–6925, 2000.

[43] E.M. Furst and A.P. Gast. Micromechanics of magnetorheological suspensions. *Phys. Rev. E*, 61(6):6732–6739, 2000.

[44] E. Gauger and H. Stark. Numerical study of a microscopic artificial swimmer. *Phys. Rev. E*, 74:021907, 2006.

[45] A.J. Goldman, R.G. Cox, and H. Brenner. Slow viscous motion of a sphere parallel to a plane wall–i motion through a quiescent fluid. *Chem. Engng Sci.*, 22:637–651, 1967.

[46] H.L. Goldsmith and S.G. Mason. The microrheology of dispersions. In F.R. Eirich, editor, *Rheology: Theory and Applications*, volume 4, pages 85–250. Academic Press, 1967.

[47] T. Goto, K. Nakata, K. Baba, M. Nishimura, and Y. Magariyama. A fluid-dynamic interpretation of the asymmetric motion of singly flagellated bacteria swimming close to a boundary. *Biophys. J.*, 89:3771–3779, 2005.

[48] C. Goubault, P. Jop, M. Fermigier, J. Baudry, E. Bertrand, and J. Bibette. Flexible magnetic filaments as micromechanical sensors. *Phys. Rev. Lett.*, 91(26):260802, 2003.

[49] L. Greengard and V. Rokhlin. A fast algorithm for particle simulations. *J. Comp. Phys.*, 73:325–348, 1987.

[50] J. Happel and H. Brenner. *Low Reynolds Number Hydrodynamics.* Prentice Hall, 1965.

[51] G. Helgesen, P. Pieranski, and A.T. Skjeltorp. Dynamic behavior of simple magnetic hole systems. *Phys. Rev. A*, 42(12):7271–7280, 1990.

[52] L.E. Helseth. Self-assembly of colloidal pyramids in magnetic fields. *Langmuir*, 21:7276–7279, 2005.

[53] J.P. Hernández-Ortiz, J.J. de Pablo, and M.D. Graham. Fast computation of many-particle hydrodynamic and electrostatic interactions in a confined geometry. *Phys. Rev. Lett.*, 98:140602, 2007.

[54] J.P. Hernandez-Ortiz, C.G. Stoltz, and M.D. Graham. Transport and collective dynamics in suspensions of confined swimming particles. *Phys. Rev. Lett.*, 95(20):204501, 2005.

[55] T. Ishikawa and T.J. Pedley. Diffusion of swimming model micro-organisms in a semi-dilute suspension. *J. Fluid Mech.*, 588:437–462, 2007.

[56] T. Ishikawa, G. Sekiya, Y. Imai, and T. Yamaguchi. Hydrodynamic interactions between two swimming bacteria. *Biophys. J.*, 93:2217–2225, 2007.

[57] T. Ishikawa, M.P. Simmonds, and T.J. Pedley. Hydrodynamic interaction of two swimming model micro-organisms. *J. Fluid Mech.*, 568:119–160, 2006.

[58] J.N. Israelachvili. *Intermolecular and Surface Forces.* Academic Press, 2 edition, 1992.

[59] J.D. Jackson. *Classical Electrodynamics.* John Wiley and Sons, Inc., 3 edition, 1999.

[60] G.B. Jeffery. The motion of ellipsoidal particles immersed in a viscous fluid. *Proc. R. Soc. Lond. A*, 102:161–179, 1922.

[61] D.J. Jeffrey. Conduction through a random suspension of spheres. *Proc. R. Soc. Lond. A*, 335:355–367, 1973.

[62] G.E. Karniadakis, M. Israeli, and S.A.Orszag. High-order splitting methods for the incompressible Navier-Stokes equations. *J. Comp. Phys.*, 97:414–443, 1991.

[63] B. Kashevsky and V.A. Kuzmin. Pair interaction in magnetic suspensions under a rotating field: the influence of particle surface conditions. *J. Phys. D: Appl. Phys.*, 29:2579–2585, 1996.

[64] D.F. Katz. On the propulsion of micro-organisms near solid boundaries. *J. Fluid Mech.*, 64:33–50, 1974.

[65] S. Kim and S. J. Karrila. *Microhydrodynamics: Principles and Selected Applications.* Dover Publications, Inc., 2005.

[66] D. J. Klingenberg and C. F. Zukoski IV. Studies on the steady-shear behavior of electrorheological suspensions. *Langmuir*, 6:15–24, 1990.

[67] D.J. Klingenberg. Magnetorheology: Applications and challenges. *AIChE J.*, 47:246–249, 2001.

[68] D.J. Klingenberg, J.C. Ulicny, and M.A. Golden. Mason numbers for magnetorheology. *J. Rheol.*, 47:759–778, 2007.

[69] D.J. Klingenberg, Frank van Swol, and C.F. Zukoski. The small shear rate response of electrorheological suspensions. I. Simulation in the point-dipole limit. *J. Chem. Phys.*, 94(9):6160–6169, 1991.

[70] D.J. Klingenberg, Frank van Swol, and C.F. Zukoski. The small shear rate response of electrorheological suspensions. II. Extension beyond the point-dipole limit. *J. Chem. Phys.*, 94(9):6170–6178, 1991.

[71] A.J.C. Ladd. Short time motion of colloidal particles: numerical simulation via a fluctuating lattice–boltzmann equation. *Phys. Rev. Lett.*, 70(9):1339–1342, 1993.

[72] M.C. Lagomarsino, F. Capuani, and C.P. Lowe. A simulation study of the dynamics of a driven filament in an aristotelian fluid. *J. Theor. Biol.*, 224:215–224, 2003.

[73] M.C. Lagomarsino, I. Pagonabarraga, and C. P. Lowe. Hydrodynamic induced deformation and orientation of a microscopic elastic filament. *Phys. Rev. Lett.*, 94(14):148104, 2005.

[74] L. D. Landau and E. M. Lifshitz. *Theory of Elasticity.* Pergamon Press, third edition, 1986.

[75] L.D. Landau and E.M. Lifshitz. *Fluid Mechanics.* Pergamon, 1959.

[76] E. Lauga. Floppy swimming: Viscous locomotion of actuated elastica. *Phys. Rev. E*, 75:041916, 2007.

[77] E. Lauga, W.R. DiLuzio, G.M. Whitesides, and H.A. Stone. Swimming in circles: Motion of bacteria near solid boundaries. *Biophys. J.*, 90:400–412, 2006.

[78] J. Lighthill. Flagellar hydrodynamics: The John von Neumann lecture, 1975. *SIAM Review*, 18(2):161–230, 1976.

[79] D. Liu, E.E. Keaveny, M.R. Maxey, and G.E. Karniadakis. A spectral element and force-coupling method for flow past 3d ellipsoidal particles. *to be submitted to J. Comp. Phys.*, 2008.

[80] D. Liu, M.R. Maxey, and G.E. Karniadakis. Modeling and optimization of colloidal micro-pumps. *J. Micromech. Microeng.*, 14:567–575, 2004.

[81] S. Lomholt and M.R. Maxey. Force-coupling method for particulate two-phase flow: Stokes flow. *J. Comp. Phys.*, 184:381–405, 2003.

[82] S. Lomholt, B. Stenum, and M.R. Maxey. Experimental verifications of the force coupling method for particulate flows. *Int. J. Multiphase Flow*, 28:225–246, 2002.

[83] C.P. Lowe. Dynamics of filaments: modelling the dynamics of driven microfilaments. *Phil. Trans. R. Soc. Lond. B*, 358:1543–1550, 2003.

[84] H.V. Ly, F. Reitich, M.R. Jolly, H.T. Banks, and K. Ito. Simulations of particle dynamics in magnetorheological fluids. *J. Comp. Phys.*, 155:160–177, 1999.

[85] H. Ma and M.D. Graham. Theory of shear-induced migration in dilute polymer solutions near solid boundaries. *Phys. Fluids*, 17:083103, 2005.

[86] Y. Magariyama, M. Ichiba, K. Nakata, K. Baba, T., and Y. Magariyama. A fluid-dynamic interpretation of the asymmetric motion of singly flagellated bacteria swimming close to a boundary. *Biophys. J.*, 88:3648–3658, 2005.

[87] M. Manghi, X. X. Schlagberger, and R.R Netz. Propulsion with a rotating elastic nanorod. *Phys. Rev. Lett.*, 96:068101, 2006.

[88] J.E. Martin and R.A. Anderson. Chain model of electrorheology. *J. Chem. Phys.*, 104(12):4814–4827, 1996.

[89] J.E. Martin, K.M. Hill, and C.P. Tigges. Magnetic-field-induced optical transmittance in colloidal suspensions. *Phys. Rev. E*, 59(5):56765692, 1999.

[90] F. Martínez-Pedrero, M. Tirado-Miranda, A. Schmitt, and J. Callejas-Fernández. Scaling in the aggregation dynamics of a magnetorheological fluid. *Phys. Rev. E*, 76:011405, 2007.

[91] M.R. Maxey and B.K. Patel. Localized force representation for particles sedimenting in Stokes flow. *Int. J. Multiphase Flow*, 27:1603–1626, 2001.

[92] M.R. Maxey and J.J. Riley. Equation of motion for a small rigid sphere in a nonuniform flow. *Phys. Fluids*, 26(4):883–889, 1983.

[93] S. Melle, O.G. Calderon, M.A. Rubio, and G.G. Fuller. Microstructure evolution in magnetorheological suspensions governed by mason number. *Phys. Rev. E*, 68(041503), 2003.

[94] S. Melle and J.E. Martin. Chain model of a magnetorheological suspension in a rotating field. *J. Chem. Phys.*, 118(21):9875–9881, 2003.

[95] S. Melle, M.A. Rubio, and G.G. Fuller. Time scaling regimes in aggregation of magnetic dipolar particles: Scattering dichroism results. *Phys. Rev. Lett.*, 87(11):115501, 2001.

[96] H. Moore, K. Dvorakova, and W. Breed. Exceptional sperm cooperation in the wood mouse. *Nature*, 418:174–177, 2002.

[97] V. Namias. Application of the Dirac delta function to electric current and magnetic multipole distributions. *Am. J. Phys.*, 47(9):803–806, 1979.

[98] P.Dominguez-Garcia, S. Melle, O.G. Calderon, and M.A. Rubio. Doublet dynamics of magnetizable particles under frequency modulated rotating fields. *Colloids and Surfaces A: Physiochem. Eng. Aspects*, 270-271:270–276, 2005.

[99] I. Petousis, E. Homburg, R. Derks, and A. Dietzel. Transient behaviour of magnetic micro–bead chains rotating in a fluid by external fields. *Lab on a Chip*, 7:1746–1751, 2007.

[100] I.V. Pivkin, P.D. Richardson, and G.E. Karniadakis. Blood flow velocity effects and role of activation delay time on growth and form of platelet thrombi. *PNAS*, 103(46):17164–17169, 2006.

[101] C. Pozrikidis. *Boundary integral and singularity methods for linearized viscous flow.* Cambridge University Press, 1992.

[102] J.H.E. Promislow, A.P. Gast, and M. Fermigier. Aggregation kinetics of paramagnetic colloidal particles. *J. Chem. Phys.*, 102(13):5492–5498, 1995.

[103] E.M. Purcell. Life at low Reynolds number. *Am. J. Phys.*, 45(1):3–11, 1977.

[104] M. Ramia, D.L. Tullock, and N. Phan-Thien. The role of hydrodynamic interaction in the locomotion of microorganisms. *Biophys. J.*, 65:755–778, 1993.

[105] A. Rida and M.A.M. Gijs. Manipulation of self-assembled structures of magnetic beads for microfluidic mixing and assaying. *Anal. Chem.*, 76:6239–6246, 2004.

[106] I.H. Riedel, K. Kruse, and J. Howard. A self-organized vortex array of hydrodynamically entrained sperm cells. *Science*, 309(5732):300–303, 2005.

[107] M. Roper, R. Dreyfus, J. Baudry, M. Fermigier, J. Bibette, and H.A. Stone. On the dynamics of magnetically driven elastic filaments. *J. Fluid Mech.*, 554:167–190, 2006.

[108] R.E. Rosensweig. *Ferrohydrodynamics.* Dover Publications, Inc., 1997.

[109] W.B. Russel, D.A. Saville, and W.R. Schowalter. *Colloidal Dispersions.* Cambridge University Press, 1989.

[110] D. Saintillan and M.J. Shelley. Orientational order and instabilities in suspensions of self-locomoting rods. *Phys. Rev. Lett.*, 99(5):058102, 2007.

[111] N. Sharma and N.A. Patankar. Direct numerical simulation of the brownian motion of particles by using fluctuating hydrodynamic equations. *J. Comp. Phys.*, 201:466–486, 2004.

[112] R.A. Simha and S. Ramaswamy. Hydrodynamic fluctuations and instabilities in ordered suspensions of self-propelled particles. *Phys. Rev. Lett.*, 89(5):058101, 2002.

[113] G. I. Taylor. Analysis of the swimming of microscopic organisms. *Proc. R. Soc. Lond. A*, 209:447–461, 1951.

[114] G. I. Taylor. The action of waving cylindrical tails in propelling microscopic organisms. *Proc. R. Soc. Lond. A*, 211:225–239, 1952.

[115] A.K. Vuppu, A.A. Garcia, and M.A. Hayes. Video microscopy of dynamically aggregated paramagnetic particle chains in an applied rotating magnetic field. *Langmuir*, 19:8646–8653, 2003.

[116] C. H. Wiggins and R. E. Goldstein. Flexive and propulsive dynamics of elastica at low Reynolds number. *Phys. Rev. Lett.*, 80(17):3879–3882, 1998.

[117] C.H. Wiggins, D. Riveline, A. Ott, and R. E. Goldstein. Trapping and wiggling: Elastohydrodynamcis of driven microfilaments. *Biophys. J.*, 74:1043–1060, 1998.

[118] C. W. Wolgemuth, T.R. Powers, and R. E. Goldstein. Twirling and whirling: Viscous dynamics of rotating elastic filaments. *Phys. Rev. Lett.*, 84(7):1623–1626, 2000.

[119] D.M. Woolley. Motility of spermatozoa at surfaces. *Reproduction*, 126:259–270, 2003.

[120] K-M. Yeo. Personal communication. 2008.

[121] T. S. Yu, E. Lauga, and A. E. Hosoi. Experimental investigations of elastic tail propulsion at low Reynolds number. *Phys. Fluids*, 18:091701, 2006.

[122] I.Y.Z. Zia, R.G. Cox, and S.G. Mason. Ordered aggregates of particles in shear flow. *Proc. R. Soc. Lond. A*, 300:421–441, 1967.